EVALUATION OF NOVEL HOVERING STRATEGIES TO IMPROVE GRAVITY-TRACTOR DEFLECTION MERITS

A Thesis presented to

the Faculty of the Graduate School

at the University of Missouri

In Partial Fulfillment

of the Requirements for the Degree

Doctor of Philosophy

---

by

Darío O. Cersosimo

Dr. Craig A. Kluever, Thesis Supervisor

MAY 2011

The undersigned, appointed by the Dean of the Graduate School, have examined the dissertation entitled:

EVALUATION OF NOVEL HOVERING STRATEGIES
TO IMPROVE THE GRAVITY-TRACTOR DEFLECTION MERITS

presented by Darío O. Cersosimo,
a candidate for the degree of Doctor of Philosophy and hereby certify that, in their opinion, it is worthy of acceptance.

Dr. Craig A. Kluever

Dr. Douglas Smith

Dr. Frank Feng

Dr. Roger Fales

Dr. Jan Segert

To my parents, Leonor and Juan Carlos.

ACKNOWLEDGMENTS

First and foremost I would like to thank to my advisor, Dr. Craig A. Kluever for the assistance he provided to during the research process. I also would like to thank Professor Douglas Smith, director of the GAANN fellowship, which provided the financial support needed to make this work possible. I wish to express my gratitude to Dr. Daniel J. Scheeres for sharing his views and opinions in the early stages of this dissertation work. Finally I would like to thank my friends Weijun Huang, and Melanie Carraher.

Contents

List of Tables

List of Figures

Nomenclature

a	Asteroid major semiaxes, [m].
a_x	Component of the GT acceleration along x [m/s^2].
a_y	Component of the GT acceleration along y [m/s^2].
a_z	Component of the GT acceleration along z [m/s^2].
a_{net}	Acceleration supplied by each thruster, [m/s^2].
A_{sa}	Area of the solar array, [m^2].
b	Asteroid intermediate semiaxis, [m].
c	Asteroid minor semiaxis, [m].
d	Distance from the GT to the center of mass of the asteroid, [m].
e_{ab}	Axial eccentricity between semiaxes a and b.
f_{merit}	Figure of merit.
$f_{penalty}$	Figure of penalty.
$\mathbf{F}_{sp}$	Force due to solar radiation pressure, [N].
$\mathcal{F}$	Solar flux [kW/m^2].

$\mathcal{F}_0$ Solar flux at 1 AU [kW/m^2].

g_0 Acceleration of gravity at sea level [m/s^2].

G Gravitational constant [m^3/kg/s^2].

h Altitude from the surface of the asteroid [m].

I_{sp} Specific impulse [s].

k_d Derivative gain, [1/s].

k_l Modulus of the elliptic integral.

k_p Proportional gain, [1/s^2].

m Mass of the spacecraft, [kg].

m_0 Initial mass of the spacecraft, [kg].

m_p Propellant mass, [kg].

$\dot{m}_p$ Propellant mass flow rate, [kg/s].

M Mass of the asteroid, [kg].

$\mathcal{P}$ Pressure due to solar photons [N/m^2].

P Rotational period of the asteroid, [s].

P_{in} Power supplied to the thruster, [W].

P_{load} Net power load of the spacecraft subsystems, [W].

$\mathbf{r}$ Position vector, [m/s].

$\mathbf{r}_{ref}$ Reference position vector, [m/s].

$\dot{\mathbf{r}}$ Velocity vector, [m/s].

$\dot{\mathbf{r}}_{ref}$	Reference velocity vector, [m/s].
$\mathcal{R}$	Heliocentric distance, [AU].
t	Time, [s].
T	Engine thrust, [N].
T_c	Control Thrust, [N].
T_x	Component of thrust in the x direction, [N]
T_{max}	Maximum thrust available, [N].
T_{min}	Minimum thrust available, [N].
T_{net}	Sum of the thrust supplied by each engine, [N].
$\mathbf{u}$	Control input vector, [m/s^2].
V	Gravitational Potential, [kg.m/s].
x	Component of position along the $\hat{\mathbf{i}}$-axis.
y	Component of position along the $\hat{\mathbf{j}}$-axis.
z	Component of position along the $\hat{\mathbf{k}}$-axis.
β	Engine canting angle, [deg].
δr	Position tolerance of the Dead-band controller, [m].
Δm_{GT}	Propellant used by the GT, [kg].
Δm_{xGT}	Propellant used by the xGT, [kg].
Δv	Velocity change imparted on the asteroid, [m/s].
Δv_{GT}	Velocity change imparted on the asteroid by the classical GT, [m/s].

Δv_{xGT} Velocity change imparted on the asteroid by the xGT, [m/s].

ε Ratio between the minor and intermediate semiaxes of the asteroid.

η Component of position along the $\hat{\eta}$-axis, [m].

η_T Thruster efficiency.

λ Latitude, measured from the equator towards the rotation pole.

μ Gravitational parameter, [m^3/s^2].

ξ Component of position along the $\hat{\xi}$-axis, [m].

ρ Asteroid density, [kg/m^3].

ρ_a Coefficient of absorbed radiation.

ρ_d Coefficient of diffuse reflection.

ρ_s Coefficient of specular reflection.

ϕ_l Amplitude of the elliptic integral.

ϕ_{phw} Plume half-width, [deg].

ω Rotation rate of the asteroid, [rad/s].

ω_{GT} Angular rate of the periodic translational motion of the GT, [rad/s].

ζ Component of position along the $\hat{\zeta}$-axis, [m].

ABSTRACT

The gravity-tractor (GT) consists of a spacecraft hovering inertially over a small asteroid. This equilibrium state is achieved by the action of a pair of engines that balance the gravitational acceleration. Due to Newton's law of gravitation the spacecraft causes a small gravitational pull on the asteroid that after prolonged time intervals causes a small change in its trajectory preventing it from impacting the Earth. This dissertation introduces a novel concept in the implementation of the GT to augment its deflection merits. Two novel guidance laws are designed to take advantage of the asteroid shape and rotation rate forcing the GT spacecraft to move towards and away the center of mass of the asteroid in synchronous motion with its rotation, resulting in an increased gravitational pull. The asteroid model was generalized as a solid, homogeneous triaxial ellipsoid. A small GT spacecraft was proposed and a detailed model of the NSTAR ion thrusters was used to investigate the efficiency of the GT operating under these novel guidance laws and the classical inertial hovering. The performance of these hovering laws was examined over a wide range of asteroid shapes and rotation rates. The results obtained suggest that it is possible to improve the deflection merits by up to 60%. The propellant efficiency showed to be sensitive to the spacecraft parameters; in particular, the engine model and the controller used to sustain the desired hovering state play an important role in the propellant penalties associated with these extended hovering modes. Furthermore, these results indicate that previous works have overestimated the propellant efficiency of a typical GT by using oversimplified models of solar electric engines.

Chapter 1

Introduction

1.1 Earth Impact Evidence

The solar system is plagued with evidence of interplanetary collisions and the Earth is not exempt. The cratered surface of Mercury, Venus, Mars and The Moon are a direct proof of the dynamical interactions between minor solar system bodies and terrestrial planets. The Earth is not exempt from these interactions, but its impact record is less obvious due to erosion and geological activity [1]. In fact, the Earth impact database list 178 confirmed impact structures on Earth.[1] The Tunguska event is a recent proof of these interplanetary catastrophes. In 1908 an object of approximately 60 m diameter exploded in the atmosphere at a height of 8 km in the middle of an unpopulated area in Siberia. The energy released was estimated between 10 to 15 mega-tons of TNT devastating an area of about 2000 km^2 of forest [2, 3]. The Tunguska meteoroid disintegrated in the air before reaching the surface, but in many occasions these meteoroids are able to survive the pressures of atmospheric entry and reach the ground. The Barringer crater in Arizona presents direct evidence of

[1]The Earth Impact Database, http://www.passc.net/EarthImpactDatabase/index.html.

the survival of atmospheric entry. In the early ages of the solar system, during the heavy bombardment (4.1-3.8 billion years ago), these collisions played an important role in the delivery and distribution of exogenous matter, such as volatiles, organic compounds and possible water to Earth [4]. At a lower rate, these minor celestial bodies continued bombarding the Earth until present days. This sequence of impacts has played an essential role in the formation of the Earth, but also shaped and shifted the evolution path of Earth's biosphere.

In 1980 Alvarez *et al.* [5], presented strong evidence supporting the hypothesis that the mass extinction of the Cretaceous-Tertiary (65 million years ago), was due to the impact of an asteroid of about 10 to 15 km diameter. The impact crater has a diameter of 180 km in diameter and is located in the Yucatan peninsula. Their findings triggered concerns about the hazards posed to our civilization by the population of small bodies orbiting in the vicinity of the Earth. These objects are known as near-Earth objects (NEO) include asteroids and certain comets.

1.2 The Near-Earth Object Environment

Near-Earth objects are those asteroids with perihelion distances $q \leq 1.3$ AU and aphelion distances $Q \geq 0.983$AU [6]; and short-period comets with $q < 1.3$ AU and orbital period, $P < 200$ years. The near-Earth asteroid (NEA) population is divided into three subgroups based on their orbital semimajor axis a, perihelion q and aphelion Q distances. These population subsets of NEAs are denominated Apollos, Atens and Amors (see Fig. 1.1 for schematic of their orbits). Apollos and Atens have Earth-crossing orbits with semimajor axes $a \geq 1.0$AU. The Apollos have perihelion $q \leq 1.0167$ AU and the Atens have aphelion $Q \geq 0.983$ AU. The Amors class consist of those NEA with perihelion $1.0167 < q \leq 1.3$ AU. Orbital perturbations may cause the Amors to become Earth-crossing NEOs. Another family of asteroids that does

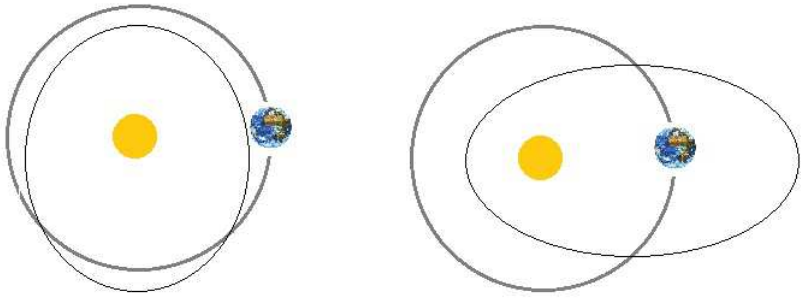

(a) Apollo (b) Aten

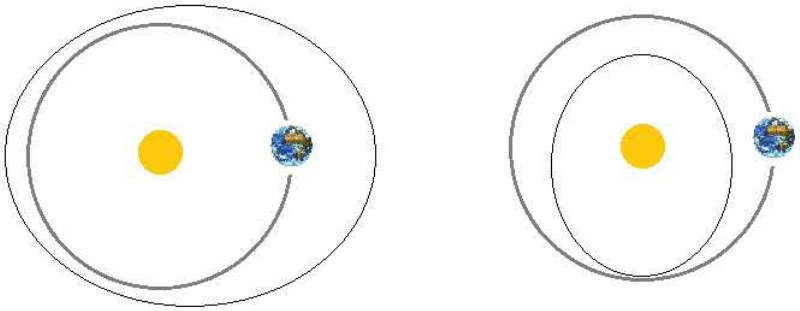

(c) Amor (d) IEO

Figure 1.1: Orbit diagrams of the four families of near-Earth asteroids.

not fall in the official NEA classification are those objects whose orbits are bounded inside the Earth's orbit ($Q < 0.983$ AU). These objects are called inner-Earth Objects (IEO) [7] or Atiras named after asteroid 163693 Atira.[2]

The current cataloged NEO population consists of more than 7000 objects where less that 100 are near-Earth comets (NEC). Within the NEA population approximately 12% are larger than 1 km in diameter. Those NEA that have a minimum orbit intersection distance (MOID)[3] with Earth of 0.05 AU or less and a diameter of 110 m or larger are considered potentially hazardous asteroids (PHA) [8, 9, 10]. The catalogued population of PHA contains 1125 asteroids where 147 (13%) are of the order of a kilometer size.

The asteroids in the NEO population are supplied from the main asteroid belt,

[2]The Near-Earth Object database does not include aphelion limits for the classification of NEOs and considers Atiras as part of the NEO, (http://neo.jpl.nasa.gov/neo/groups.html).

[3]MOID is the closest possible approach distance between the osculating orbits of two objects.

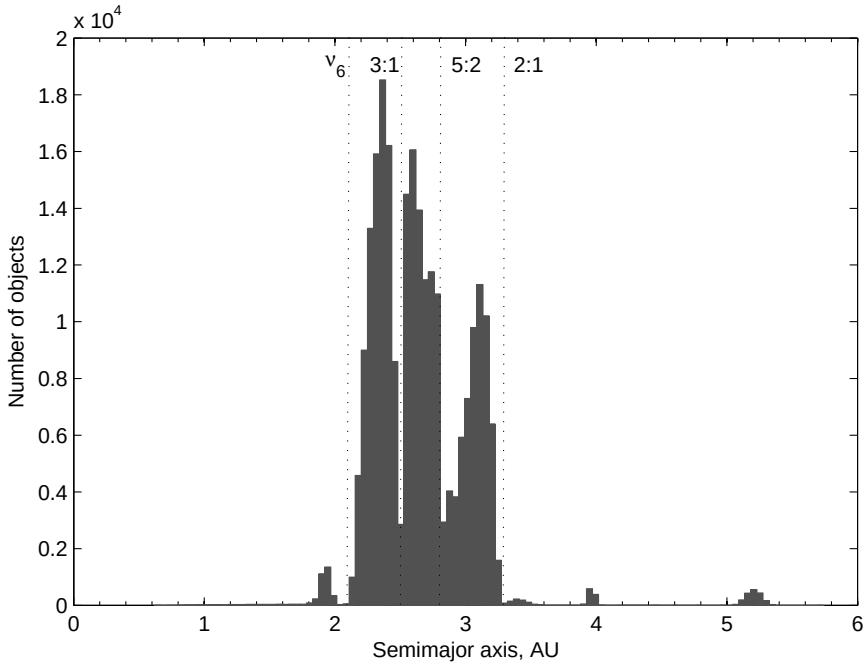

Figure 1.2: Distribution of the population in main asteroid belt.

located between 2.1 to 3.3 AU, due to the action of resonant phenomena. Some of the resonance regions can be identified by unpopulated regions in the main belt called *Kirkwood gaps* (see Fig. 1.2). These gaps are a consequence of mean motion orbital resonances with Jupiter that, due to gravitational perturbations, boost the asteroids eccentricities causing them to reach the orbits of the inner planets. The most prominent mean motion resonances are the ν_6, 3:1, 5:2 and 2:1.

The ν_6 resonance marks the inner boundary of the main belt. It is caused when the precession frequency of the asteroid longitude of perihelion is equal to the sixth secular frequency of the planetary system. The median lifetime of bodies in this region is about 2 million years [11, 12, 7]. Once expelled from the ν_6 region most of these bodies can spend an average of 6.5 million years in the NEO region until they end up colliding with the Sun. The 3:1 mean motion resonance is located at 2.5 AU with typical mean lifetimes close to 2 million years. Bodies driven from this region into NEO space have a mean lifetime of 2.2 million years. They often collide with the Sun

but sometimes are ejected from the solar system [7]. The second deep gap corresponds to the 5:2 at about 2.8 AU. The orbital lifetimes in this region have timescales in the order of 0.6 million years. The 2:1 mean motion resonance exist at 3.3 AU. This resonance has the largest population time scale >100 million years. Once removed from this region about 20% could become Earth-crossers [11]. Objects falling into the 5:2 and 2:1 resonance regions are likely to be injected into Jupiter crossing or hyperbolic orbits being not major contributors to the NEO population [7]. Diffusive resonances are weaker than mean motion resonances but are spread across the main belt driving most asteroid orbits to be slightly chaotic. The mean lifetime in these resonance changes broadly, between 10 to 10^3 million years depending on the kind of resonance and the initial eccentricity [7, 12].

Comets contributing to the NEO population are believed to come from two main sources, the trans-Neptunian region and the Oort cloud. The trans-Neptunian region has segments where orbits are dynamically unstable over the lifetime of the solar system. Within the population of Earth-crossing comets two families are distinguished, those belonging to the Jupiter family and those of the Halley family. Jupiter family comets reach the inner solar system due to close encounters with Jupiter. Their inclination does not exceed 27 deg [13] and their periods are no longer than 20 years. Halley family comets have periods between 20 and 200 years. These are believed have originated from the Oort cloud. Their near-isotropic nature gives them a broad inclination distribution, in some cases exceeding 90 deg.

In June 2004 R. Tucker and his coworkers discovered a NEO wandering in a trajectory that six months later was determined to have 2.7% chance of coliding with Earth in April 13, 2029 [14]. Upon astrometric corrections this probability decreased to almost zero. Today this asteroid is known as 99942 Apophis and is under intense watch since its 2029 flyby Earth could lead to a resonant return and subsequent impact in 2039. The size of Apophis is estimated to be 270 ± 60 m in diameter. The

mass of Apophis is estimated to be 2.7×10^{10} kg assuming a uniform spherical body with 2600 kg/m^3 of density. The rotation period of Apophis is 30.4 hrs [15].

1.3 Deflection and Mitigation Strategies

When envisioning alternatives to deflect a potentially hazardous object (PHO)[4] from collision with Earth, imagination is the limit. While time, feasibility and reliability are the constraints. Several system architectures have been proposed to mitigate the treat an asteroid or comet could pose to the Earth in the case of a foreseen collision. These mitigation strategies vary widely from simple but powerful detonations to very complex and often high-precision systems that use all the physical principles on hand to convert any source of external energy available into added kinetic energy to the threatening object.

Given the need to deflect a PHO in collision course with Earth, the choice of a deflection strategy is intimately related to a wide range of key factors determining the success of the deflection. The most important factor is the *warning time*, that is the time between the confirmation of the threat and the predicted collision epoch. Warning times could range from decades to weeks or days. Long warning times allow the community to evaluate and develop an optimal mitigation strategy for the particular scenario. However, extremely short warning times would only allow to the evacuation of the population in the predicted area of impact.

The deflection of an asteroid requires the physical interaction between the body and the mitigation system [16]. In fact, several deflection strategies interact directly or indirectly with different physical properties of the target. Therefore, a comprehensive knowledge about the physical properties of the body (i.e., composition, external structure, internal structure, dynamical configuration, number of orbital companions,

[4] An asteroid or a comet is considered a PHO when its MOID is 0.05 AU or less and has a diameter of 150 meters or more.

etc), would lead to a more efficient mitigation strategy. A summary of these architectures is presented in the following paragraphs. Although the list is not comprehensive, it is intended to underline the current line of thinking about the issue.

1.3.1 Impulsive Strategies

The nuclear alternative

Perhaps the most intuitive method to deflect an asteroid could be by means of a nuclear device detonating in the vicinity of the asteroid surface. Nuclear explosives are a viable alternative because they deliver the highest energy to mass ratio, in the order of 4×10^6 MJ/kg. In contrast a non-nuclear explosive can supply an energy ratio of 6 MJ/kg [17].

There are various alternatives for the implementation of the nuclear option. A nuclear device can be detonated at an optimal altitude from the asteroid surface. The neutrons and X-ray yield irradiating the surface will cause the blow-off of surface and near-subsurface material. Material ejected in excess of the NEO escape velocity can generates the needed impulse for the deflection. A nuclear detonation on the surface the NEO can produce bigger crater consequently increasing the amount of ejected material contributing to a higher impulse [18, 19, 20]. A third nuclear alternative is to detonate the device beneath the surface of the asteroid. The later will require mining hardware which could decrease the energy to mass ratio of the entire system. Surface and subsurface detonations are likely to yield higher momentum change but at an increased the risk of fragmenting the asteroid into large pieces that could threat the Earth with multiple impacts. Asteroid fragmentation could easily occur in bodies having weak cohesive strength held together by gravitational forces such as rubble piles, contact binaries, or cometary nucleus.

Kinetic energy impacts

A kinetic energy impact is the simplest way to change the orbital momentum of a PHO. A massive projectile can be aimed to hit the NEO parallel or anti-parallel to its orbital motion increasing or reducing its orbital energy, respectively during its perihelion passage [21, 22]. The change in the orbital momentum is the sum of the projectile momentum plus the momentum of the ejected particles with speeds greater that the escape speed of the asteroid. The momentum added by the ejected mass depends on the material and structural composition of the asteroid. Research has shown the ejecta particles can contribute up to 10 times to the momentum transferred by the impactor [23, 19, 20]. Thus, if the asteroid is highly porous, little or none ejecta will occur [20]. In such case the momentum transfer is due only to the impacting projectile.

The fundamental technical challenges of this strategy were tested successfully during the Deep-Impact mission [24] to comet 9P/Tempel 1 where a 364-kg projectile impacted its surface at a relative velocity 10.2 km/s. The predicted change in the comet's heliocentric velocity (Δv), due to the collision was 0.00005 mm/s [25]. Other technical issues arise in the guidance of a deflector impactor towards an asteroid or a comet. In such case, the direction of the impact needs to be precisely aligned with the desired Δv vector and aimed in the direction of the center of mass in order to minimize torque losses, rising challenges in the design of terminal guidance stage.

1.3.2 Slow Push Strategies

A second family of mitigation alternatives, often referred as "slow push strategy", relies on changing the orbit of the target PHO by applying very small forces over long periods of time. Some of these strategies require a spacecraft to rendezvous and land on the PHO or to perform a sequence of maneuvers about the target. The slow

push alternatives can be divided into two groups: contact and non-contact methods. Contact methods are those that require the deflection system to land and or attach to the surface of the PHO. Non-contact methods are those systems able to operate at a distance from the surface of the PHO. Surface operations will require detailed knowledge of the surface and subsurface properties to permit a better design of the anchoring or mining systems.

Mass drivers

From a planetary defense perspective the mass driver system consist on a device anchored on the surface of the PHO that digs out material from its surface, accelerates it and then ejects it at high speeds producing a momentum exchange between the asteroid and the ejected mass, similar to a rocket engine. The thrust achieved is the product between the mass flow rate and the velocity of the ejected material. Higher ejection velocities will decrease the amount of mass needed to be excavated in order to achieve the Δv goal [23]. Melosh *et al.,* [23] assume the use of solar energy to supply power to the system in accordance to a non-nuclear alternative.

Olds *et al.* [26] analyzed a mission concept of multiple mass drivers systems, each powered by a small nuclear reactor. The advantage of having multiple mass drivers is that it provides system redundancy against individual system failures and the ability to operate over extended times. The nuclear reactor allows continuous operation during eclipse conditions.

Despite the relative technological advanced state of this system [17, 26], the mass-driver concept suffers of several practical problems. The surface characteristics of these bodies are poorly known driving to serious complications in the design of an anchoring system and a mining strategy to maintain a continuous mass supply to the ejector. The thermal gradient during the day and eclipse phases may adversely affect the use of mining tools [17]. Other difficulties arise with this strategy, the non-

spherical nature of these bodies, the roughness of the surface topology and rotation state present a challenge when pointing the thrust vector in the correct direction. For example, if the thrust vector does not point in the direction of the body center of mass a torque component due to the ejected mass will cause the asteroid to change its angular momentum rather than its orbital momentum.

Asteroid tug

The asteroid tug could be realized by landing and subsequently anchoring a spacecraft to the surface of the NEO. Sufficiently powerful engines to re-orient or de-spin the asteroid and then tug it in the desired direction [27, 28]. Alternatively, the engines could be fired periodically every time the thrust vector is aligned with the desired direction of push at the expense increased time to complete the deflection. The rocket engine could consist of high efficiency propulsion system using solar electric or nuclear electric propulsion. This method reduces the problem of mining into the surface of uncertain properties. However, anchoring the system to the surface and re-orienting the spin are challenging operations.

Solar concentrators

Solar concentrators were introduced by Melosh, *et al.* [29]. The idea behind the solar concentrator is to evaporate the surface of the PHO by using a reflective mirror that collects the solar photons concentrating them on a small spot on the surface of the asteroid. The thrust results from the vaporized jet of surface material. A second alternative could be the use of laser beams [30]. The laser system can be ground-based or space-based. These methods are not sensitive to target rotation and they might be very attractive in cases where the target rich in volatile materials such as comets.

Albedo change

Albedo is a measure of the reflectivity of a Lambertian surface. This strategy is intended to change the reflective properties of the asteroid surface altering the amount of radiation absorbed or reflected once the asteroid's surface is exposed to the Sun. As the asteroid rotates the side previously exposed to the Sun enters to the dusk zone and the warm surface radiates more energy than the cooler dawn side. The difference in energy radiated generates a force due to the momentum of the photons which produces a very small acceleration on the asteroid. A mitigation method has been proposed by attempting to change the reflection properties of the surface by painting the asteroid with a dark or light coating depending in the direction in which the force needs to be applied [31].

Gravity tractor

The gravity-tractor (GT) concept was first proposed by Lu and Love [32]. In their article, the authors claim that a spacecraft can use its own mass to change the orbit of a small body in a collision route with Earth. To achieve such a deflection, the spacecraft is kept at a constant distance from the center of mass of the PHO by the action of the engine thrusters. Due to Newton's law of gravitation, the asteroid will accelerate at a rate proportional to the spacecraft mass and the inverse of the squared distance. The simplest GT scheme consist on a spacecraft with two main engines continuously thrusting to balance the gravitational pull. These engines are tilted away to prevent their exhaust plumes to hit the surface of the asteroid counteracting the gravitational pull of the spacecraft (see Fig. 1.3).

The GT alternative allows precise orbit tracking of the threatening NEO due to the on board transponder that periodically transmit its position to Earth, augmenting the accuracy of the deflection maneuver [33]. The GT is not sensitive to uncertainties regarding its surface characteristics and allows to perform scientific observations and

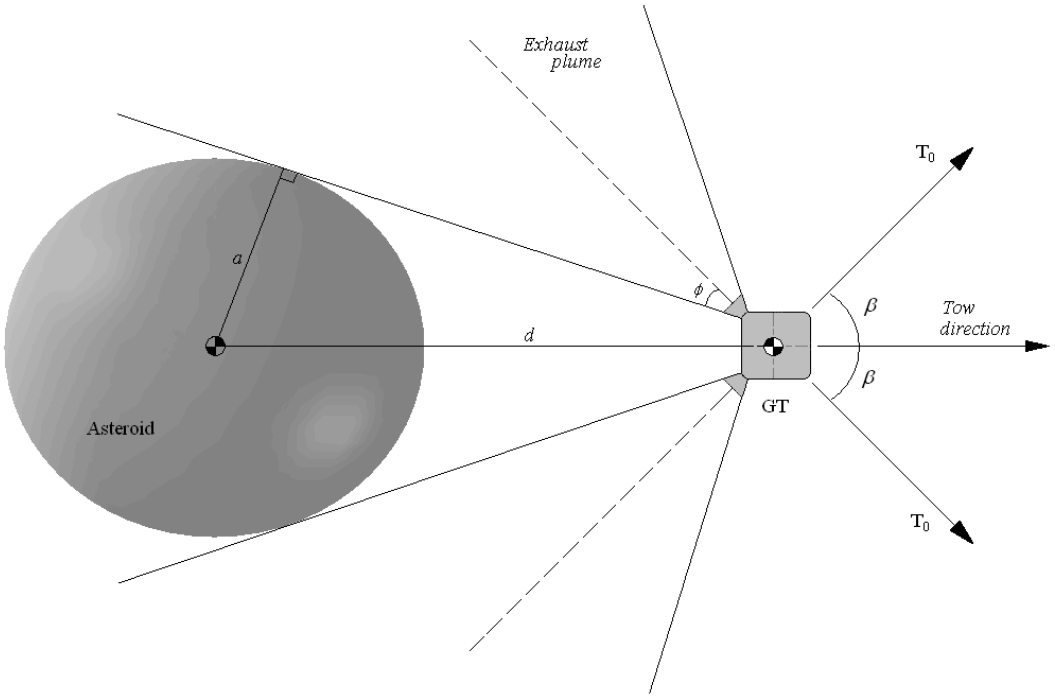

Figure 1.3: Geometrical representation of the classical gravity tractor system as proposed by Lu and Love [32].

object characterization. Another advantage, shared as well among other slow-push deflection methods is that the slow-acting force due to the GT pull is unlikely to cause fragmentation of weakly binded body.

1.4 Contributions of this Dissertation

The gravity tractor concept has evolved since its introduction by Lu and Love. Several studies have been carried out proposing alternative dynamical configurations to improve the gravity tractor efficiency. McInnes [34], studied the alternative of placing a GT spacecraft in a displaced non-Keplerian orbit with the intention to alleviate the problem of the canted engines that is a key issue for a gravity tractor operating in inertial hovering. This configuration could reduce the thrust demanded by the engines.

Wie [35], elaborates further on the work by McInnes by proposing a constellation with multiple gravity tractors hovering in a pair of displaced non-Keplerian or halo orbits. In the same article, Wie introduces a solar sail alternative for a gravity tractor. The solar sail gravity tractor does not requires propellant because it is propelled by the momentum exchange from solar photons reflected off from the sail. Fahnestock *et al.* [36], investigated the coupled dynamics between the NEO and the GT spacecraft using polyhedral models of a NEO to analyze the performance for two different GT configurations: a pendulum-shaped and a novel bar-shaped spacecraft, both powered by nuclear electric engines. In their work they point out the effects of the coupled dynamics in the operational performance of the GT. However, none of these have proposed an alternative to increase the amount of acceleration imparted on the asteroid which is the prime characteristic of any asteroid deflection system.

The gravity tractor is the subject of this dissertation and our goal is to improve the acceleration that a single gravity tractor can impart on an asteroid. This goal is achieved by considering the generic ellipsoidal shape and spin state of a threatening asteroid, and commanding the gravity tractor spacecraft to periodically adjust its distance from the center of mass of the asteroid in synchronous motion with its rotation period. The hypothesis of this work states that the periodic displacement of the GT spacecraft reduces its mean distance from the asteroid consequently increasing the mean gravitational acceleration over it. The secondary objective is to perform an analysis on the implementation of a realistic ion engine model to support the hovering operations in the vicinity of the asteroid. A third objective is to investigate how the performance of the GT is affected by the implementation of proportional-derivative and dead-band controllers to control the hovering motion of the spacecraft.

Chapter 2 introduces the dynamics involving the classical gravity tractor and two novel guidance laws that allow the gravity tractor spacecraft to maneuver over the asteroid. These guidance are inspired by the fact that most asteroids have prolate

shapes and can be better represented by triaxial ellipsoids rather than simple spheres as usually done in the earlier works by Lu and Lo [32], McInnes [34], and Wie [35]. Contrary to the classical inertial hover [32], we propose that the gravitational acceleration on the asteroid can be increased by maneuvering the GT in the vicinity of the asteroid. These hovering modes guide the spacecraft to move in synchrony with the asteroid spin consequently decreasing the mean distance from the centers of mass of the asteroid and the spacecraft. The amplitude of the translational motion is defined by the difference between the two largest semiaxes of the asteroid. The first guidance law to be proposed in this work restricts the spacecraft motion to a single dimension corresponding to the direction in which the acceleration is applied. The second guidance law allows the spacecraft to move in two dimensions.

The physical model of the system is introduced in Chapter 3. This chapter describes the physical models of the asteroid and the GT spacecraft with special emphasis on the the configuration and operation of the propulsion system. The spacecraft is based on the gravity tractor model introduced in Ref. [33] and sized upon the characteristics of the Dawn mission. The propulsion system is based on the NSTAR engine as flown in two interplanetary missions: Deep Space 1 and Dawn [37, 38]. Earlier works on the GT failed to consider a realistic model for the thrusters supporting hovering. In fact, the GT problem addressed by Yeomans *et al.* [39, 33] did not consider the performance variation of the thruster due to different throttle settings nor the thrust thresholds that limit the minimum thrust these ion engines can provide. We believe that including a detailed model of the thrusters has serious implications in the propellant required to sustain a GT mission to deflect an asteroid.

Chapter 4 presents the results on the performance of these hovering laws and the propellant penalties incurred due to their implementation. The first part of the chapter evaluates the performance of these novel guidance laws assuming a GT with ideal ion engines. The results are compared against the classical GT which is used

as a base model to determine the relative merits and penalties due to the guidance laws introduced in this work. The second part of Chapter 4 incorporates the detailed engine system described in Chapter 3 and emphasizes on the implications it has on the propellant efficiency of the GT. The study is performed over a wide range of asteroid shapes ranging from quasi-spherical bodies to extremely eccentric ones with rotation periods ranging from 2 hours to 1 day.

Chapter 5 describes the implementation of proportional-derivative and dead-band controllers to control the translational dynamics of the spacecraft operating under the guidance laws proposed in Chapter 2. The performance of dead-band controller to maintain inertial hovering has been studied in the literature [40, 41, 42, 39] and it was successfully implemented in the Hyabusa mission commanded by the Japanese Aerospace Exploration Agency (JAXA) [43]. A proportional-derivative controller has been suggested by Wie [35] but only in the context of the classical gravity tractor. Therefore we are motivated to investigate the performance of these controllers to sustain the guidance laws proposed in Chapter 2 and their implications on the propellant demands.

Chapter 2

The Gravity Tractor

2.1 Introduction

In this chapter we present the fundamental dynamics of the gravity tractor. The chapter begins by explaining the concept of inertial hovering and its implementation in the classical gravity tractor. In the second part of this chapter we present two novel hovering laws designed to improve the performance of a gravity tractor mission.

2.2 Hovering Strategies

2.2.1 Inertial Hovering

The concept of a spacecraft hovering inertially over a small celestial body say, an asteroid or comet was first considered by Scheeres [44]. Inertial hovering is the foundation for the classical gravity tractor. In general, inertial hovering consists of creating an artificial equilibrium point by applying a thrust $\mathbf{T_c}$ through the spacecraft engines to balance the gravitational pull of the asteroid maintaining a fixed position $\mathbf{r}$, relative

to an inertial coordinate frame usually placed at the center of mass of the asteroid. Under the assumption of a gravitational potential V and a spacecraft of mass m, the generalized vector equation of motion can be written as,

$$\ddot{\mathbf{r}} + \frac{\partial V}{\partial \mathbf{r}} = \frac{\mathbf{T}_c}{m}. \tag{2.1}$$

From a mechanical perspective, inertial hovering is the basis of the gravity-tractor concept. The towing performance of the GT is driven by its hovering locus. According to Newton's law of gravitation, the gravitational pull between the GT and the asteroid decreases with the inverse square of their relative distance. In addition, the thrusters balancing the asteroid gravitational pull need to be slanted to prevent the exhaust plumes to impinge on the asteroid surface. Such engine configuration incite losses due to the non-zero sine component of the thrust vector degrading the efficiency of the GT. The schematic of the gravity tractor system in Fig. 1.3 depicts the GT spacecraft hovering at a distance d from the center of mass of a spherical asteroid. This is the GT concept initially conceived by Lu and Love [32]. Each canted thruster supplies a net thrust T_0 directed away from the asteroid by an angle β from the spacecraft centerline. Under this configuration, the thrust needed to support inertial hovering is

$$2T_0 \cos\beta = \frac{\mu m}{d^2}, \tag{2.2}$$

where μ is the asteroid gravitational constant and m is the GT mass. The canting angle β results from adding the plume-half-width ϕ_{phw}, and the angle between the hovering distance d, and the inner edge of the plume flux tangent to the asteroid surface. For a spherical body of radius a, the canting angle is

$$\beta = \arcsin\frac{a}{d} + \phi_{phw}. \tag{2.3}$$

The results from Equations (2.2) and (2.3) motivates the search for an optimal hovering location where the gravity pull can be achieved with the least degradation of the cosine component of the hovering thrust vector. For the GT system presented in Fig. 1.3, Lu and Love [32] found this distance to be about 1.5 asteroid radii, assuming a plume-half-width $\phi_{phw} = 20$ deg. Their results are reproduced in Fig. 2.1 from a generalized perspective by mapping Eq. (2.2) as function of the hovering distance. As an illustrative example, let $T_x = \mu m/d^2$ be the thrust per unit mass imparted by the GT engines along the radial direction from the asteroid, then the optimal hovering distance corresponds to the point where Eq. (2.2) is satisfied. Figure 2.1 displays the variation of the gravitational acceleration versus distance of a hypothetical spherical NEO of unity radius and canonical gravitational constant $\mu = 1$ (dashed line). The solid line shows the cosine component of the thrust vector supplied by the two canted engines and the dotted line is the total thrust supplied by the two canted thrusters. The results in Fig. 2.1 imply that the optimum compromise between gravitational pull and cosine losses exist at their intersection. In other words, the distance where the towing effort is maximized and cosine losses are minimized. The engine canting angle at the optimal distance $d \approx 1.5$ asteroid radii results in $\beta = 60$ deg (consistent with Refs. [32, 35]).

Analytical and numerical studies on the stability of inertial and body-fixed hovering over small rotating celestial bodies were carried out by Scheeres [44], Sawai *et al.,* [40] and Broschart and Scheeres [41, 42]. These authors found, in general, that close proximity inertial hovering is stable in the lateral direction in most regions away from the resonance radius (i.e., the distance where the orbital period of the spacecraft is equal to the rotation period of the asteroid) [41]. Inertial hovering was found to be a feasible strategy that can be implemented using a simple dead-band controller of one or two-dimensions to keep a spacecraft hovering within a prescribed region above a small celestial body [42]. Results from these investigations were successfully

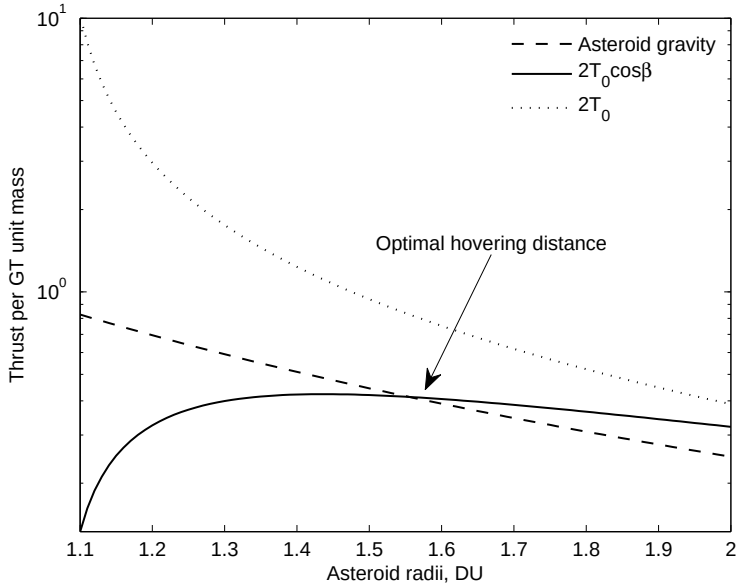

Figure 2.1: Thrust required by the GT engines to sustain inertial an inertial position over a spherical asteroid.

implemented in the Hyabusa mission commanded by the Japanese Aerospace Exploration Agency (JAXA) [43]. Recent studies carried out jointly by the Jet Propulsion Laboratory and the B612 Foundation[1] suggest that inertial hovering under a dead-band controller can be efficiently employed in a GT spacecraft during its towing phase [33, 39]. In this work, inertial hovering is used as the known baseline to measure and compare the performance of the alternative hovering strategies to be introduced in the following sections.

2.2.2 Alternative Hovering Strategies

Let's consider the fact that most small bodies in the solar system differ from a spherical shape and can be better approximated by an ellipsoidal figure with three distinct axes. We can observe as well, that these bodies have a natural tendency to reach steady-state rotation about their principal axis of inertia. On the other hand, we

[1]The B612 has been established on October 7, 2002. Their current objective is to significantly alter the orbit of an asteroid in a controlled manner by 2015. http://www.b612foundation.org

know that the gravitational pull of the GT on the asteroid is enhanced at close proximities. Our goal is to find a way to place the spacecraft in a position where it can maximize its gravitational pull over the asteroid but at the same time able to maintain a safe distance from its surface. From the previous assumptions about the asteroid, we could guide the GT spacecraft to adjust its distance from the asteroid in synchrony with its rotation. This dynamical configuration allows the GT to increase its gravitational effect over the asteroid, augmenting its towing performance. Assuming that the gravitational acceleration caused by the asteroid on the GT is balanced by the action of the engines, a supplementary thrust can be included to induce this periodic trajectory. Such periodic motion of the GT can be described by a simple harmonic oscillator in a generic coordinate q and angular rate ω_0 i.e.,

$$\ddot{q} + \omega_0^2 q = 0. \tag{2.4}$$

The solution to Eq. (2.4) is:

$$q\left(t\right) = C_0 \cos\left(\omega_0 t + \psi\right), \tag{2.5}$$

where C_0 and ψ are respectively, the displacement amplitude and phase angle determined upon the initial conditions in Eq. (2.4).

Equation (2.4) represents the general guidance law for the GT to implement what we refer to dynamic hovering. Dynamic hovering requires the engines to periodically accelerate the GT to move it towards and away the asteroid center of mass. The motion can be constrained along a single axis or in three-dimensional space. In the following section we develop two hovering strategies to extend the operational modes that could be implemented in the gravity tractor. We will refer to a GT operating under this hovering modes as the extended gravity tractor (xGT), and the two new hovering strategies as xGT1 and xGT2.

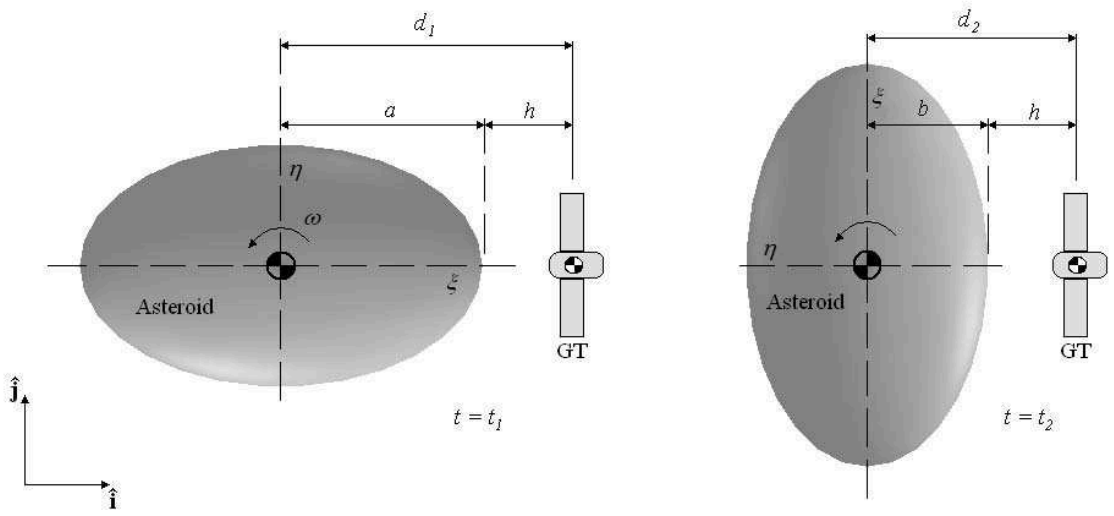

Figure 2.2: One-dimensional harmonic hovering (xGT1).

One-dimensional harmonic hovering (xGT1)

This hovering mode maintains the GT moving towards and away from the asteroid center of mass along the towing axis i.e., the direction in which the deflection Δv is to be applied (usually parallel to the asteroid velocity vector). Figure 2.2 illustrates the concept of the one-dimensional harmonic hovering. As seen from an inertial reference frame fixed at the center of mass of the NEO, the GT spacecraft moves towards and away the NEO center of mass as it spins about its minor axis at an angular rate ω_ζ. At a time $t = t_1$ the GT spacecraft is at a distance $d_1 = a + h$ from the NEO's center of mass. At a later time $t = t_2$, the NEO's attitude changed by angle $\omega_\zeta t_2 = \pi/2$ and the spacecraft had displaced to a distance $d_2 = h + b$ closer to the NEO's center of mass.

The equations of motion for a GT operating under this guidance law are obtained by combining Eqs. (2.1) and (2.4), resulting in the control thrust $\mathbf{T}_c$ to be defined as:

$$\frac{\mathbf{T}_c}{m} = -\frac{\partial V}{\partial \mathbf{r}} - \omega_{GT}^2 \frac{a-b}{2} \cos\left(\omega_{GT} t\right) \hat{\mathbf{i}}. \tag{2.6}$$

The first term on the right hand side of Eq. (2.6) balances the asteroid gravity, and

the second term induces the harmonic motion of the GT along the $\hat{\mathbf{i}}$ direction with angular rate ω_{GT}. It has been mentioned earlier that the motion of the GT needs to be synchronized with the rotation of the asteroid. The symmetry of the ellipsoidal model implies that a particular asteroid-GT configuration will repeat every half period P of the asteroid. That is, the GT returns to its initial state every π rotation of the asteroid or $\omega_{GT} = 4\pi/P$.

For the purpose of this investigation, the translation amplitude is arbitrary defined by the difference between the semiaxes a and b of the asteroid and constrained to the hovering latitude λ_0 measured counterclockwise from the asteroid's equator to its north pole. The hovering latitude is a direct consequence of the elevation of the Δv vector with respect asteroid major axis. For example, if the asteroid spin vector is parallel to the Δv vector, the resulting hovering latitude would be 90 deg, which results in a constant hovering distance d from the NEO center of mass. Conversely, if the asteroid spin vector is constrained to the plane perpendicular to Δv then the hovering latitude is at the equator. In the later case d changes periodically according with the difference between the semiaxes a and b. Another point to consider is that the towing vector Δv changes as the asteroid moves along its heliocentric path. For simplicity, the spin vector is considered to be normal to the orbital plane. Under these considerations the control thrust vector $\mathbf{T}_c$ can be written explicitly in terms of the asteroid dimensions, rotation rate and hovering latitude. Substituting the second term of the right-hand side of Eq. (2.6) with (2.5) and setting $r = q$ yields,

$$\frac{\mathbf{T}_c}{m} = -\frac{\partial V}{\partial \mathbf{r}} - 4C\omega^2 \cos\left(2\omega t + \phi_0\right) \cos\lambda_0 \hat{\mathbf{i}}, \tag{2.7}$$

where $\omega_\zeta = \frac{1}{2}\omega_{GT}$ and C is the amplitude of the harmonic trajectory relative to a central point along the displacement distance i.e., $C = \frac{1}{2}(a - b)$. Finally the resulting thrust vector $\mathbf{T}_c$ can be writen explicitly as,

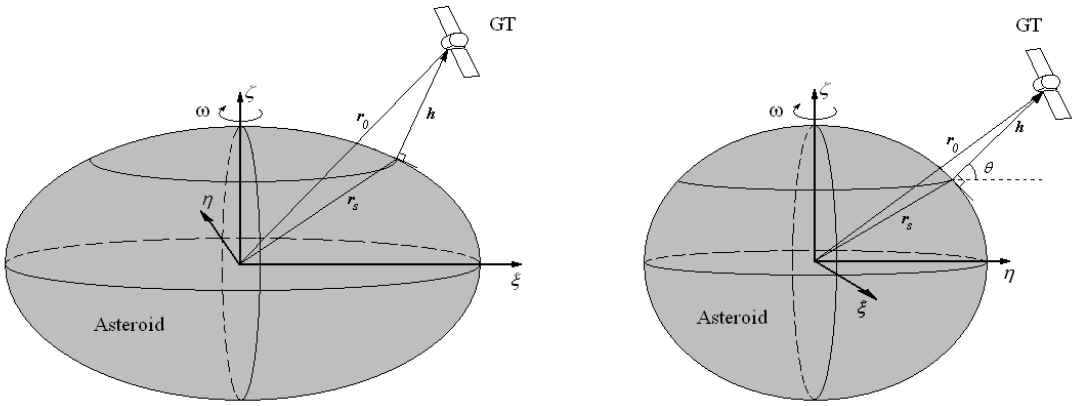

Figure 2.3: Two-dimensional harmonic hovering (xGT2).

$$\mathbf{T}_c = m\left[-4\omega^2\frac{(a-b)}{2}\cos(2\omega t)\cos\lambda_0 - \frac{\partial V}{\partial x}, -\frac{\partial V}{\partial y}, -\frac{\partial V}{\partial z}\right]^T. \tag{2.8}$$

Equation (2.8) forces the GT displacement about the $\hat{\mathbf{i}}$ coordinate while at the same time counteracts the asteroid gravitational pull along the three coordinates.

Two-dimensional harmonic hovering (xGT2)

The two-dimensional harmonic hovering frees the GT to move along the $\hat{\mathbf{i}}$ and $\hat{\mathbf{j}}$ coordinates while hovering, contrary to the one-dimensional hovering described in the previous section. The objective in this section is to derive the geometry of the reference trajectory of the GT spacecraft as seen from a reference frame fixed on the asteroid. For this, we hold on the triaxial ellipsoid model the asteroid with semiaxes $a > b > c$ spinning about its principal axis of inertia with an angular rate ω.

Consider a coordinate system with origin at the center of mass of the asteroid whose abscissas ξ, η and ζ are fixed along the primary axes of the asteroid as shown in the diagram of Fig. 2.3. At an initial time $t = t_0$ the spacecraft is placed at $\mathbf{r}_0(t_0) = [\xi_0, \eta_0, \zeta_0]^T$. Also let $\mathbf{r}_s = [\xi_s, \eta_s, \zeta_s]^T$ be a vector directed towards a point on the surface of the ellipsoid whose tangent plane is normal to the initial altitude

vector $\mathbf{h}$. From Fig. 2.3 the position of the GT spacecraft with respect to the center of coordinates is:

$$\mathbf{r}_0 = \mathbf{r}_s + \mathbf{h}. \tag{2.9}$$

The initial altitude h is defined as the shortest distance from the spacecraft to the asteroid surface. Assuming that at the initial time t_0 the GT is in the $\xi\zeta$-plane of the asteroid, then the longitude $\phi_0 = 0$ and h is determined from:

$$\min\, h = \sqrt{(\xi_0 - \xi_s)^2 + (\zeta_0 - \zeta_s)^2}, \tag{2.10}$$

where,

$$\zeta_s = c\sqrt{1 - \left(\frac{\xi_s}{a}\right)^2}. \tag{2.11}$$

The point $[\xi_s, 0, \zeta_s]$ are the coordinates of the ellipse resulting from a cross sectional cut of the ellipsoid along the $\xi\zeta$-plane, a is the major axis and c the minor axis. The direction $\hat{\mathbf{n}}$ in which the altitude is measured, is obtained from the normalized direction of the altitude vector i.e.,

$$\hat{\mathbf{n}} = \frac{\nabla E\left(\xi_s, \eta_s, \zeta_s\right)}{\|\nabla E\left(\xi_s, \eta_s, \zeta_s\right)\|}, \tag{2.12}$$

where,

$$E\left(\xi_s, \eta_s, \zeta_s\right) = \frac{\xi_s^2}{a^2} + \frac{\eta_s^2}{b^2} + \frac{\zeta_s^2}{c^2} - 1, \tag{2.13}$$

is the equation of the ellipsoid. Then the altitude vector becomes $\hat{\mathbf{h}} = h\hat{\mathbf{n}}$.

Once the altitude vector is obtained the next step is to obtain the semiaxes of the GT trajectory. For this we let ζ_s to remain fixed. After a time $t = t_1$ the attitude of the asteroid has changed by $\pi/2$ radians. Now a slice of the ellipsoid is taken along the $\eta\zeta$-plane resulting in an ellipse whose major and minor axes are b and c

respectively, allowing to the determination of η_s:

$$\eta_s = b\sqrt{1 - \left(\frac{\zeta_s}{c}\right)^2}. \tag{2.14}$$

Finally the semiaxes a_p and b_p of the reference trajectory are

$$a_p = \xi_0, \tag{2.15}$$

$$b_p = \eta_s + h\cos\theta, \tag{2.16}$$

where,

$$\theta = \sin^{-1}\left(\frac{\zeta_0 - \zeta_s}{h}\right). \tag{2.17}$$

The general control thrust $\mathbf{T_c}$ as given in Eq. (2.1) is

$$\frac{\mathbf{T_c}}{m} = \frac{\partial V}{\partial \mathbf{r}} - \begin{pmatrix} (a_p - b_p)4\omega^2\cos(2\omega + \phi_0)\cos\lambda_0 \\ (a_p - b_p)4\omega^2\sin(2\omega + \phi_0)\cos\lambda_0 \\ 0 \end{pmatrix}, \tag{2.18}$$

where,

$$\sin\lambda_0 = \frac{\zeta_0}{\|\mathbf{r}_0\|} \tag{2.19a}$$

$$\tan\phi_0 = \frac{\eta_0}{\xi_0}. \tag{2.19b}$$

The latitude λ_0 at which the GT hovers depends on the obliquity of the spin vector relative to the towing axis $\hat{\mathbf{i}}$. If the spin axis ζ, is aligned with the tow direction, then the GT will be hovering inertially over the body. On the contrary if ζ is normal

to the tow vector, the trajectory of the GT in the body-fixed frame of the asteroid will follow a concentric ellipse on the NEO equator with semiaxes $a_0 = a + h$ and $b_0 = b + h$.

Chapter 3

Dynamical Model

3.1 Introduction

This chapter presents the physical and dynamical models assumed for the asteroid and the GT spacecraft. The asteroid shape and the gravity field formulation are presented followed by the spacecraft configuration. The spacecraft configuration takes into account the location of the thrusters necessary to support the hovering dynamics. The spacecraft is sized based on historical information from the Dawn mission. A detailed model of the NSTAR thruster is described based on the work by Brophy [45]. The chapter closes with the description of a solar radiation model used for the simulations presented in Chapter 5.

3.2 NEO Physical Model

This section introduces the physical model used to represent an idealized asteroid on which the gravity tractor will hover. Several asteroid models are available in the literature. These models are based on approximated geometric shapes, spherical or

elliptical harmonic expansions, while others use multiple polyhedron approximations derived from derived from ground-based radar observations [46, 47, 48, 49] or *in-situ* spacecraft measurements [50, 51]. In this investigation the NEO is approximated as a triaxial ellipsoid whose gravity field can be solve in closed form by integration of elliptic functions.

3.2.1 Shape Model

Before proceeding with the discussion of the model, it is necessary to define the system of coordinates being used from now on. Two coordinate frames are defined here whose origin is at the asteroid center of mass. The first is coordinate system $\hat{\xi}$, $\hat{\eta}$, $\hat{\zeta}$ is fixed with the asteroid principal axes. In this reference frame $\hat{\xi}$ is aligned with the major semiaxis, $\hat{\zeta}$ with the minor semiaxis and $\hat{\eta}$ completes the orthogonal set following the right-hand rule. The second coordinate frame $\hat{\mathbf{i}}$, $\hat{\mathbf{j}}$, $\hat{\mathbf{k}}$ is assumed to be inertially fixed. Its principal direction $\hat{\mathbf{i}}$, is along the desired towing direction. The unit vector $\hat{\mathbf{j}}$ corresponds to the cross product of $\hat{\mathbf{i}}$ and the asteroid polar axis $\hat{\zeta}$. Finally the $\hat{\mathbf{k}}$ is obtained by the cross product between the $\hat{\mathbf{i}}$ and $\hat{\mathbf{k}}$ vectors.

To test the effectiveness of the hovering strategies introduced in section 2.2.2 it is convenient to define a set of ellipsoidal bodies to represent an idealized asteroid whose gravitational parameter $\mu = GM$ remains constant for the entire range of body ellipticities. The mass of a triaxial ellipsoid with semiaxes $a > b > c$ and uniform density distribution ρ is given by Eq. (3.1).

$$M = \frac{4}{3}\pi\rho abc \tag{3.1}$$

The semiaxes a and b are mutually related by the eccentricity e_{ab}, such that,

$$b = a\sqrt{1 - e_{ab}^2}\ . \tag{3.2}$$

The semiaxis c can be defined to be a fraction of b, say $c = b\epsilon$ such that $0 < \varepsilon < 1$. In this way the asteroid mass M can be written in terms of a and e_{ab} by substituting Eq. (3.2) into Eq. (3.1):

$$\begin{aligned} M &= \frac{4}{3}\pi\rho a^2\sqrt{1-e_{ab}^2}c \\ &= \frac{4}{3}\pi\rho a^2\sqrt{1-e_{ab}^2}\left(a\varepsilon\sqrt{1-e_{ab}^2}\right) \\ &= \frac{4}{3}\pi\rho a^3(1-e_{ab}^2)\varepsilon. \end{aligned} \tag{3.3}$$

Solving for the major semiaxis a gives,

$$a = \left(\frac{3M}{4\pi\rho\varepsilon\,(1-e_{ab}^2)}\right)^{1/3}. \tag{3.4}$$

Equation (3.4) allows to define the semimajor axis of the ellipsoid as a function of the eccentricity e_{ab} between the major and intermediate semiaxis a and b respectively. Consequently, the value of the intermediate semiaxis b is obtained from Eq. (3.2). The values of M, ρ and ε are arbitrary constants. Varying the eccentricity e_{ab} allows to generate different prolate bodies with the same gravitational parameter permitting to study the efficiency of the hovering modes on bodies with different axial dimensions. However, the shape of the gravitational field changes as the axial dimensions are altered.

3.2.2 Potential Field Model

The shape of a small celestial body can be approximated by a triaxial ellipsoid with semiaxes a, b and c. By changing the values of the semiaxes it is possible to change

the shape of the body from a sphere, ($a = b = c$) to an oblate ($a = b > c$) or prolate ($a > b = c$) spheroid. Thus a general triaxial ellipsoid can be defined by changing the values of a, b and c such that $a \geq b \geq c$. If the mass density ρ is assumed to be constant for a particular body, then its gravitational parameter μ can be determined as:

$$\mu = \frac{4}{3}\pi G\rho abc, \tag{3.5}$$

where $G = 6.6695 \times 10^{-11}$ $\mathrm{m^3kg^{-1}s^{-2}}$ is the universal gravitational constant.

The determination of the gravitational potential of a solid homogeneous triaxial ellipsoid at an exterior point $P_0 = (\xi_0, \eta_0, \zeta_0)$ is attributed to Sir James Ivory, 1809 [52]. The detailed derivation of this function is described by Danby, 1992 [53], MacMillan, 1958 [54] and Moulton, 1914 [55]. The resulting expression for the gravitational potential V is a function of elliptical integrals such that,

$$\begin{aligned} V(\xi, \eta, \zeta) = \frac{3}{4}\mu \int_{\kappa_0}^{\infty} \left(1 - \frac{\xi^2}{a^2+\kappa} - \frac{\eta^2}{b^2+\kappa} - \frac{\zeta^2}{c^2+\kappa}\right) \\ \times \frac{d\kappa}{\sqrt{(a^2+\kappa)(b^2+\kappa)(c^2+\kappa)}}. \end{aligned} \tag{3.6}$$

Equation (3.6) maps the gravitational potential V of a solid homogeneous ellipsoid with semiaxes a, b and c to the exterior point P_0. The lower limit of integration κ_0 defines a confocal ellipsoid $E(\kappa)$ that passes through the point P_0. The equation of the auxiliary ellipsoid is given by:

$$E(\kappa) = \frac{\xi^2}{a^2+\kappa} + \frac{\eta^2}{b^2+\kappa} + \frac{\zeta^2}{c^2+\kappa} - 1. \tag{3.7}$$

Equation (3.7) has three real roots, two are negative and one is positive. The only root that keeps the denominators of Eq. (3.7) positive is the largest root of $E(\kappa)$ that

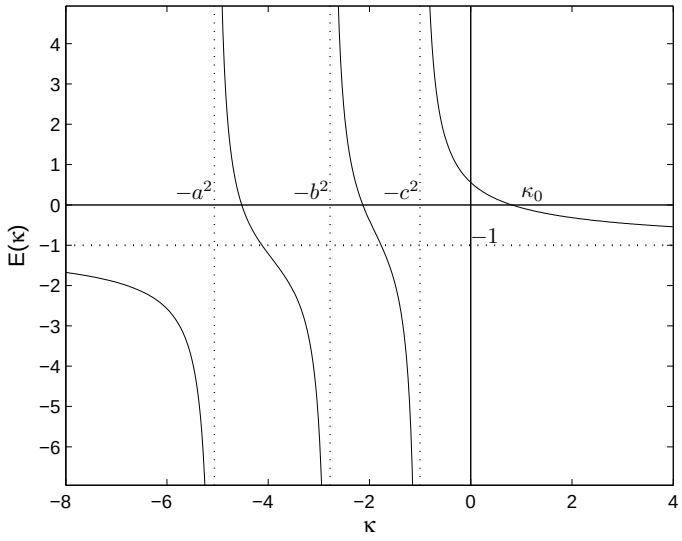

Figure 3.1: Roots of $E(\kappa)$: The only positive root $\kappa = \kappa_0$ defines the auxiliary concentric ellipsoid passing through the exterior point P_0.

defines the lower limit of integration κ_0 in Eq. (3.6). The graph of $E(\kappa)$ is shown in Fig. 3.1.

Upon integration of Eq. (3.6) the gravitational potential $V(\xi, \eta, \zeta)$ results in a function of Legendre's canonical elliptic integrals $F(\phi_l, k_l)$ and $E(\phi_l, k_l)$ of first and second kind, respectively. The amplitude ϕ_l and modulus k_l are of the elliptic integrals are:

$$\sin \phi_l = \sqrt{\frac{a^2 - c^2}{\kappa + a^2}}, \tag{3.8}$$

$$k_l = \sqrt{\frac{a^2 - b^2}{a^2 - c^2}}. \tag{3.9}$$

The expression for the potential function $V(\xi, \eta, \zeta)$ becomes:

$$V(\xi,\eta,\zeta) = \frac{2\pi G\rho abc}{\sqrt{a^2-c^2}}\Bigg[\left(1 - \frac{\xi^2}{a^2-b^2} + \frac{\eta^2}{a^2-b^2}\right) F(\phi_l, k_l) + \left(\frac{\xi^2}{a^2-b^2} + \frac{(c^2-a^2)\,\eta^2}{(a^2-b^2)(b^2-c^2)} + \frac{\zeta^2}{b^2-c^2}\right) E(\phi_l, k_l) + \left(\frac{c^2+\kappa}{b^2-c^2}\eta^2 - \frac{b^2+\kappa}{b^2-c^2}\zeta^2\right)\left(\frac{a^2-c^2}{(a^2+\kappa)(b^2+\kappa)(c^2+\kappa)}\right)^{1/2}\Bigg]. \quad (3.10)$$

The components of gravitational attraction of the triaxial ellipsoid are obtained from the gradient of the potential. Taking the partial derivative of V with respect to ξ, η and ζ yields:

$$\frac{\partial V}{\partial \xi} = \frac{\Gamma}{(a^2-b^2)}\left[E(\phi_l, k_l) - F(\phi_l, k_l)\right]\xi, \quad (3.11a)$$

$$\frac{\partial V}{\partial \eta} = \Gamma\left[\frac{(-a^2+c^2)\,E(\phi_l, k_l)}{(a^2-b^2)(b^2-c^2)} + \frac{F(\phi_l, k_l)}{a^2-b^2} + \Lambda\frac{(c^2+\lambda)}{b^2-c^2}\right]\eta, \quad (3.11b)$$

$$\frac{\partial V}{\partial \zeta} = \frac{\Gamma}{(c^2-b^2)}\left[-E(\phi_l, k_l) + \left(b^2+\lambda\right)\Lambda\right]\zeta, \quad (3.11c)$$

where Γ and Λ are auxiliary defined as

$$\Gamma = \frac{4\pi G\rho abc}{\sqrt{a^2-c^2}}, \quad (3.12)$$

$$\Lambda = \sqrt{\frac{a^2-c^2}{(a^2+\lambda)(b^2+\lambda)(c^2+\lambda)}}. \quad (3.13)$$

Mind that the semiaxes a, b and c need to be distinct in order to avoid numerical singularities. The evaluation of the elliptic integrals are carried out using robust

numerical procedures for example, see section 6.11 in Ref. [56].

3.3 Gravity Tractor Model

To provide a realistic framework in which we can make educated assumptions on the mass budget of our GT spacecraft, we relied on historical information from two spacecraft missions employing low-thrust propulsion: Deep Space 1 and Dawn. Deep Space 1 (DS1) was a technology-validation mission launched on October 24, 1998 towards comet Borrelly [37]. The Dawn spacecraft was launched on September 27, 2007 and is expected to rendezvous with two major main belt asteroids: Vesta in July 2011 and with Ceres in February 2015.[1]

We consider the GT to be small spacecraft with a mass of about 1000 kg at the beginning of the hovering stage powered by a set of ion engines similar to the NSTAR thruster flown in DS1 and Dawn missions. Figure 3.2 shows a general layout of the GT spacecraft inspired from the earlier works by Yeomans *et al.,* [39, 33]. The spacecraft bus is represented by the central box and the gray cones represent the main thrusters. A set of five ion thruster are used to control the three-dimensional translational dynamics. Thrusters labeled T_1, T_2 and T_3 combine to control the motion in the $\hat{\mathbf{i}}\hat{\mathbf{k}}$-plane whereas thrusters T_4 and T_5 control the dynamics along the $\hat{\mathbf{j}}$-axis. Thrusters T_1 and T_2 are slanted to prevent plume impingement on the asteroid. The solar arrays extend along the $\hat{\mathbf{k}}$-axis and are sized in Sec. 3.3.1.

The mass budget for the GT system was estimated based on information available from the Dawn mission. The rationale behind this decision is a set of common factors between the two spacecrafts. Among these factors we find both spacecrafts, the GT and Dawn, have a box-shaped bus, large solar arrays and both spacecraft are intended to operate under the gravitational field of an asteroid. Although their

[1]Dawn mission website, http://dawn.jpl.nasa.gov/mission/.

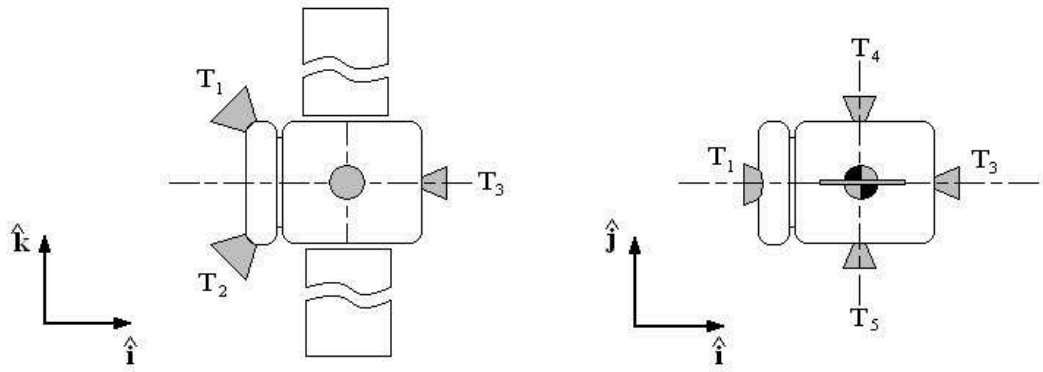

Figure 3.2: Thrusters layout for the xGT spacecraft.

similar propulsion architecture, the GT uses its NSTAR thrusters to support hovering instead of interplanetary cruise. We believe their similarities allow for relatively easy extrapolation of the subsystem requirements and mass budget.

The mass of the NSTAR ion propulsion system (IPS) is disclosed into its major components in Table 3.1. The table is divided in three column sections. The components are indicated on the left column followed by their mass as found in Refs. [38, 57]. The center section indicates the number of units of each component for the GT spacecraft and its mass cost, respectively. The right column indicates the number of units included in the Dawn spacecraft as found in Ref. [57]. The digital control interface unit (DCIU) controls the the xenon feed system (XFS) and the power processing unit (PPU), executing high level commands from the spacecraft computer. Two DCIU are installed in the Dawn spacecraft to provide redundancy. The gimbals are used to control the thrust direction, but in the GT are used to control the canting angle of T_1 and T_2. The XFS distributes the Xe propellant to the engines. A 10% contingency was added to the total mass budget.

The mass contribution from the spacecraft subsystems is given in Table 3.2. The bulk mass of the spacecraft bus and related mechanical components is indicated on the first row. The electric power system (EPS) comprises the solar array structure

Table 3.1: Propulsion system mass budget.

		GT		Dawn [57]	
Component	Mass, kg/unit	Units	Mass, kg	Units	Mass, kg
NSTAR ion engine	8.2	5	41.0	3	24.6
DCIU	5.85	2	11.7	2	11.7
PPU	13.9	5	69.5	2	27.8
Gimbals	4.6	2	9.2	3	13.8
XFS baseline	8.1	1	8.1	1	8.1
Additional per engine	3.3	5	16.5	3	9.9
Xe tank mass fraction %		4.5	6.8	4.5	20.3
Net IPS hardware mass			162.5		116.2
Mass contingency %		10	16.2	10	11.6
Total IPS mass			**179**		**128**

and auxiliary cabling and circuits. The total mass of the EPS was estimated from the solar array mass by a factor of 4, resulting in good agreement with the data obtained from Dawn. The attitude control system (ACS) controls the spacecraft orientation by means of reaction wheels or by the reaction control system (RCS). The RCS utilizes hydrazine mono propellant. The thermal control system (TCS) regulates the spacecraft temperature. The command and data handling subsystem (CDHS) processes and distributes commands to other subsystems and stores mission data. The telecommunications subsystem provides communication link with Earth. It is likely that an asteroid deflection mission will require to perform some scientific characterization of the the target. Therefore we also allocated scientific payload mass assuming a similar set of instruments as those carried in the Dawn spacecraft. Table 3.3 indicates the amount of propellant mass and the spacecraft gross weight at the beginning of the mission. It is important to remind the reader that the initial mass of the GT is considered at the beginning of the hovering stage while the mass of the Dawn spacecraft reflect the launch mass. Therefore, the mass budget presented

Table 3.2: Miscellaneous subsystems mass.

		GT		Dawn [38]	
Subsystem	Mass, kg/unit	Units	Mass, kg	Units	Mass, kg
Mech/Struct/Harn/Balance	203	1.5	305	1	203
EPS	53	4	213	1	204
ACS	37	1	37	1	37
RCS	14	1	14	1	14
TCS	44	1	44	1	44
CDHS	21	1	21	1	21
Telecom	28	1	28	1	28
Science	45	1	45	1	45
Mass uncertainty			20		20
Total Miscellaneous			**726**		**616**

Table 3.3: Spacecraft gross mass.

	GT	Dawn [38]
	Mass, kg	Mass, kg
Xenon	100	450
Hydrazine	45	45
IPS	179	128
Misc. subsystem	726	616
Net spacecraft mass	**1050**	**1239**

here does not account for the total launch mass.

3.3.1 Solar Array

The roll of the solar array is to transform the energy from the solar photons into electric current in order to supply power to the spacecraft subsystems. In the case of a spacecraft equipped with solar-electric engines, most of the power produced by the solar panels is fed into the propulsion system. In fact, the power budget of the

Dawn spacecraft was around 3.1 kW of which 2.5 kW were used by the IPS [58]. The TCS consumed a maximum of 200 W at 3 AU and the telecoms system X-band transponder required 100 W. The Dawn solar array panels comprised a net area of 36 m^2 capable of generating 10.3 kW at 1 AU and 1.3 kW at 3 AU [38].

Similarly, the GT power load is driven by the five engines comprising the IPS. The engines controlling the dynamics along the $\hat{\mathbf{j}}$-direction (i.e. T_4 and T_5) thrust in opposite directions and therefore only one engine may be needed to fire at maximum power. On the other hand, thrusters T_1, T_2 and T_3 may fire simultaneously at any time although not all of them at full power. From this information, and under a conservative stand point we could estimate the IPS power load to be equivalent to four engines operating at full throttle plus an additional 10% for the remaining GT subsystems resulting in a net power load of 11 kW. The size of the solar array is a function of the power load, P_{load} and the heliocentric distance, R. The area of the solar array A is,

$$A_{sa} = \frac{P_{load}\mathcal{R}^2}{\nu_{cell}\mathcal{F}_0}, \tag{3.14}$$

where $\mathcal{F}_0 = 1.36\text{kW/m}^2$ is the solar flux at 1 AU, $\mathcal{R}$ is the heliocentric distance in AU and ν_{cell} is the efficiency of the solar cells. Fatemi *et al.,* reported on the efficiency of the triple-junction InGa/InGaAs/Ge to be $\nu_{cell} = 27.6\%$ [59]. Each NSTAR engine operating at full throttle requires 2.5 kW of power. If we assume four engines operating simultaneously at their maximum capacity at a maximum heliocentric range of 1.1 AU, then the total area of the solar array is 35.5 m^2.

3.3.2 Propulsion System

Ion propulsion systems generate thrust by ionizing a gas, usually xenon (Xe), and accelerating the ions through an electric potential. The accelerated Xe ions are expelled

with velocities in the order of 10^2 km/s. The efficiency of ion thrusters range between 60% and 80% [60] p. 4. In practice, ion engines are often used for north-south stationkeeping of satellites on geosynchronous orbits and in the last decade they have been used in interplanetary missions as the primary propulsion system. The NSTAR ion engine was designed to be throttled up or down in order to adjust to the varying solar power available at various heliocentric distances.

The mass-flow rate equation of the electric thruster is

$$\dot{m}_p = \frac{T^2}{2\eta_T P_{in}}, \tag{3.15}$$

where η_T is the thruster efficiency and P_{in} is the power supplied to the thruster. The specific impulse can be written as,

$$I_{sp} = \frac{2\eta_T P_{in}}{g_0 T}. \tag{3.16}$$

Substituting Eq. (3.16) into Eq. (3.15), results in the classical rocket equation,

$$\dot{m}_p = \frac{T_{net}}{g_0 I_{sp}}, \tag{3.17}$$

where $T_{net} = \sum_{i=1}^{5} T_i$ is the net thrust supplied by the engines at a given time and $g_0 = 9.81$ m/s^2 is the acceleration of Earth's gravity at sea level. The I_{sp} values for each throttle setting are given in Table 3.4[2] , where the minimum and maximum thrust settings are $T_{min} = 0.020$ N and $T_{max} = 0.092$ N, respectively. The I_{sp} data was fitted into a fourth-order polynomial to generate a continuous function of I_{sp} vs. thrust. Then, for each thruster the I_{sp} is determined by

$$I_{sp} = A_0 T^4 + B_0 T^3 + C_0 T^2 + D_0 T + E_0, \tag{3.18}$$

[2]The units of flow rate are given in standard cubic centimeter per minute (sccm). For xenon ions, 1 sccm= 0.0983009 [mg/s] (see Ref. [60], page 464).

where the coefficients of the polynomial are: $A_0 = -4.170 \times 10^8$ sec/N^4, $B_0 = 1.046 \times 10^8$ sec/N^3, $C_0 = -9.628 \times 10^6$ sec/N^2, $D_0 = 3.887 \times 10^5$ sec/N and $E_0 = -2.751 \times 10^3$ sec and T is the applied thrust in units of Newtons (N). Figure 3.3(a) shows the fit along with the original data. The propellant mass rate follows a near linear relation with respect to the applied thrust except near the lower limit T_{min} (Fig. 3.3(b)).

The amount of thrust supplied by each engine is the vector sum of the required acceleration in the $\hat{\mathbf{i}}$, $\hat{\mathbf{j}}$ and $\hat{\mathbf{k}}$ directions. The canted orientation of thrusters T_1 and T_2 requires the introduction of a mixing algorithm to command the engines to provide the correct amount of thrust T_i (for $i = 1, .., 5$), along the desired coordinate. Therefore, given the components of acceleration a_x, a_y and a_z, the mixing logic for thrusters T_1, T_2 and T_3 is defined as follows:

$$T_1 = \begin{cases} \frac{m|a_x|}{2\cos\beta} + \frac{m|a_z|}{\sin\beta}, & \text{if } a_x > 0 \text{ and } a_z \leq 0; \\ \frac{m|a_z|}{\sin\beta|}, & \text{if } a_x = 0 \text{ and } a_z \leq 0; \\ 0, & \text{otherwise.} \end{cases} \tag{3.19a}$$

$$T_2 = \begin{cases} \frac{m|a_x|}{2\cos\beta} + \frac{m|a_z|}{\sin\beta}, & \text{if } a_x > 0 \text{ and } a_z \geq 0; \\ \frac{m|a_z|}{\sin\beta|}, & \text{if } a_x = 0 \text{ and } a_z \geq 0; \\ 0, & \text{otherwise.} \end{cases} \tag{3.19b}$$

$$T_3 = \begin{cases} m\,|a_x| + \frac{m|a_z|\cos\beta}{\sin\beta}, & \text{if } a_x < 0 \text{ and } a_z \neq 0; \\ \frac{m|a_z|\cos\beta}{\sin\beta}, & \text{if } a_x = 0 \text{ and } a_z \neq 0; \\ 0, & \text{otherwise.} \end{cases} \tag{3.19c}$$

The mixing logic for thrusters T_4 and T_5 is rather simple. These thrusters fire in op-

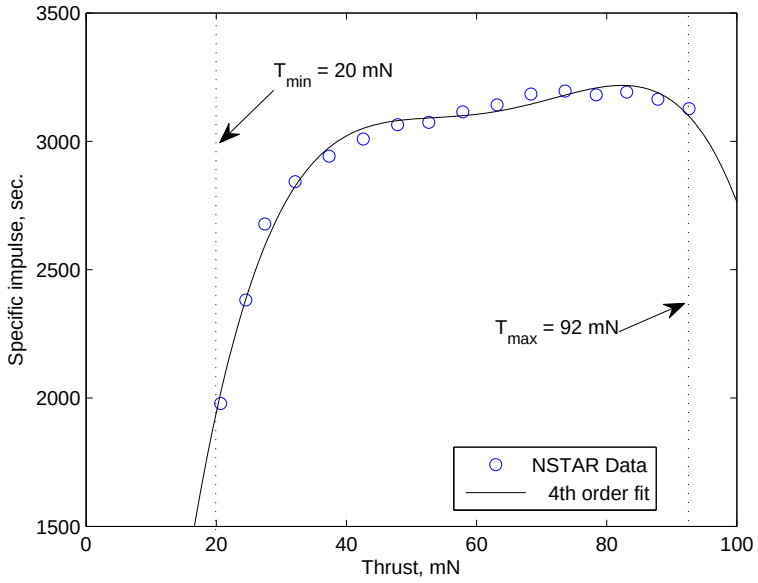

(a)

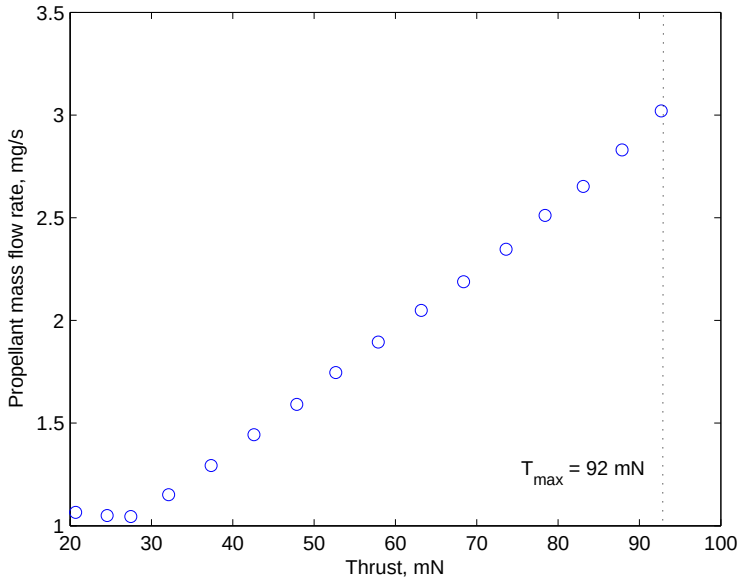

(b)

Figure 3.3: NSTAR Engine performance plots.

Table 3.4: Throttle table of the NSTAR thruster. [45]

Throttle level	PPU input power, kW	Engine input power, kW	Calculated thrust, mN	Main flow rate, sccm	Cathode flow rate, sccm	Neutralizer flow rate, sccm	Isp, s	Thruster efficiency
15	2.567	2.325	92.67	23.43	3.70	3.59	3127	0.618
14	2.416	2.200	87.87	22.19	3.35	3.25	3164	0.624
13	2.272	2.077	83.08	20.95	3.06	2.97	3192	0.630
12	2.137	1.960	78.39	19.86	2.89	2.80	3181	0.628
11	2.006	1.845	73.60	18.51	2.72	2.64	3196	0.631
10	1.842	1.717	68.37	17.22	2.56	2.48	3184	0.626
9	1.712	1.579	63.17	15.98	2.47	2.39	3142	0.618
8	1.579	1.456	57.90	14.41	2.47	2.39	3115	0.611
7	1.458	1.344	52.67	12.90	2.47	2.39	3074	0.596
6	1.345	1.238	47.87	11.33	2.47	2.39	3065	0.590
5	1.222	1.123	42.61	9.82	2.47	2.39	3009	0.574
4	1.111	1.018	37.35	8.30	2.47	2.39	2942	0.554
3	0.994	0.908	32.12	6.85	2.47	2.39	2843	0.527
2	0.825	0.749	27.47	5.77	2.47	2.39	2678	0.487
1	0.729	0.659	24.55	5.82	2.47	2.39	2382	0.472
0	0.577	0.518	20.69	5.98	2.47	2.39	1979	0.420

posite directions and their firing sequence is evaluated under the following conditions:

$$T_4 = \begin{cases} m\,|a_y|\,, & \text{if } a_y < 0; \\ 0, & \text{otherwise.} \end{cases} \tag{3.20a}$$

$$T_5 = \begin{cases} m\,|a_y|\,, & \text{if } a_y > 0; \\ 0, & \text{otherwise.} \end{cases} \tag{3.20b}$$

Differential thrust balance

Upon determination of the thruster firing mix, we need to evaluate whether the resulting amount of thrust is inside the operational range of the engine. The data in Table 3.4 indicates the operational range of the NSTAR engine is between 20 mN and 92 mN. If at a given time the thrust to be applied falls below the 20 mN threshold, then the engine fires at its lower limit and engines in the opposite direction switch-on to compensate for the excess thrust. For all engines the following condition must be satisfied:

$$T_i + \delta a \geq T_{min}, \tag{3.21}$$

where $i = 1, 2, 3, 4, 5$. For engines T_1, T_2 and T_3 we have,

$$\delta a_1 \geq T_{min} - T_1, \tag{3.22a}$$

$$\delta a_2 \geq T_{min} - T_2, \tag{3.22b}$$

$$\delta a_3 \geq \frac{T_{min} - T_3}{2\cos\beta}, \tag{3.22c}$$

where,

$$\delta a = \max\left(\delta a_1, \delta a_2, \delta a_3\right). \tag{3.23}$$

Equation (3.22) guarantees that Eq. (3.21) is satisfied for thrusters T_1, T_2 and T_3. For engines T_4 and T_5, T_{min} is added to both thrusters in addition to the input required to provide thrust in the commanded direction. The mixing logic is defined as,

$$\text{if } T_4 < T_{min} \Rightarrow \begin{cases} T_4 & = T_4 + T_{min} \\ T_5 & = T_{min} \end{cases} \tag{3.24a}$$

$$\text{if } T_5 < T_{min} \Rightarrow \begin{cases} T_5 & = T_5 + T_{min} \\ T_4 & = T_{min} \end{cases} \tag{3.24b}$$

Otherwise, the logic given in Eqs. (3.20) applies.

3.3.3 Engine Canting Angle

In section 2.2.1 we found that the minimum engine can angle for the special case of a GT hovering over an spherical body is,

$$\beta = \arcsin\frac{a}{d} + \phi_{phw}.$$

In this section we solve the problem of the engine minimum slant angle for the general case where the NEO is a triaxial ellipsoid of semiaxes a, b and c and the GT spacecraft position is $\mathbf{r}_0 = [x_0, y_0, z_0]$ from the center of mass of the NEO. Our goal is achieved by finding the point of tangency, $P_s = [x_s, y_s, z_s]$ on the surface of the ellipsoid

that belongs to the vector intersecting the point $P_0 = [x_0, y_0, z_0]$, (recall that P_0 corresponds to the locus of the spacecraft). Finding the point P_s requires to solve a system of three equations whose unknowns are x_s, y_s and z_s.

The first equation is given by the algebraic form of a triaxial ellipsoid centered at the origin of the coordinate system $\hat{\mathbf{i}}$, $\hat{\mathbf{j}}$, $\hat{\mathbf{k}}$ defined earlier in Sec. 3.2.1:

$$f(x, y, z) = A_0x^2 + B_0y^2 + 2C_0z^2 + 2D_0xy + 2E_0xz + 2F_0yz + G_0. \tag{3.25}$$

where $G_0 = -abc$ and the coefficients, A_0, B_0, C_0, D_0, E_0 and F_0 are due to the relative orientation of the ellipsoid axes with respect to the frame $\hat{\mathbf{i}}$, $\hat{\mathbf{j}}$, $\hat{\mathbf{k}}$. To obtain the remaining coefficients, let $\mathbf{Q}$ be the matrix representing the ellipsoid with its axes of inertia aligned with the reference frame such that,

$$\mathbf{Q} = \begin{pmatrix} \frac{bc}{a} & 0 & 0 \\ 0 & \frac{ac}{b} & 0 \\ 0 & 0 & \frac{ab}{c} \end{pmatrix}. \tag{3.26}$$

Following a coordinate transformation yields,

$$\mathbf{Q}' = \mathbf{R}_1^T\mathbf{R}_2^T\mathbf{Q}\mathbf{R}_2\mathbf{R}_1, \tag{3.27}$$

where,

$$\mathbf{R}_1 = \begin{pmatrix} \cos\lambda & 0 & \sin\lambda \\ 0 & 1 & 0 \\ -\sin\lambda & 0 & \cos\lambda \end{pmatrix}, \tag{3.28}$$

is a rotation about the η-axis by a latitude λ and

$$\mathbf{R}_2 = \begin{pmatrix} \cos\theta & \sin\theta & 0 \\ -\sin\theta & \cos\theta & 0 \\ 1 & 0 & 1 \end{pmatrix}, \tag{3.29}$$

is rotation about the ζ-axis by the longitude θ. From Eq. (3.27), $\mathbf{Q}'$ can be written explicitly in terms of the coefficients in Eq. (3.25):

$$\mathbf{Q}' = \begin{pmatrix} A_0 & D_0 & E_0 \\ D_0 & B_0 & F_0 \\ E_0 & F_0 & C_0 \end{pmatrix}. \tag{3.30}$$

The second equation corresponds to the plane tangent to the ellipsoid that contains P_s and P_0 or,

$$\mathbf{n}_s \cdot (\mathbf{r}_s - \mathbf{r}_0) = 0, \tag{3.31}$$

where

$$\mathbf{n}_s = \nabla f\left(x_s, y_s, z_s\right), \tag{3.32}$$

and $\mathbf{r}_s = [x_s, y_s, z_s]$ is the vector from the origin to the surface of the ellipsoid. The third equation corresponds to a plane defined by the points P_0, P_s and $P_k = [0, 0, 1]$ which yields,

$$\mathbf{n}_k \cdot (\mathbf{r}_s - \mathbf{r}_0) = 0, \tag{3.33}$$

where,

$$\mathbf{n}_k = \overrightarrow{P_0 O} \times \overrightarrow{P_0 P_k}. \tag{3.34}$$

The intersection of the planes defined by Eqs. (3.31) and (3.33) is the line tangent to

$f(x_s, y_s, z_s) = 0$ that intersects P_0. Equations (3.25), (3.31) and (3.33) conform an algebraic system of three nonlinear algebraic equations with three unknowns i.e.,

$$A_0x^2 + B_0y^2 + Cz^2 + D_0xy + E_0xz + F_0yz + G = 0 \tag{3.35a}$$

$$\nabla f\left(x_s, y_s, z_s\right) \cdot \left(\mathbf{r}_s - \mathbf{r}_0\right) = 0 \tag{3.35b}$$

$$\mathbf{n}_2 \cdot \left(\mathbf{r}_s - \mathbf{r}_0\right) = 0 \tag{3.35c}$$

Finding an analytical solution of Eq. (3.35) is cumbersome therefore, a numerical method such as the Gauss-Newton is desirable. A numerical routine of this kind can be implemented by invoking the function *fsolve.m* in Matlab. However, an analytical solution is easier to find under the assumption that P_0 lies on the $\hat{\mathbf{i}}\hat{\mathbf{j}}$-plane. Such assumption causes the $\hat{\mathbf{j}}$-coordinate to be zero because the tangent lines containing P_0 and P_s are embedded in the $\hat{\mathbf{i}}\hat{\mathbf{j}}$-plane as well, reducing the system in Eq. (3.35) into two equations and two unknowns,

$$A_0x_s^2 + C_0z_s^2 + 2E_0x_sz_s + G_0 = 0, \tag{3.36a}$$

$$z_s + \frac{A_0x_s + E_0z_s}{C_0z_s + E_0x_s}(x_s - x_0) = 0. \tag{3.36b}$$

The solution to the system in Eqs. (3.36) is,

$$x_s = \frac{-G_0 \mp \frac{E_0\sqrt{-G_0\left(G_0 + A_0x_0^2\right)}}{\sqrt{\left(A_0C_0 - E_0^2\right)}}}{A_0x_0}, \tag{3.37a}$$

$$z_s = \pm\frac{\sqrt{-G_0\left(G_0 + A_0x_0^2\right)}}{x_0\sqrt{\left(A_0C_0 - E_0^2\right)}}. \tag{3.37b}$$

The relevance of the analytical solution (3.37a) is that allows to use them as the

initial guess when solving solving Eq. (3.35) numerically and reducing computational time. Finally, the engine canting angle is the bisection of the angle formed between $\mathbf{r}_0$ and the two solutions to Eqs. (3.35) i.e.,

$$\beta = \frac{1}{2}\left(\sin^{-1}\frac{z_{s_1}}{\|\mathbf{r}_0 - \mathbf{r}_{s_1}\|} + \sin^{-1}\frac{z_{s_2}}{\|\mathbf{r}_0 - \mathbf{r}_{s_2}\|}\right) + \phi_{phw}. \tag{3.38}$$

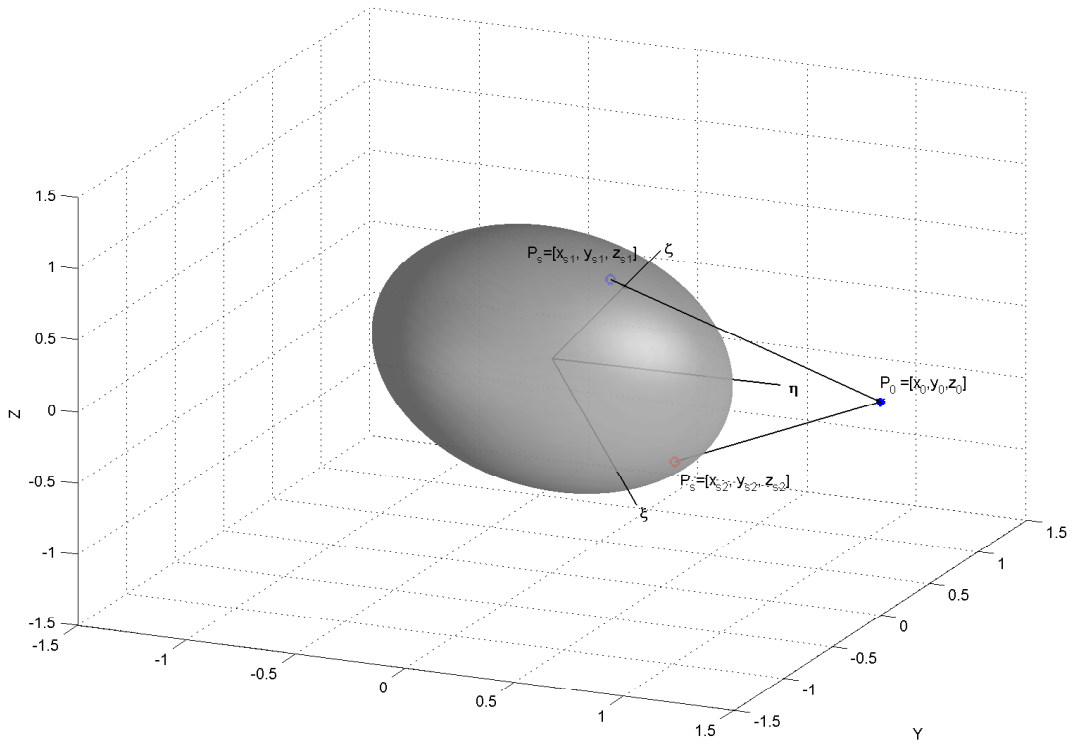

Figure 3.4: Tangent vectors connecting $\mathbf{r}_0$ to the points in the surface of the ellipsoid.

3.4 Radiation Pressure Model

The large area of the solar arrays, in combination with the prolonged operations in the proximity of the asteroid, motivates the inclusion of the disturbing forces due to solar radiation. Over extended periods of time, these small perturbations may cause the GT spacecraft to drift away from its prescribed hovering position putting the

mission at risk. The solar flux at 1 AU is approximately $\mathcal{F}_0 = 1367$ W/m^2 [61] and decreases with the inverse square of the heliocentric distance $\mathcal{R}$,

$$\mathcal{F} = \mathcal{F}_0 \frac{1}{\mathcal{R}^2}. \tag{3.39}$$

The acceleration due to solar radiation pressure can be estimated by modeling the size of main reflective surfaces of the spacecraft and its orientation with the Sun's normal. In this case we consider the solar array to be flat Lambertian surfaces oriented perpendicular to the photons flux as shown in Fig. 3.5. The force acting on the spacecraft due to solar radiation pressure is calculated as,

$$\mathbf{F}_{sp} = \mathcal{P} A_{sa} \left[(1 + \rho_s) + \frac{2}{3} \rho_d \right] \hat{\mathbf{n}}, \tag{3.40}$$

where $\mathcal{P} = 3 \times 10^{-8} \mathcal{F}$ is the pressure due to the solar photons and A_{sa} is the area of the solar array. The coefficients of specular reflection ρ_s, diffuse reflection ρ_d and absorbed radiation ρ_a satisfy $\rho_a + \rho_s + \rho_d = 1$. Because solar panels are mostly absorber surfaces we assume $\rho_a = 0.7$, $\rho_s = 0.15$ and $\rho_d = 0.15$ [62].

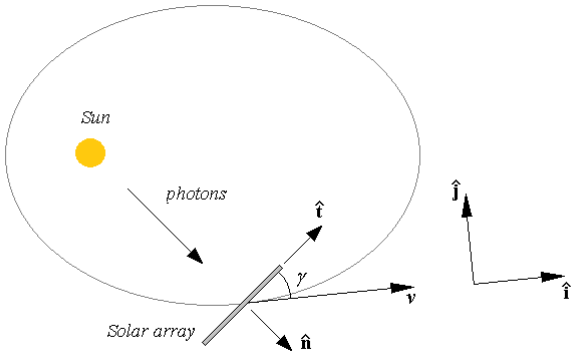

Figure 3.5: Solar radiation pressure model.

Chapter 4

Results on the xGT Performance

4.1 Introduction

In this chapter we report on the results of a parametric study done in order to gather a first-order insight regarding the performance of the GT spacecraft operating under the dynamic hovering laws *versus* the classical inertial hovering. The analysis consisted in determining the amount of towing Δv and propellant consumption of the GT when it has to operate over bodies of different rotation periods and shapes, as described in 3.2.1. This chapter is divided in two major parts. First we perform a parametric analysis using an ideal ion engine of constant specific impulse, $I_{sp} = 3000$ sec. In the second part of this chapter the same analysis is done but using the NSTAR engine model described in section 3.3.2.

4.2 Simulation Parameters

The physical parameters of the asteroid are quantified in Table 4.1. The shape of the asteroid is determined by Eqs. (3.2) and (3.4) for values of $0.05 \geq e_{ab} \leq 0.90$. The

spin rates are defined by rotation periods ranging from 2 hours to 1 revolution per day. The spin vector is assumed to be along the principal axis of inertia c, orthogonal to the desired Δv vector, which is the vector pointing from the asteroid center of mass towards the GT spacecraft, and perpendicular to the orbit plane. These conditions allow to place the GT spacecraft in the equatorial plane of the asteroid at an arbitrary initial altitude $h = 80$ m from the surface.

In practice, there is no defined upper bound for the rotation period. For example, asteroid 99942 Apohis has a rotation period of 30 hours while others could have periods lasting several days. The lower boundary of the rotation period has been found to be near 0.1 days ($\approx$ 2.4 hours) for asteroids with diameters greater that 200 meters. This spin limit is thought to be due to a purely gravitational regime that hold these bodies together.[63, 64]

Table 4.1: Asteroid Parameters.

Density, kg/m^3	Mass, kg	e_{ab}	ε	Period, hs
2300	2.6×10^{10}	[0.05 - 0.9]	0.75	[2 - 24]

The equations of motion (Eq. (2.1)) were integrated in an inertial frame with origin at the asteroid center of mass. The gravitational pull on the spacecraft was obtained by transforming the position vector into body-fixed coordinates. The first rotation $\mathbf{C}_\eta$, is about the intermediate body axis $\hat{\eta}$, by the respective latitude angle λ, resulting in the new orientation of the polar axis $\hat{\zeta}$ with respect to $\hat{\mathbf{i}}$. Recall that the $\hat{\mathbf{i}}$-axis corresponds to the direction of towing. The second rotation $\mathbf{C}_\zeta$, is about the $\hat{\zeta}$-axis by the longitude angle ϕ. Alternatively, the polar axis may not necessarily be normal to the $\hat{\mathbf{i}}\hat{\mathbf{j}}$-axis. In such case, a rotation about the $\hat{\mathbf{i}}$-axis by an angle ψ precedes

the former transformation resulting in the general sequence,

$$\begin{pmatrix} \xi_0 \\ \eta_0 \\ \zeta_0 \end{pmatrix} = \mathbf{C}_\zeta(\phi)\mathbf{C}_\eta(\lambda)\mathbf{C}_{\hat{\mathbf{i}}}(\psi) \begin{pmatrix} x_0 \\ y_0 \\ z_0 \end{pmatrix}. \tag{4.1}$$

The numerical simulation was done using the Matlab integrator *ode113* with an absolute tolerance 10^{-6} and a relative tolerance of 10^{-8}. In order to obtain more accurate results and to prevent numerical artifacts due to the different integration step-sizes *ode113* may use for the different simulation cases, we restricted the maximum integration step-size to 1/50 times the rotation period of the asteroid. The total simulation time was 20 days and the results (i.e., Δv and Δm) are presented as the daily average.

4.3 Ideal Ion Engine

The gravitational action of the GT on the asteroid produces an acceleration

$$\dot{v} = \frac{Gm(t)}{r^2}, \tag{4.2}$$

where r is the distance from the asteroid center of mass and $m(t)$ accounts for the decreasing mass of the spacecraft. The change in mass is given by the ideal rocket equation (i.e., Eq. (3.17)). Combining Eqs. (3.17) and (4.2) the net Δv imparted on the NEO over the towing period is estimated as,

$$\Delta v = \frac{Gm_0 I_{sp} g_0}{a_{net} r^2} \left(1 - \exp^{-\frac{a_{net}}{I_{sp} g_0} \Delta t} \right), \tag{4.3}$$

where $a_{net} = T_{net}/m$. Recall that the second term on the right of Eq. (2.6),

$$\frac{\mathbf{T}_c}{m} = -\frac{\partial V}{\partial \mathbf{r}} - \omega_{gt}^2 \frac{a-b}{2} \cos(\omega_{GT} t)\, \hat{\mathbf{i}},$$

indicates that the distance between the centers of mass of the asteroid and spacecraft changes periodically. Therefore, the Δv on the asteroid due to the xGT is estimated using the average hovering distance over the towing period Δt.

Figure 4.1 shows the Δv exerted by a GT with initial mass $m_0 = 1050$ kg while hovering inertially from the center of mass of a triaxial body of varying shapes, constant gravitational parameter $\mu = GM$ and constant density distribution ρ. The Δv imparted on the asteroid due the gravitational pull of the GT is mapped against the eccentricity between semiaxes a and b, and the rotation period of the body. The color scale indicates the averaged daily propellant consumption. The altitude h, in addition to the extension of the semimajor axis, determine the hovering position with respect to the center of mass of the asteroid. Therefore, larger axial eccentricities e_{ab}, cause the GT to hover farther from the center of mass, decreasing the towing Δv imparted on the asteroid. This effect is shown in Fig. 4.1 where the Δv decreases as the axial eccentricity increases. The Δv given in Eq. (4.3) is the component of acceleration exerted by the GT on the NEO in the direction parallel to the desired towing axis $\hat{\mathbf{i}}$. Note the towing performance for a GT operating in inertial hovering is independent from the asteroid rotation rate. The propellant depletion is indicated by the color scale of Fig. 4.1. As expected the propellant usage decreases as the bodies become more eccentric as a consequence of increased distance from the asteroid center of mass.

Figures 4.2(a) and 4.2(b) display the towing Δv exerted on the asteroid by the xGT operating in the one-dimensional dynamic hovering (xGT1) and in the two-dimensional dynamic hovering (xGT2), respectively. Both strategies yield the same Δv, an expected result since the average position along the $\hat{\mathbf{i}}$ direction is the same for the xGT1 and xGT2. The towing Δv is mapped against the shape and rotation period of the asteroid. The increase in Δv for the xGT depends on the amplitude of the spacecraft displacement along the towing axis. Such displacement has been defined

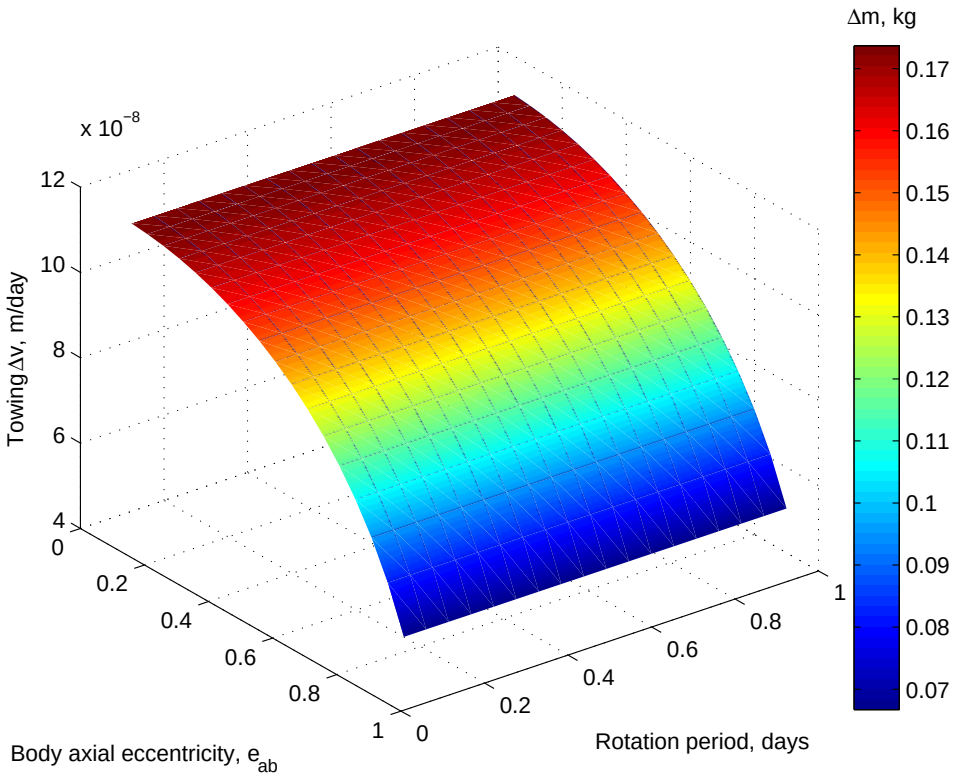

Figure 4.1: Towing Δv exerted by a GT operating in inertial hovering. The color scale indicates the propellant mass used over a 24 hrs interval.

to be the difference between the major and intermediate semiaxes of the NEO (see section 2.2.2).

The merits due to the xGT are quantified by calculating the percentage of Δv increment with respect to the classical GT as,

$$f_{merit} = 1 - \frac{\Delta v_{xGT}}{\Delta v_{GT}}, \tag{4.4}$$

where Δv_{xGT} and Δv_{GT} are the change in velocity imparted on the asteroid by the xGT and the GT, respectively. The relative increment in towing Δv due to the xGT hovering modes is shown in Fig. 4.3. The increased Δv is due to the decreased average distance the xGT spacecraft has from the center of mass of the asteroid. The results shown in Fig. 4.3 suggest that in the most optimistic scenario the xGT strategy could

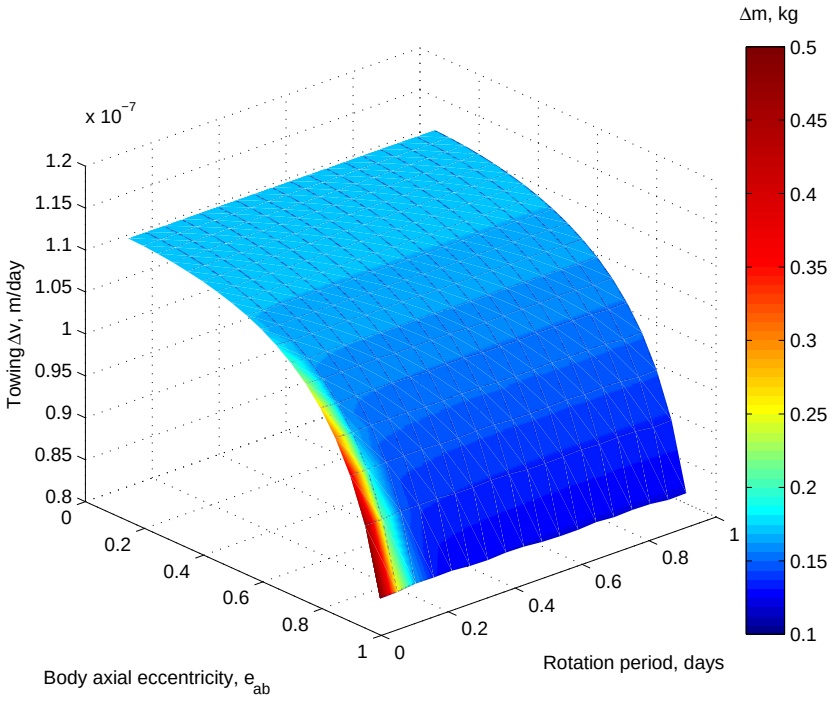

(a)

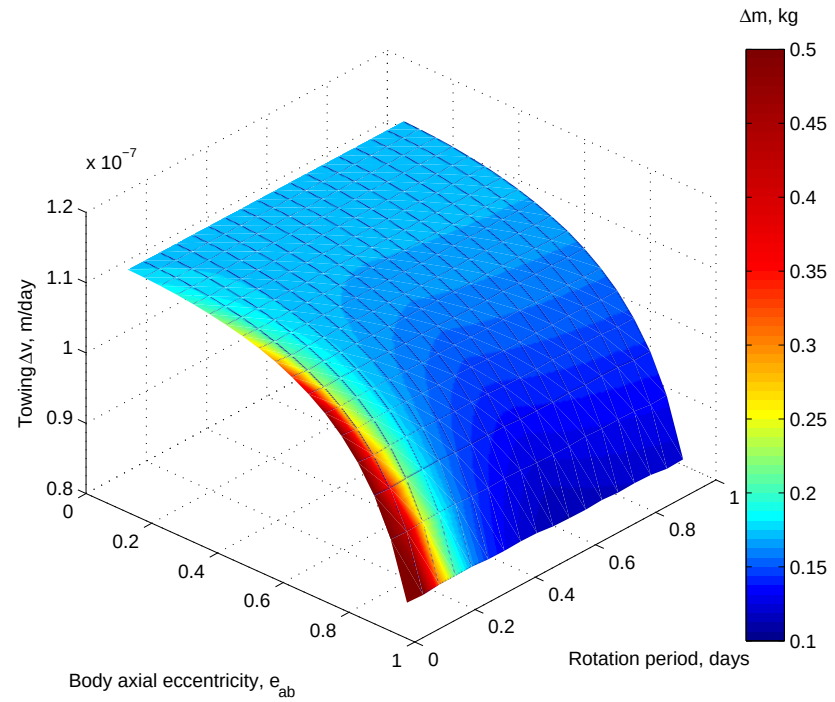

(b)

Figure 4.2: Towing Δv exerted by the (a) xGT1 and (b) xGT2.The color scale indicates the propellant mass used over a 24 hrs interval.

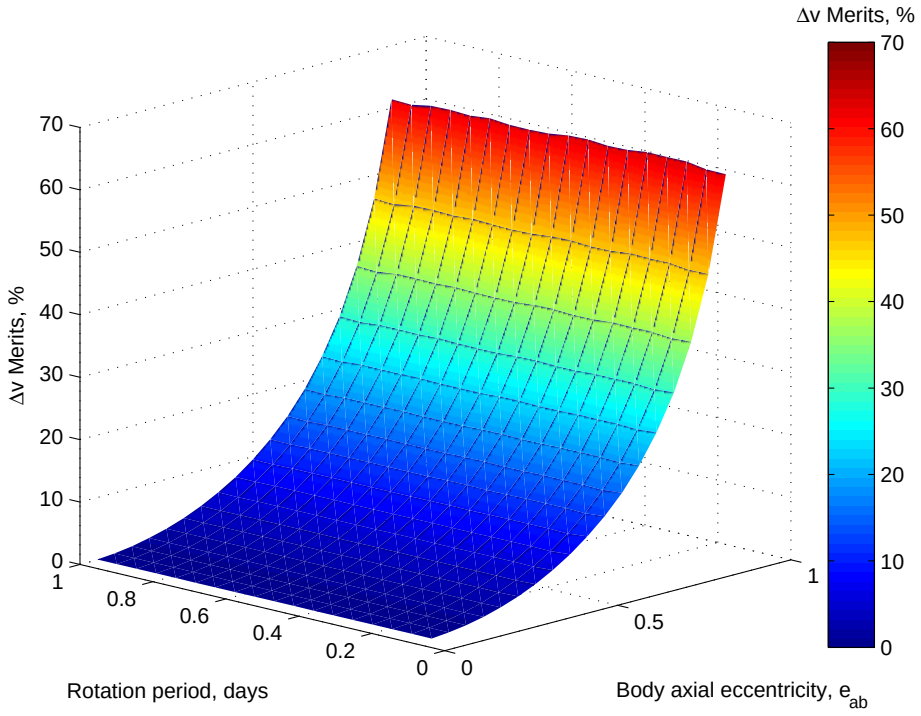

Figure 4.3: Towing merits for the xGT modes.

yield Δv improvements of up to a 60% with respect to the classical GT.

Even though both xGT strategies exhibit the same towing merits, their propellant penalties present large differences. Figure 4.4(a) maps the dependence of propellant consumption in the shape and rotation space of the NEO for the xGT1. From Fig. 4.4(a), it is easy to observe that shorter rotation periods and higher axial eccentricities induce a nonlinear increase in propellant usage. This increment in propellant demands is a direct consequence of the guidance law given in Eq. (2.6), where the xGT acceleration is proportional to the square of the asteroid rotational period and to the displacement amplitude, defined by the difference between the semiaxes a and b. In contrast, the xGT2 (Fig. 4.4(b)) shows a higher increase in propellant usage towards the limit of high axial eccentricities and short rotation rates. The increased propellant rate is a direct consequence of the combined action of the thrusters in the $\hat{\mathbf{i}}$ and $\hat{\mathbf{j}}$ coordinates as dictated by the guidance law of Eq. (2.18).

The propellant penalties are the loss in efficiency of the xGT relative to the clas-

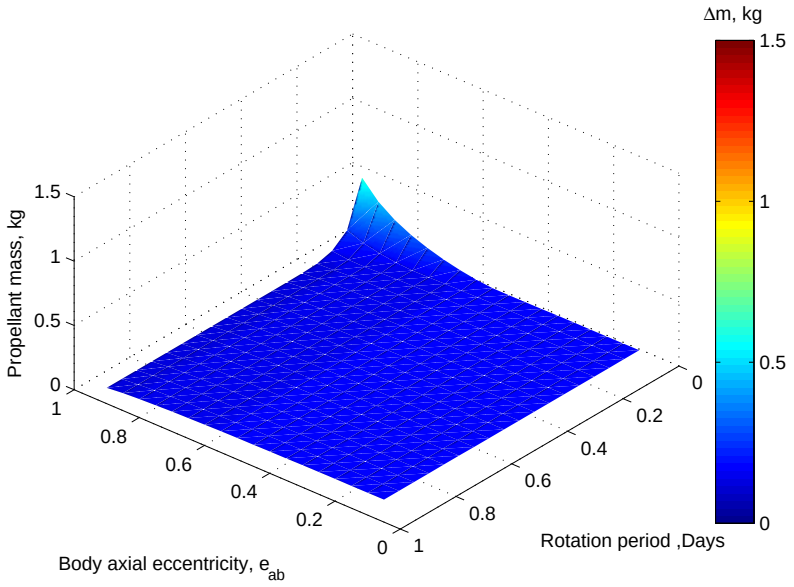

(a)

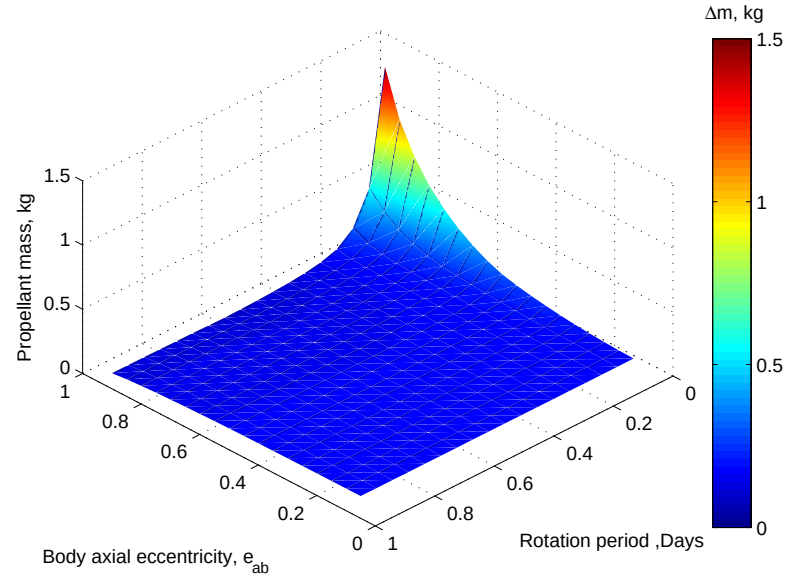

(b)

Figure 4.4: Map of the averaged propellant mass rate consumed by the (a) xGT1 and (b) xGT2.

sical GT. We meassure these penalties as the relative percent of increased propellant demands of the xGT hovering modes with respect to the inertial hovering,

$$f_{penalty} = 1 - \frac{\Delta m_{xGT}}{\Delta m_{GT}}, \tag{4.5}$$

where Δm_{GT} is the fuel mass depleted by the classical GT and Δm_{xGT} is the fuel mass depleted that corresponds to the dynamic hovering modes.

Figure 4.5 shows the relative increase in propellant usage due to the dynamic hovering modes. Figure 4.5(a) displays the penalty for the xGT1 strategy. For the xGT1, the penalties increase monotonically along the axial eccentricity space reaching up to 85%. Along the rotation space a sharp increase in propellant consumption appears near the limit of high eccentricities and rotation periods shorter than 8 hours. Figure 4.5(a) shows the penalty map for the xGT2. In this mode the penalty map is richer in features than the former (Fig. 4.5(b)). The penalties near the limit of high eccentricities appear to be less than those in the xGT1. There is also a penalty decrease at rotation periods near 0.6 day ($\approx$ 14 hours) followed by a spike in penalties towards the limit of high eccentericities and short rotation period.

In general, these penalties are driven by three factors. First, as the spacecraft moves closer to the asteroid its engines need to increase their thrust to balance the local gravity field. Second, the cosine losses due to the canting of thrusters T_1 and T_2 increase as the xGT moves closer to the asteroid surface. The third contributor is the synchronized periodic motion of the xGT. The second term in Eqs. (2.6) and (2.18) is proportional to the displacement amplitude and to the square of the asteroid rotation rate. Its effects are evident towards the limit where the asteroids have extreme eccentric shapes and short rotation periods.

The remarked differences seen between Figs. 4.5(a) and 4.5(b) motivates to compare these results against each other. We perform this comparison by subtracting the

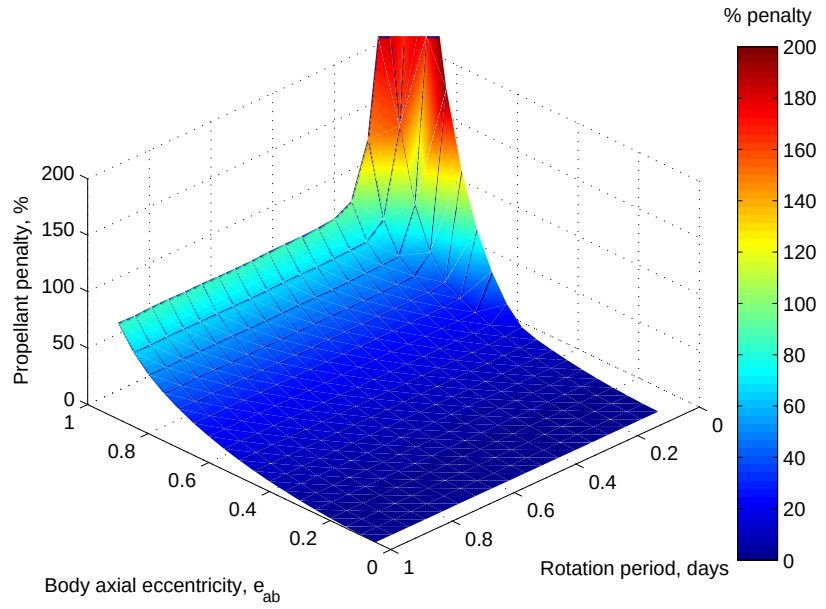

(a)

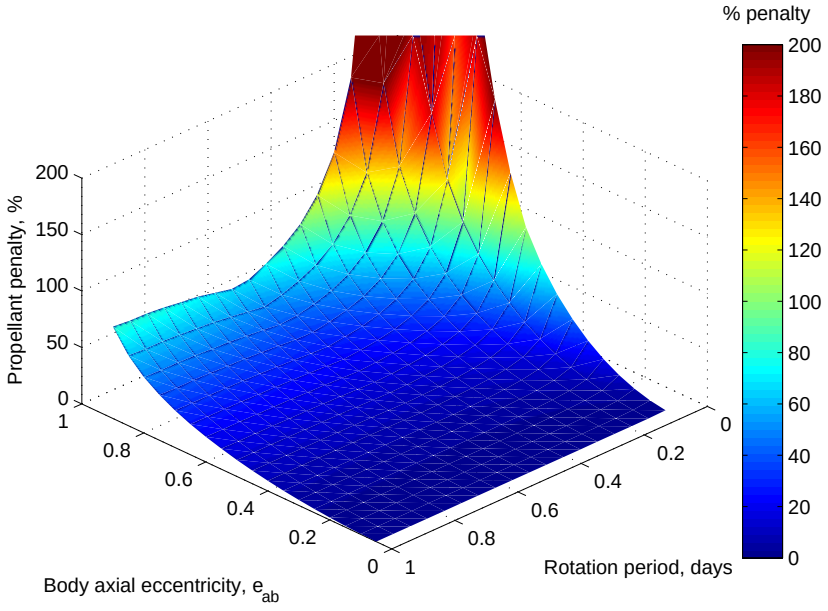

(b)

Figure 4.5: Propellant penalties incurred by xGT modes:(a) xGT1 and (b) xGT2.

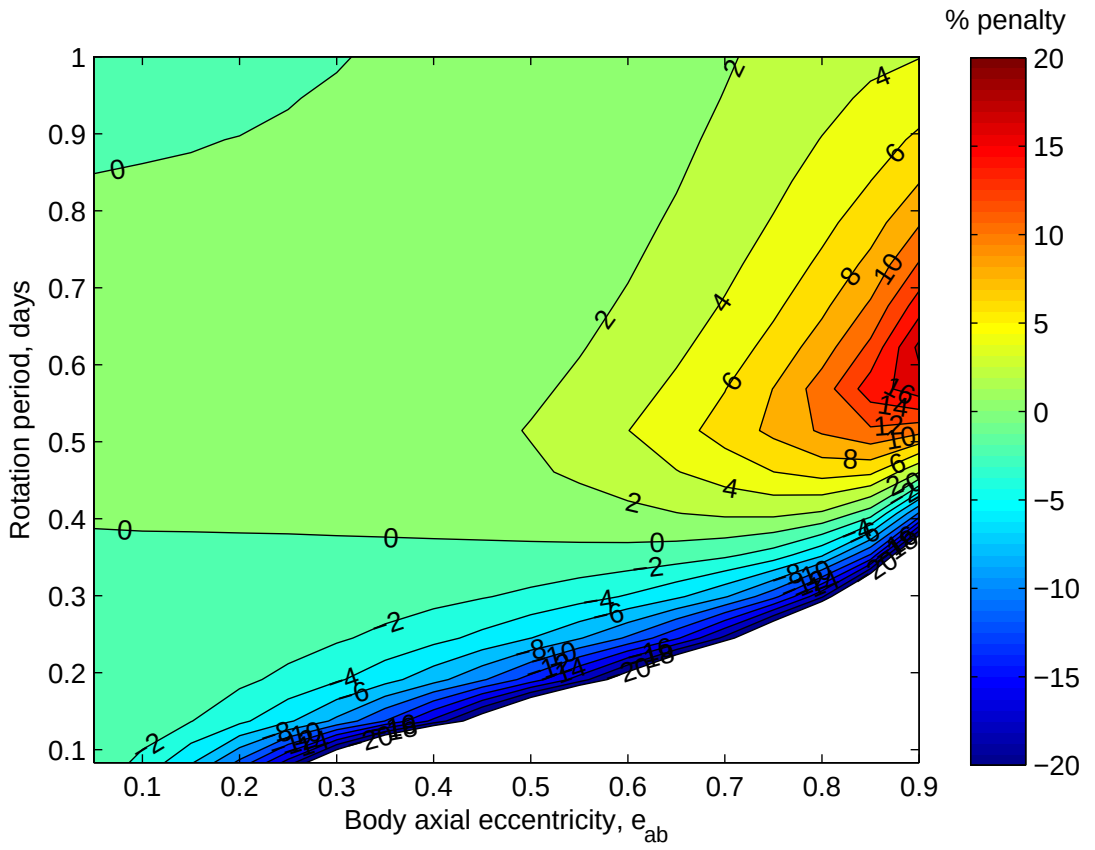

Figure 4.6: Penalty difference between xGT1 and xGT2.

values in Fig. 4.5(a) from those in Figs. 4.5(b). In this way we can get an insight on which strategy is more efficient given an asteroid with certain axial shape and rotation period. The results are presented in Fig 4.6 where positive values indicate the xGT2 carries less penalties than the xGT1, and negative values indicate that penalties are relatively less for the xGT1 than for the xGT2. Note that the xGT2 perform with up to a 20% less propellant penalty in a region at $e_{ab} = 0.9$ and $T \approx 14$ hours while the xGT1 incurs less penalties near the edge of the clear region. The clear region near the limit of short rotation periods is close to the gap where the implementation of the classical GT is more convenient than the advanced hovering strategies. That is, the penalties are too high with respect to the merits.

As an illustrative example we consider a 1-ton xGT system loaded with 50 kg of Xe propellant. We were interested in comparing its deflection Δv capability against

the classical GT. For this we assumed asteroids of different shapes with rotation period of 12 hours. The mass and density of the asteroids are indicated in Table 4.1. A simulation was performed until the xGT depleted its propellant and a similar simulation was performed for the classical GT. The results are shown in Figure 4.7(a). As expected, the xGT was able to exert a higher Δv on the asteroid than the classical GT during the same time interval. This effect is amplified when the target asteroid possesses high axial eccentricities. A contrasting point lies over the fact that substantial amounts of propellant remained in the tanks of the GT at the end of the towing period. Figure 4.7(b) shows the residual propellant mass against the simulation time. These results suggest that for certain deflection scenarios we could reduce towing time for certain Δv goal by employing the xGT concept.

4.3.1 Engine Canting Angle

The variation of the canting angle of engines T_1 and T_2 worth to be explored to determine whether the implementation of a gimbaled system is realistic for the scenarios described above. The variation of the canting angle over a GT hovering cycle is a function of the asteroid shape and orientation, as well as the spacecraft position. The variation amplitude for each hovering mode is shown in Fig. 4.8. Figure 4.8 shows that the amplitude variation of the engine canting angle does not present a critical issue. For axial eccentricities lower than 0.6 the amplitude of the canting angle does not exceeds 5 degrees. Within this range the canting angle of the xGT is lower than the GT for $e_{ab} < 0.6$. For $e_{ab} > 0.6$ the GT displays a maximum amplitude of 6.5 degrees, the xGT1 reaches a maximum amplitude of 10 degrees and the xGT2 reaches 13 degrees. This analysis aids in the determination whether the complexity of a gimbaled system for the thrusters and the subsystems related to continuously track and adjust their orientation, overcomes the cost associated with the increased cosine losses incurred due to a fixed canting angle. A first look to these results leads

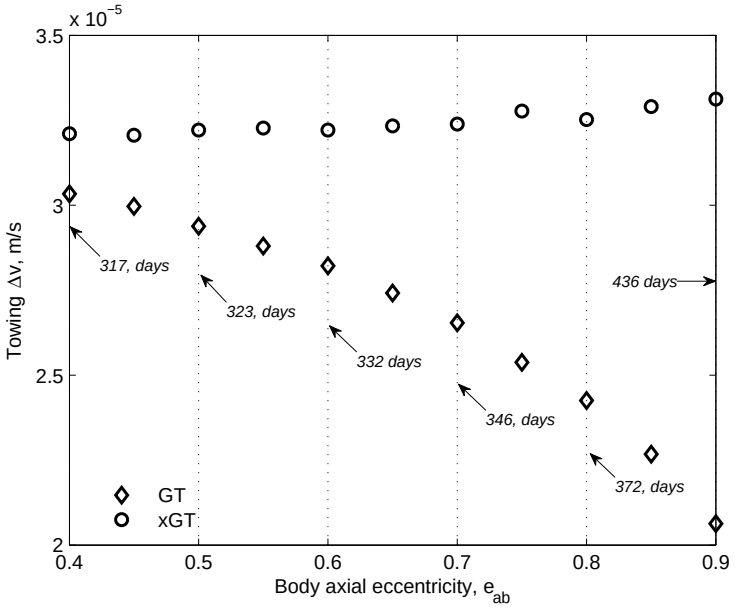

(a)

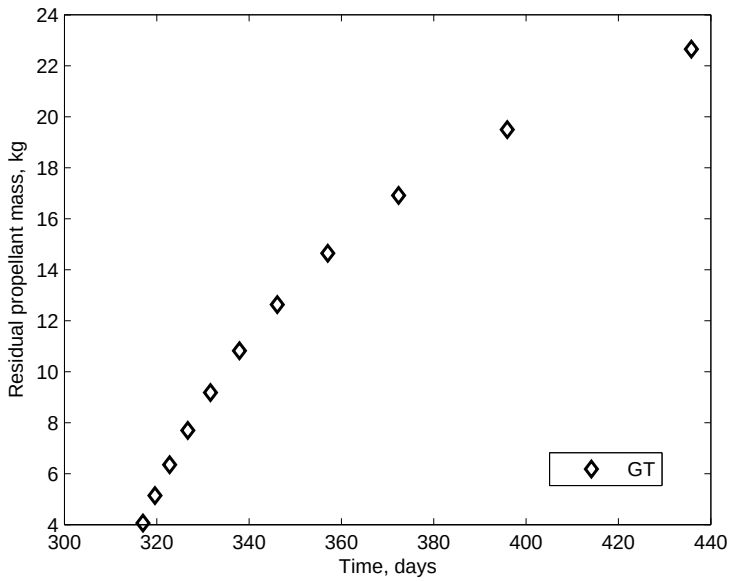

(b)

Figure 4.7: (a)Towing Δ achieved by the xGT upon propellant depletion. (b) Propellant mass remaining in the GT.

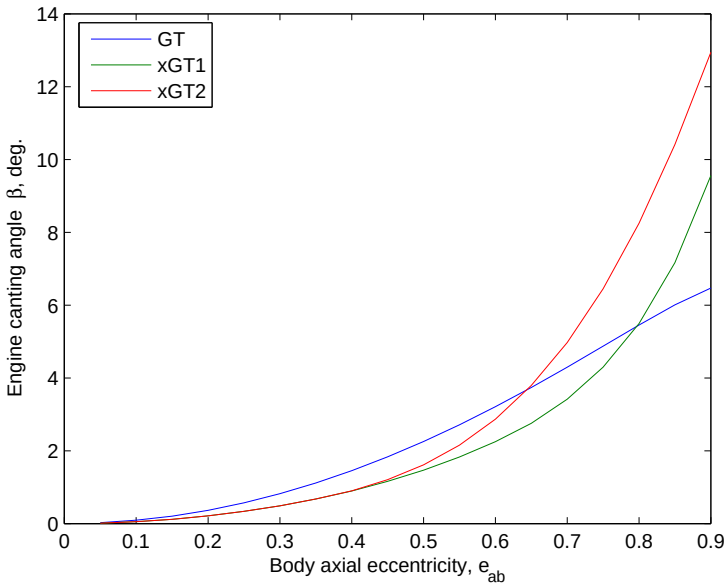

Figure 4.8: Amplitude of the engine canting angle.

to the speculation that for $e_{ab} < 0.6$ a continuous adjustment of the engine canting angle may not be a critical issue for any of the three hovering strategies. However, a detailed system analysis of cost and risks is required to provide with a precise answer.

4.4 NSTAR Ion Engine

In this section we report on the performance of the GT and xGT using the NSTAR engine model introduced section 3.3.2. The inclusion of a realistic thruster model implies that the available thrust T is limited and bounded within certain operational range $T_{min} \leq T \leq T_{max}$. From Table 3.1 these limits are: $T_{min} = 0.020$ N and $T_{max} = 0.092$ N. In addition, the specific impulse is variable and bounded between 1979 sec and 3127 sec. Using this information, it is convenient to perform some analysis using a simple model in order to obtain an insight about the general implications this thruster model could have on the GT systems. For this, we assume a GT hovering over a small spherical body and observe the effects on the thrusters operation as the

radial distance is increased. From Eq. (2.2) the thrust to support inertial hovering is given by

$$T = \frac{\mu m}{2d^2 \cos\beta}, \tag{4.6}$$

where d is the hovering distance. From the data listed in Table 4.1 the radius of the small asteroid is about 140 m. Hovering at an initial altitude $h = 80$ m results in $d = 220$ m. The thrust supplied by the canted engines is $T \approx 0.023$ N, just above T_{min} and satisfying the condition given in Eq. (3.21). Once the hovering distance is increased to the value where the required thrust T falls bellow T_{min}, Eq. (3.21) is be enforced by satisfying Eqs. (3.22) and (3.23); resulting in the firing of an opposite thruster (T_3) in order to balance the excess thrust from by T_1 and T_2.

The action of the engines to support hovering over a range of distances is shown in Fig. 4.9(a) and the resulting propellant mass rate is plotted in Fig. 4.9(b). The thrust supplied by each canted engine T_1 and T_2 is indicated by the solid line. The dashed line shows the operation of thruster T_3. Thruster T_3 provides thrust in the direction of the gravitational pull. The local gravitational force is indicated by the dash-dotted line. The thrust supplied by thrusters T_1 and T_3 is reduced as the distance from the body increases. At about $d = 230$ m, the required thrust from T_1 and T_2 falls below T_{min} causing T_3 to activate. Beyond $d > 230$ m, all three thrusters are operating. Another interesting event occurs at $d \approx 325$ meters where T_3 operates at a higher throttle level than T_2 and T_3. However, the resulting acceleration balances the local gravity pull.

Figure 4.10 shows the averaged propellant mass depleted after one day by the GT operating in inertial hovering as a function of the asteroid axial eccentricity and rotation period. For the classical GT, the propellant rate depends only on the axial eccentricity of the asteroid and is independent from its rotation rate. The propellant depletion rate decreases from 0.38 kg/day on the region of a near spherical body ($e_{ab} = 0.05$), to about 0.36 kg/day near axial eccentricities of $e_{ab} = 0.6$. This is a result

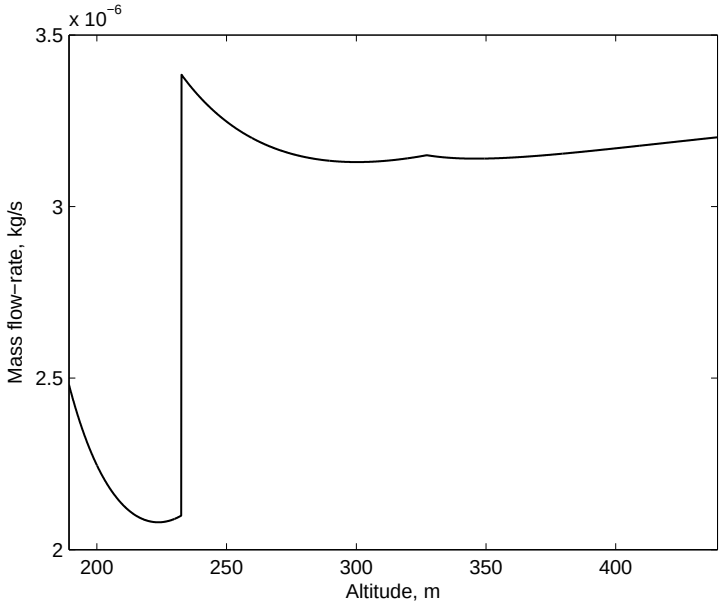

(a)

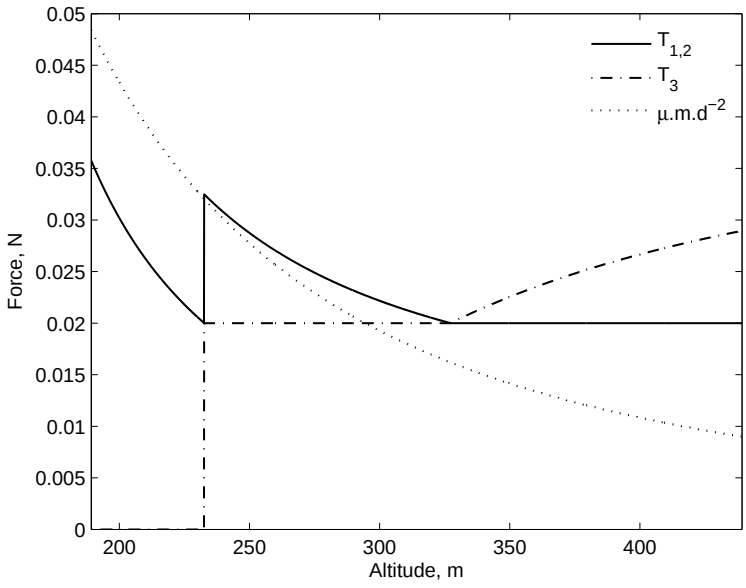

(b)

Figure 4.9: Engines mixing logic: (a) applied thrust and (b) net propellant depletion rate.

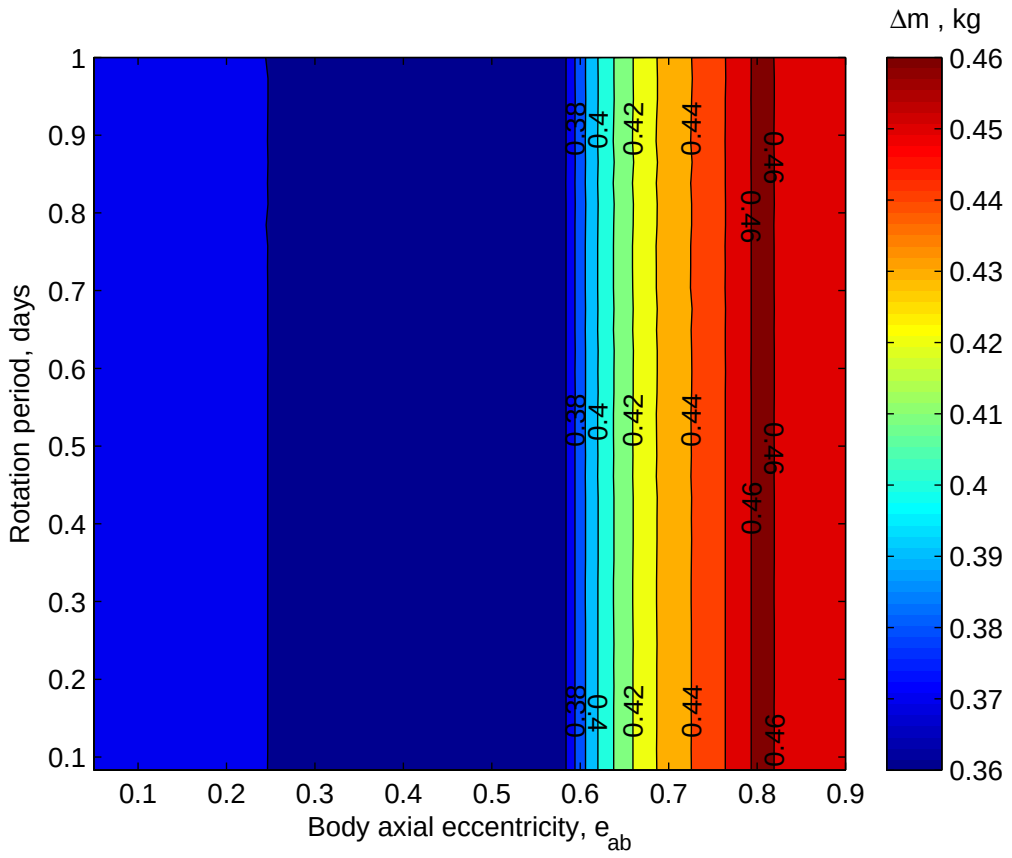

Figure 4.10: Propellant mass rate for the GT system powered by five NSTAR thrusters.

of the attenuation of the asteroid's gravitational pull as the GT hovers farther from the center of gravitational attraction. Beyond this point, the daily propellant mass rate displays a sharp increase reaching a peak value of 0.46 kg/day at $e_{ab} \approx 0.8$ followed by a shallow decrement. This behavior can be explained using the analysis performed at the beginning of this section. In short, the gravitational pull of the asteroid on the spacecraft had decreased to a value bellow the lower thrust boundary of the engine. The difference here is that that a different gravity field was used and we are adding into account the action of the engines along the $\hat{\mathbf{j}}$ axis. In consequence, engines in the opposite direction fire to compensate for the excess thrust. The gravitational pull is then balanced by the difference between the thrust components acting in opposite directions.

Figures 4.11 and 4.12 show the averaged propellant consumption rate for the xGT1 and xGT2, respectively. As could be expected from the results discussed in the previous section, the dynamic hovering modes display a strong dependence on the rotation rate of the asteroid but the overall propellant rate had increased. Figure 4.11 shows a shallow decrease in propellant usage as the axial eccentricity increases to about $e_{ab} = 0.7$ and rotation periods longer than 7 hours. For values of $e_{ab} > 0.7$ the propellant rate suddenly increases as the required thrust falls below the lower boundary of the thruster operational limits. Consequently, a complementary thrust is applied in the opposite direction, driving the thrusters to fire within its operational margins. Recall that in this hovering mode the gravitational pull decrease as e_{ab} increases but at the same time the displacement amplitude increases reducing the margin in which the required thrust in the $\hat{\mathbf{i}}$ direction falls below the operational limit of the engine.

If we move in the direction of shorter rotational periods, we find the well of minimum propellant consumption vanishes as periods become shorter than 7 hours and the mass rate increases faster in the direction of increased axial eccentricities and short rotational periods. This behavior can be explained as a consequence of the dominance of the second right-hand term in Eq. (2.6) over the asteroid's gravitational pull. Equation (2.6) indicates the acceleration of the xGT is proportional to the displacement amplitude and to the square of the asteroid rotation rate. The void region in the lower corner of Fig. 4.11 indicates that the required thrust exceeded the operational limit of the thruster (0.092 N). Evidently, the xGT1 cannot operate under these conditions.

Figure 4.12 shows the propellant consumption rate for the xGT2. The features found here share a close similarity to those found earlier in Fig. 4.11. However, a prominent feature arises near the lower right corner of the map. A "valley" of relatively minimum mass rate is isolating the void region from the region of increased

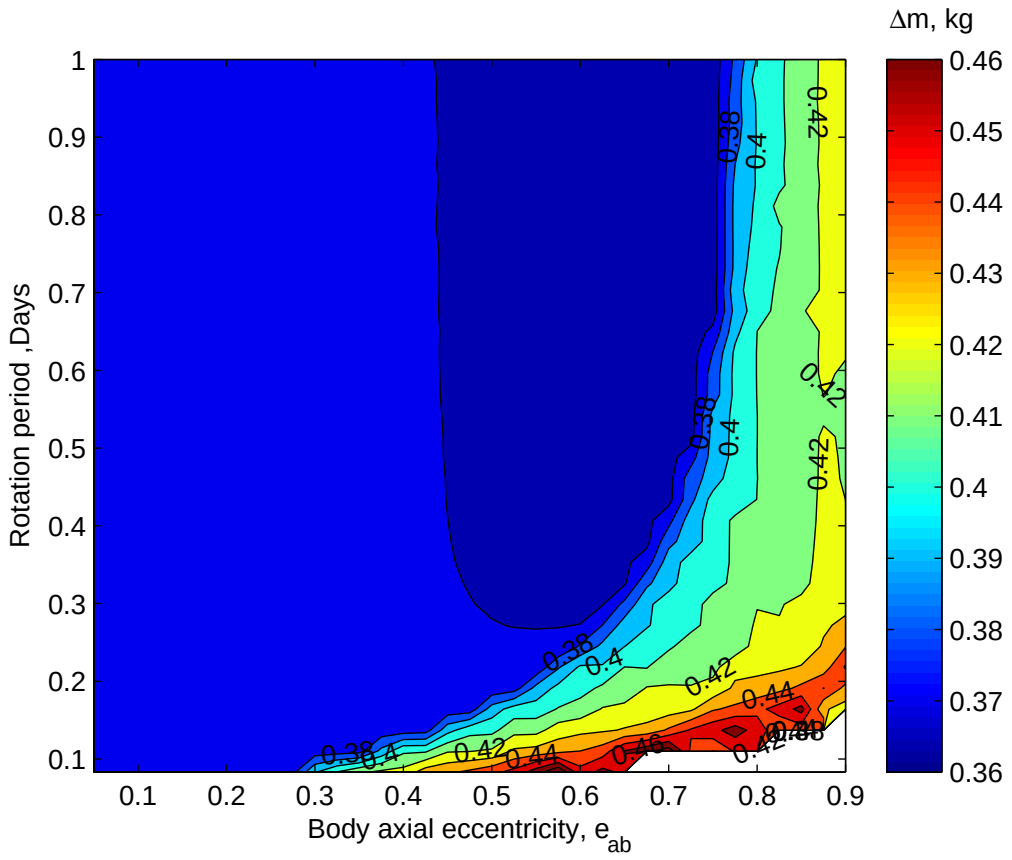

Figure 4.11: Propellant mass rate for the xGT1 system powered by five NSTAR thrusters.

mass rate. This valley suggest that the required thrust does not falls below the minimum threshold and also the thrusters are operating in the thrust region where I_{sp} is highest.

Figure 4.13 maps the propellant penalties between the GT and the xGT1. Positive values indicate the classical GT is favored in terms of propellant usage while negative penalties favor the implementation of xGT1. These results show that penalties are negligible in most of the space where $e_{ab} < 0.6$, except for a small isolated region where $T < 0.2$ days (< 5 hours) and $e_{ab} = 0.6$. In this region the penalties due to the xGT1 increase to near 30% over the GT. Once the axial eccentricity becomes greater than 0.6 the penalties display negative values favoring the implementation of the xGT1 with up to 20% less fuel consumption than the classical GT. The explanation lays in

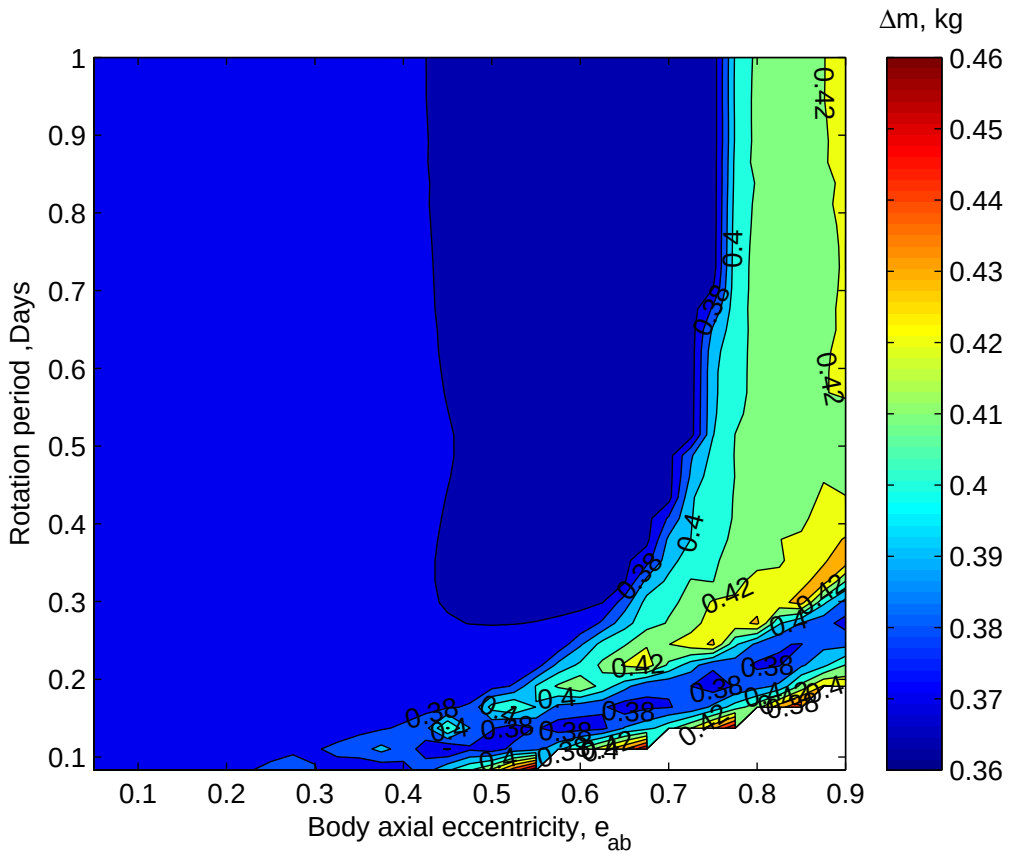

Figure 4.12: Propellant mass rate for the xGT2 system powered by five NSTAR thrusters.

the fact that the periodic translational motion of the xGT1 increase the level of thrust needed, consequently decreasing the time where differential thrust balance needs to be applied. The improvements in propellant efficiency of the xGT1 over the GT are near 20% in a region where $e_{ab} \approx 0.7$ and $T > 0.5$ days. These results have serious implications in the previous assumption that the performance of a gravity tractor can be modeled using a variable-thrust engine with constant I_{sp} and a minimum thrust level $T_{min} = 0$ N.

Figure 4.14 maps the propellant penalties between the GT and the xGT2. As previously done, positive values indicate the classical GT is favored in terms of propellant usage while negative penalties favor the implementation of xGT2. The results presented in Fig. 4.14 show that for most of the region where $e_{ab} < 0.6$ no signifi-

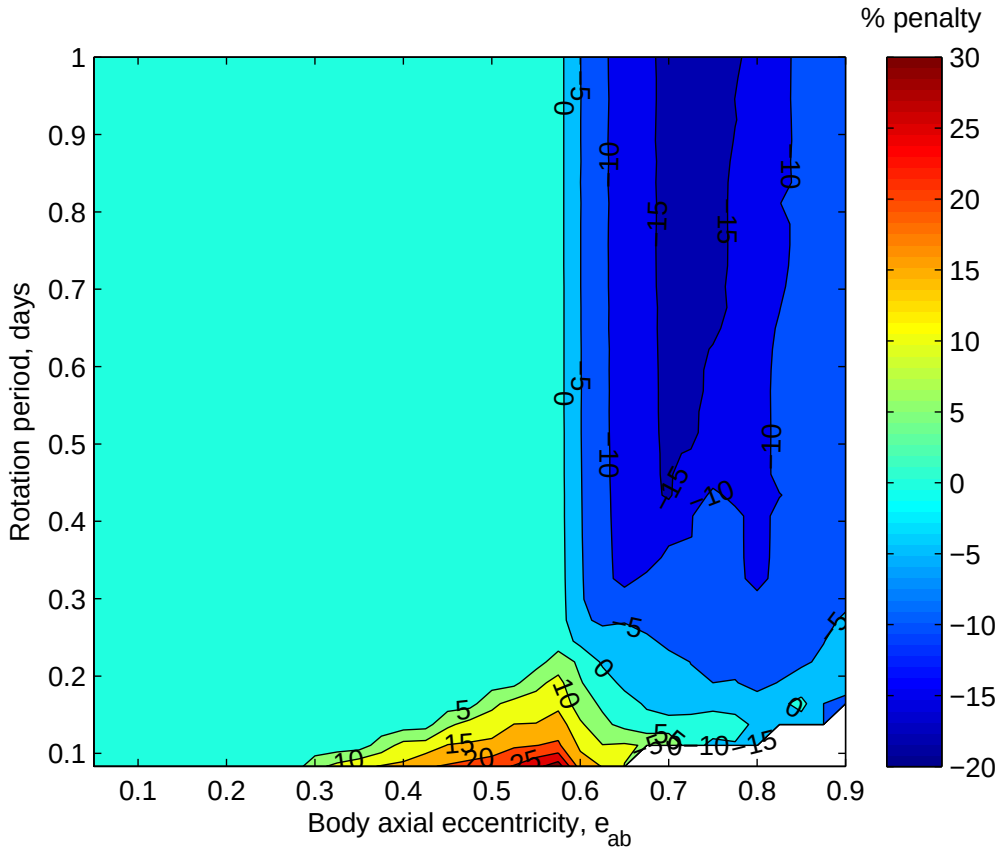

Figure 4.13: Percent penalty between the classical GT and the xGT1.

cant differences in propellant performance between the GT and the xGT2 exist. The region where $e_{ab} > 0.6$ and $P > 0.3$ displays a similar behavior to that observed in Fig. 4.13. When the rotational period falls below 0.3 day, the valley described in Fig. 4.11 translates into improved propellant efficiencies favoring the xGT2 over the classical GT.

The results presented above indicate that a realistic engine model changes completely the performance of a GT strategy, and under certain scenarios, the novel hovering strategies proposed in this investigation (xGT1 and xGT2) appear to be more efficient than the classical GT. Furthermore, we have observed that there are marked differences in the propellant performance between the xGT1 and xGT2. These differences motivate a comparison between the two strategies by subtracting the results

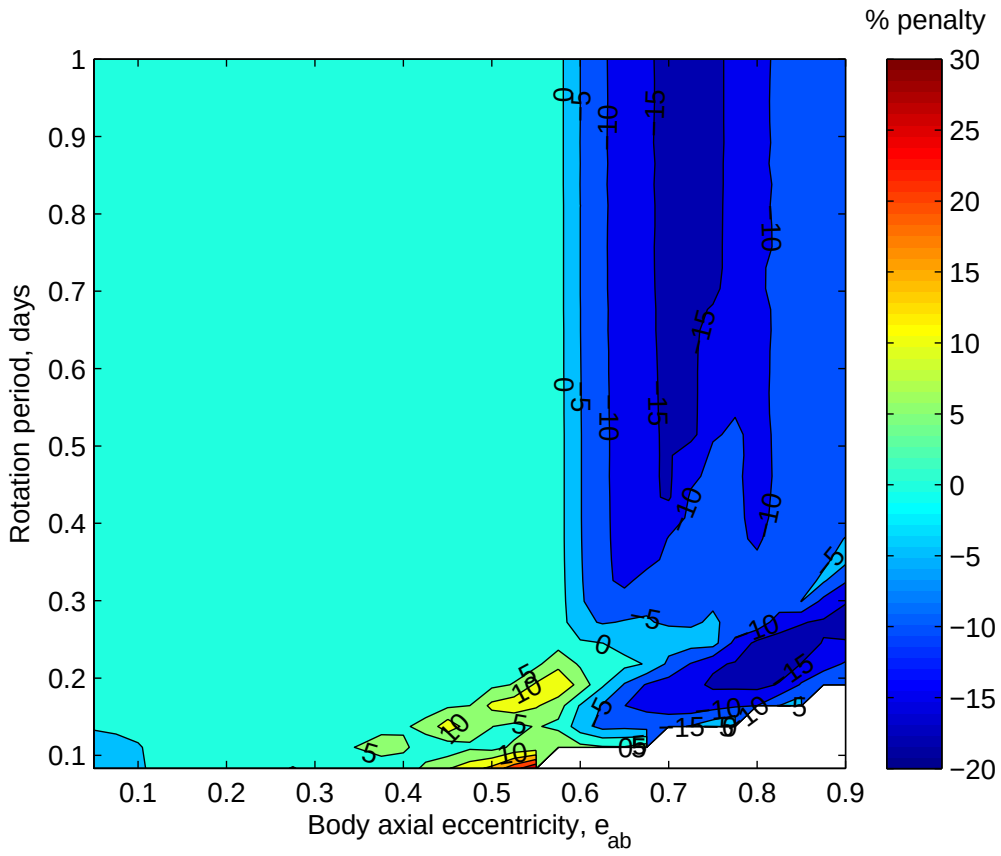

Figure 4.14: Percent penalty between the classical GT and the xGT2.

presented in Figs. 4.13 and 4.14. The results of this experiment are given in Fig. 4.15. Positive values favor the performance of the xGT2 while negative values favor the xGT1. The results in Fig. 4.15 show that differences in performance between the xGT1 and xGT2 are not greater than 4% in favor of the xGT1. An exception occurs within the area of the valley observed earlier in Fig. 4.12. The valley region suggests that the xGT2 yields about 10% improvements in propellant efficiency than the xGT1.

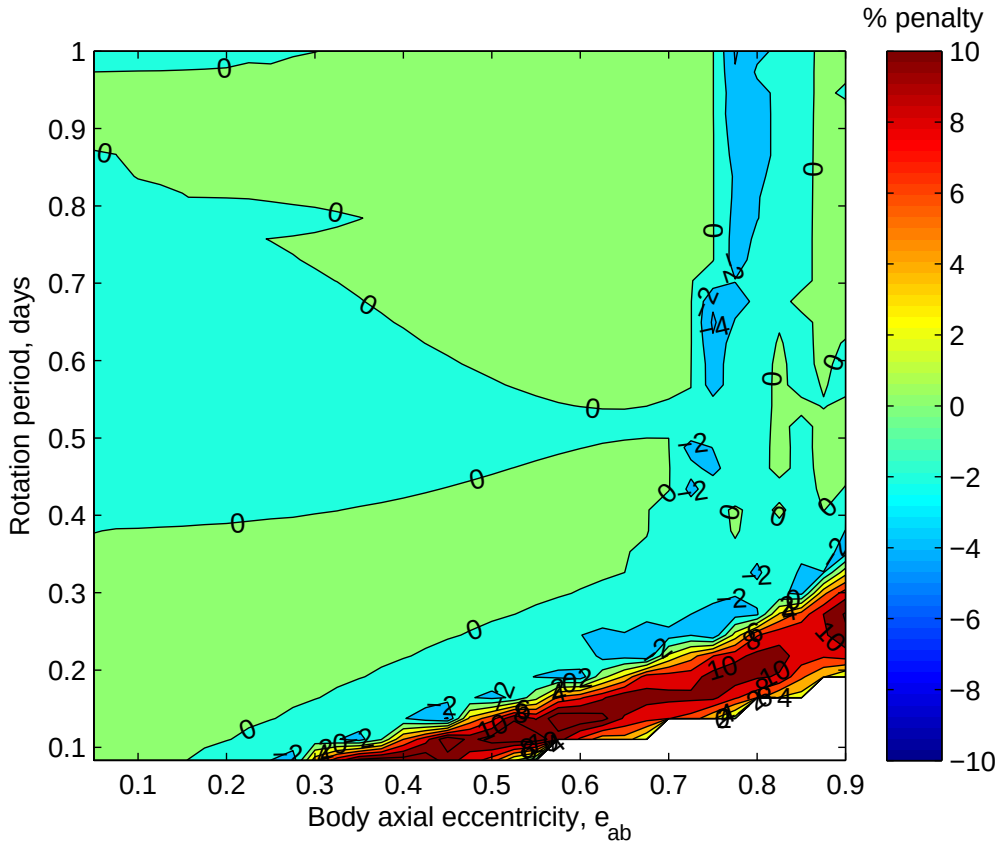

Figure 4.15: Percent penalty between the xGT1 and the xGT2.

4.5 Summary

In this chapter we performed a first-order analysis to determine the effectiveness of the proposed hovering strategies and compared them against the classical GT. The effectiveness was measured in terms of Δv imparted on the asteroid and the propellant penalties incurred by operating in the xGT modes. The analysis consisted a variety of body shapes and rotation rates. A second part of this chapter was dedicated to find the implications that a realistic engine model could have on the performance of the GT and xGT systems. The results found show the importance to consider certain level of detail, in particular, the operational range of the engines. Such consideration revealed that in some scenarios the xGT could perform more efficiently than the classical GT by reducing the propellant penalties.

Chapter 5

Hovering Control for the Extended Gravity Tractor

5.1 Introduction

This chapter presents results on the implementation of set of basic strategies to control the GT hovering modes. The control strategies considered are a dead-band (DB) and proportional-derivative (PD) controllers. These control algorithms were implemented independently for each axis, allowing to select the most convenient controller for each coordinate.

5.2 Hovering Control

A typical controller is divided in two components, an open-loop and a closed-loop term. The open-loop controller (OL) is employed to cancel the gravitational pull of the asteroid. The closed-loop controller corrects for any trajectory deviations caused by external perturbations such as solar radiation pressure or plant inaccuracies. For each hovering strategy a different combination of DB and PD were used to control

the spacecraft motion on each axis. The way these controllers were implemented is described in the following subsections.

5.2.1 Inertial Hover

The simplest way to achieve inertial hovering is by means of a DB controller. The performance of this type of hovering control has been studied in the literature [40, 41, 42, 39] and successfully implemented in the Hyabusa mission commanded by the Japanese Aerospace Exploration Agency (JAXA) [43]. The DB controller can be implemented alone or in combination with an open-loop component depending on the desired performance level. In this work it is assumed that the local gravity field is balanced by the action of an open-loop controller,

$$\frac{T_{ol}}{m} = -\frac{\partial V}{\partial \mathbf{r}}\bigg|_{\mathbf{r}=\mathbf{r}_0}. \tag{5.1}$$

The closed-loop component is then analyzed in the phase plane of each coordinate. Figure 5.1 shows the general phase-plane logic of a DB controller. The structure of the controller consist of a coast ($\mathbf{u} = 0$) and a firing zone ($\pm 1\mathbf{u}$). The error and error rate boundaries (δr and $\delta \dot{r}$) drive the GT into a limit cycle in the phase plane inside the coast zone.

To determine the switching logic the described in Fig. 5.1 let,

$$C_0 = u\, r_n, \tag{5.2}$$

$$C_1 = u\,(r_n + \delta r)\,, \tag{5.3}$$

$$C_2 = u\,(r_n - \delta r)\,, \tag{5.4}$$

$$C = \frac{1}{2}\dot{r}\,|\dot{r}| + u\, r. \tag{5.5}$$

The phase plane logic is then written as:

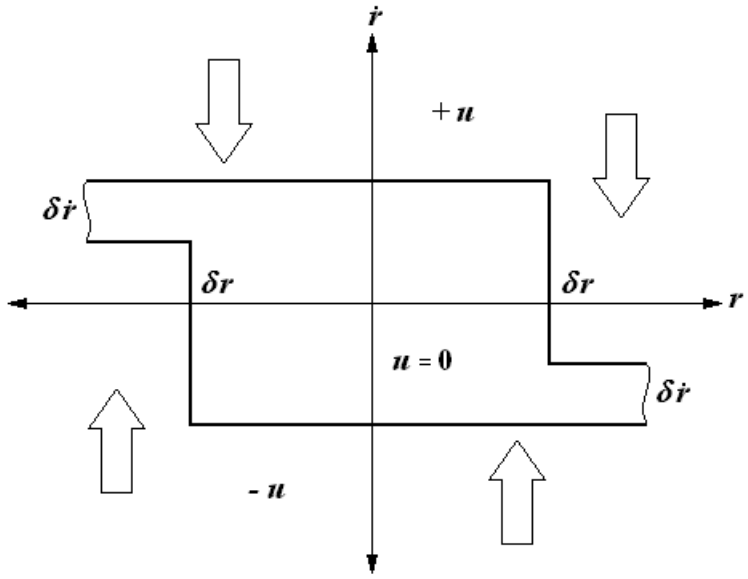

Figure 5.1: Phase plane logic diagramfor the DB controller.

if $C - C_0 < 0$ *then,*

$$u = \begin{cases} -T_c \operatorname{sgn}(C - C_0), & \text{if } C - C_2 < 0 \\ 0 & \text{otherwise} \end{cases} \tag{5.6}$$

else, if $C - C_0 > 0$ *then,*

$$u = \begin{cases} -T_c \operatorname{sgn}(C - C_0), & \text{if } C - C_1 > 0 \\ 0 & \text{otherwise} \end{cases} \tag{5.7}$$

else, $u = const.$

In practice, it is common to include certain percent of hysteresis in order to avoid jitter. The control of a spacecraft operating in inertial hovering was studied in the literature [44, 40, 41, 42, 39] therefore the remaining sections discuss the results regarding to the control of the dynamic hovering strategies.

5.2.2 Dynamic Hovering (xGT1 and xGT2)

For the dynamic hovering modes a PD controller is implemented to control the translational motion. The controller acts over the $\hat{\mathbf{i}}\hat{\mathbf{k}}$-plane in the xGT1 while the DB controller acts along the $\hat{\mathbf{j}}$-axis. In the xGT2 the DB controller along the $\hat{\mathbf{j}}$-axis was replaced by a PD controller, allowing control of the translational motion with greater accuracy.

The PD controller defined in Eq. (5.8) continuously tracks the position error (proportional term), and the rate at which the error is changing (derivative term). The proportional term, k_p provides a restoring force proportional to the error driving the system towards the reference point. At the same time, the derivative term k_d adds damping to prevent the system to oscillate about the operational state ($\mathbf{r}_{ref}$, $\dot{\mathbf{r}}_{ref}$).

$$\mathbf{u} = -k_p \left(\mathbf{r} - \mathbf{r}_{ref}\right) - k_d \left(\dot{\mathbf{r}} - \dot{\mathbf{r}}_{ref}\right). \tag{5.8}$$

The following results illustrates the behavior of the combined controllers for xGT1 and xGT2. The parameters used in the simulations are shown in Tables 5.1 and 5.2. The parameters used for the controllers are listed in Table 5.3.

Table 5.1: Asteroid Parameters.

Density, kg/m^3	Mass, kg	Axial dimensions, m	Rotaion periond, hs
2300	2.6×10^{10}	$215 \times 129 \times 97$	12

Table 5.2: Spacecraft Parameters.

h, m	$\mathbf{r}_0$, m	$\mathbf{r}_{ref}$, m	m_0, kg
80	[282, -5, 5]	[272,0,0]	1000

Table 5.3: Controller Parameters.

Method	Proportional gain, k_p	Derivative gain, k_d	δr, m
xGT1	5×10^{-6}, 0, 10^{-6}	3×10^{-2}, 0, 10^{-3}	10
xGT2	5×10^{-6}, 0, 10^{-6}	3×10^{-2}, 10^{-3}, 10^{-3}	NA

xGT1

To accurately drive the xGT1 the reference state were defined as,

$$\mathbf{r}_{ref} = \left[a + h - \frac{a-b}{2}(1 - \cos(2\omega t))\cos(\lambda), 0, 0\right]^T, \tag{5.9}$$

$$\dot{\mathbf{r}}_{ref} = \left[\omega(a-b)\sin(2\omega t)\cos(\lambda), 0, 0\right]^T. \tag{5.10}$$

The DB controller is implemented for a DB with a displacement tolerance of $\delta r = \pm 10$ meters from the nominal and 10% of hysteresis. Figure 5.2(a) plots the position of the xGT in inertial coordinates and the projected trajectory in the fixed frame of the asteroid is shown in Fig. 5.2(b). The initial response of the controller is plotted for the x and z position and velocity components in Figs. 5.3(a) and 5.3(e) with their respective phase plane trajectories. The PD controller gains were chosen to prevent overshoot in the x direction and to avoid exceeding the thruster limits. However, it is likely that these gains will have to be selected independently for each particular scenario. The small overshot along the z direction does not present any risk and could be tolerated in most scenarios. The dotted line marks the reference trajectory.

The DB controller is implemented along the y-coordinate. Figure 5.3(c) displays position and velocity history along the y-coordinate for the xGT1. The phase space plot is shown in Fig. 5.3(d) along with the switching boundaries and their hysteresis markers. The solid lines indicate the ideal DB boundary while the broken inner

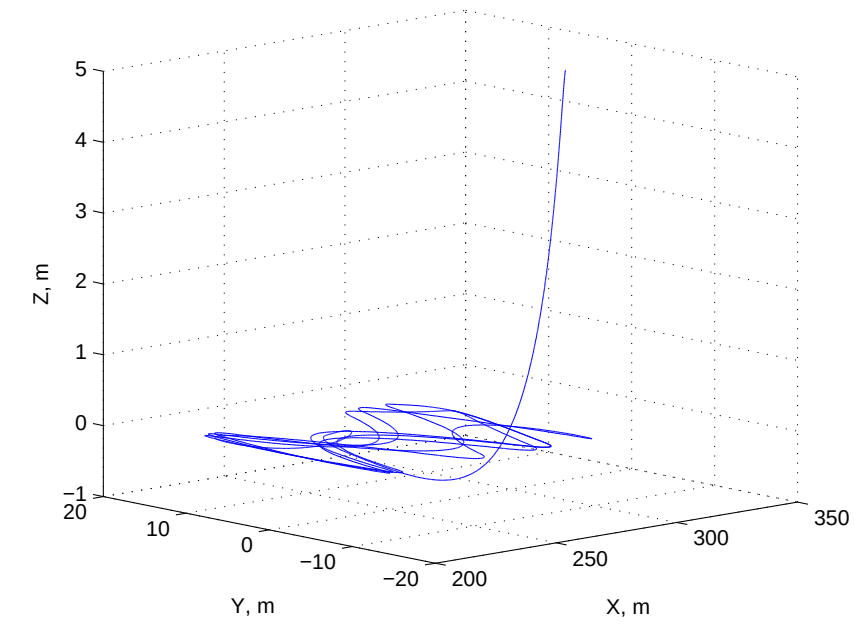

(a)

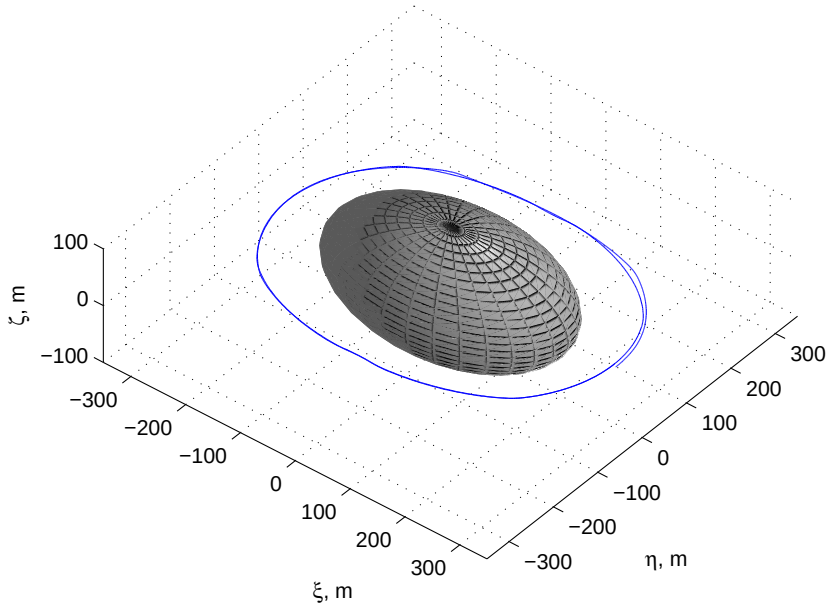

(b)

Figure 5.2: Trajectory plots for the xGT1, (a) $\hat{\mathbf{i}}\,\hat{\mathbf{j}}\,\hat{\mathbf{k}}$ coordinates, and (b) body frame.

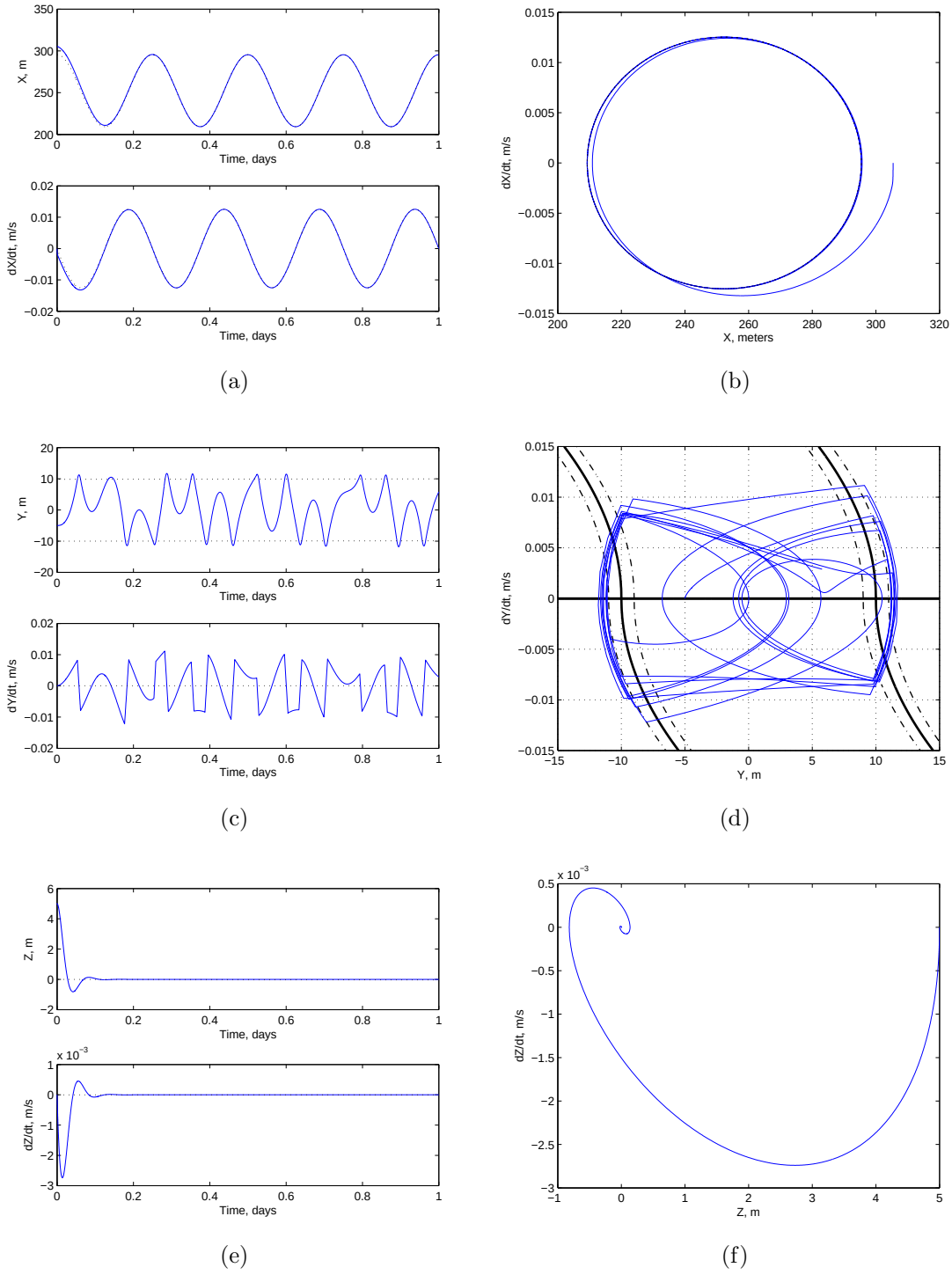

Figure 5.3: Response of the controllers for the xGT1: (a) and (b) show the state history and phase plane plots for the x axis; (c) and (d) for the y axis; (e) and (f) for the z axis.

lines indicate the switch-off boundary and the outer broken lines mark the switch-on boundaries. The chaotic nature of the trajectories is evident and the controller shows stability and good response. Due to the highly nonlinear and discontinuous nature of the DB controller, its trajectory is very sensitive to the tolerances of the integration algorithm. Therefore, when this controller is implemented the integration is usually longer.

xGT2

The reference state used to guide the xGT2 is,

$$\mathbf{r}_{ref} = \begin{pmatrix} a + h + \dfrac{a_p - b_p}{2}(-1 + \cos(2\omega t)\cos(\lambda) \\ (a_p - b_p)\sin(2\omega t)\cos(\lambda) \\ 0 \end{pmatrix}, \tag{5.11}$$

$$\dot{\mathbf{r}}_{ref} = \begin{pmatrix} -(a_p - b_p)\omega \sin(2\omega t)\cos(\lambda) \\ 2(a_p - b_p)\omega \cos(2\omega t)\cos(\lambda) \\ 0 \end{pmatrix}. \tag{5.12}$$

Figure 5.4(a) displays the trajectory of the xGT2 as seen from the $\hat{\mathbf{i}}\,\hat{\mathbf{j}}\,\hat{\mathbf{k}}$-frame. The projection in the fixed frame of the asteroid is shown in Fig. 5.4(b). The cyclic behavior about the $\hat{\mathbf{i}}\,\hat{\mathbf{j}}$-plane is projected as two circles with a fraction of them is merge together. As done previously with the xGT1, the initial position was offset from the nominal by 10 m in x, -5 m in y and 5 m in z. The PD controller was implemented in the three translational coordinates replacing the DB controller along $\hat{\mathbf{j}}$. The initial response of the controller is shown in Fig. 5.5 for each coordinate with their respective phase plane trajectory. The response of the controller is smooth with no signs overshoot in the x or y components. The response along the z axis has a

moderate overshoot. The proportional and derivative gains for each coordinate are given in Table 5.3. The gains were determined by trial and error with the objective to prevent saturation, overshoot and undershoot during the initial response.

The net propellant mass depleted by the xGT1 and xGT2 are shown in Figs. 5.6(a) and 5.6(b) respectively. The xGT1 consumed 0.3 kg of propellant while the xGT2 used 0.46 kg implying a 35% in propellant savings. The propellant rates are shown in Figs. 5.6(c) and 5.6(d) and the thruster firing histories are displayed in Figs. 5.6(e) and 5.6(f) for the xGT1 and xGT2, respectively.

These results can be compared with those presented in the previous chapter. The asteroid shape and rotation period are derived from Table 5.1, where the semiaxes dimensions correspond to an axial eccentricity $e_{ab} = 0.8$. From the results presented in Figs. 4.11, 4.12 and 4.15 it should be expected that both hovering strategies lead to the same propellant expenditures. However, the implementation of the DB controller along the xGT1 improves propellant efficiency by preventing the simultaneous firing of thrusters T_4 and T_5. Note that Figs. 5.6(e) and 5.6(f) show thrusters T_1, T_2 and T_3 operating simultaneously due to the fact that required thrust to guide the spacecraft is less than 0.020 N, but only the xGT2 has thrusters T_4 and T_5 firing simultaneously. The effects of the solar radiation pressure are also appreciated by looking at the thrust magnitudes of T_4 and T_5 in Fig. 5.6(f) where the amplitude of T_4 is always greater than the amplitude of T_5. This is because the solar radiation pressure applies force in the anti-solar direction and is balanced by T_4 which fire in the solar direction.

The improvements brought by the introduction of the DB controller in the xGT1 motivates to investigate its performance inside the valley region described in Fig. 4.12. Reducing the rotation period listed in Table 5.1 to 6 hours, gives the asteroid properties in the valley region of Fig. 4.12. Figure 5.7(a) indicates that the total propellant mass consumed by the xGT1 was 0.25 kg/day. The propellant rate for the xGT2

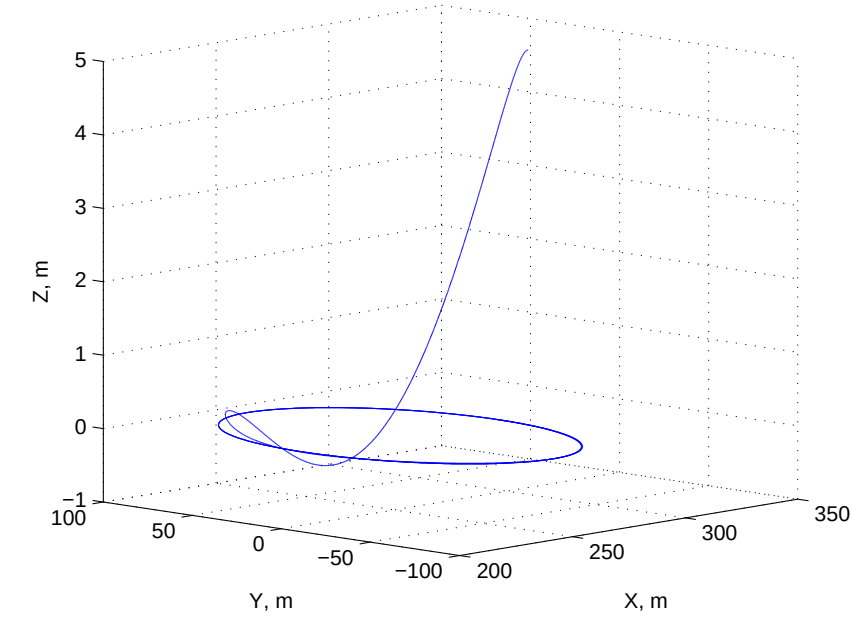

(a)

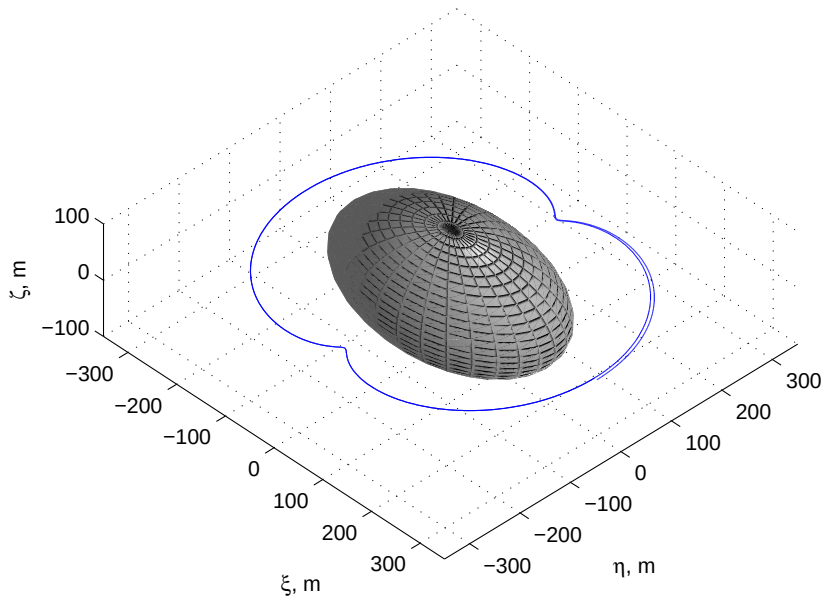

(b)

Figure 5.4: Trajectory plots for the xGT2, (a) $\hat{\mathbf{i}}\,\hat{\mathbf{j}}\,\hat{\mathbf{k}}$ coordinates, and (b) body frame.

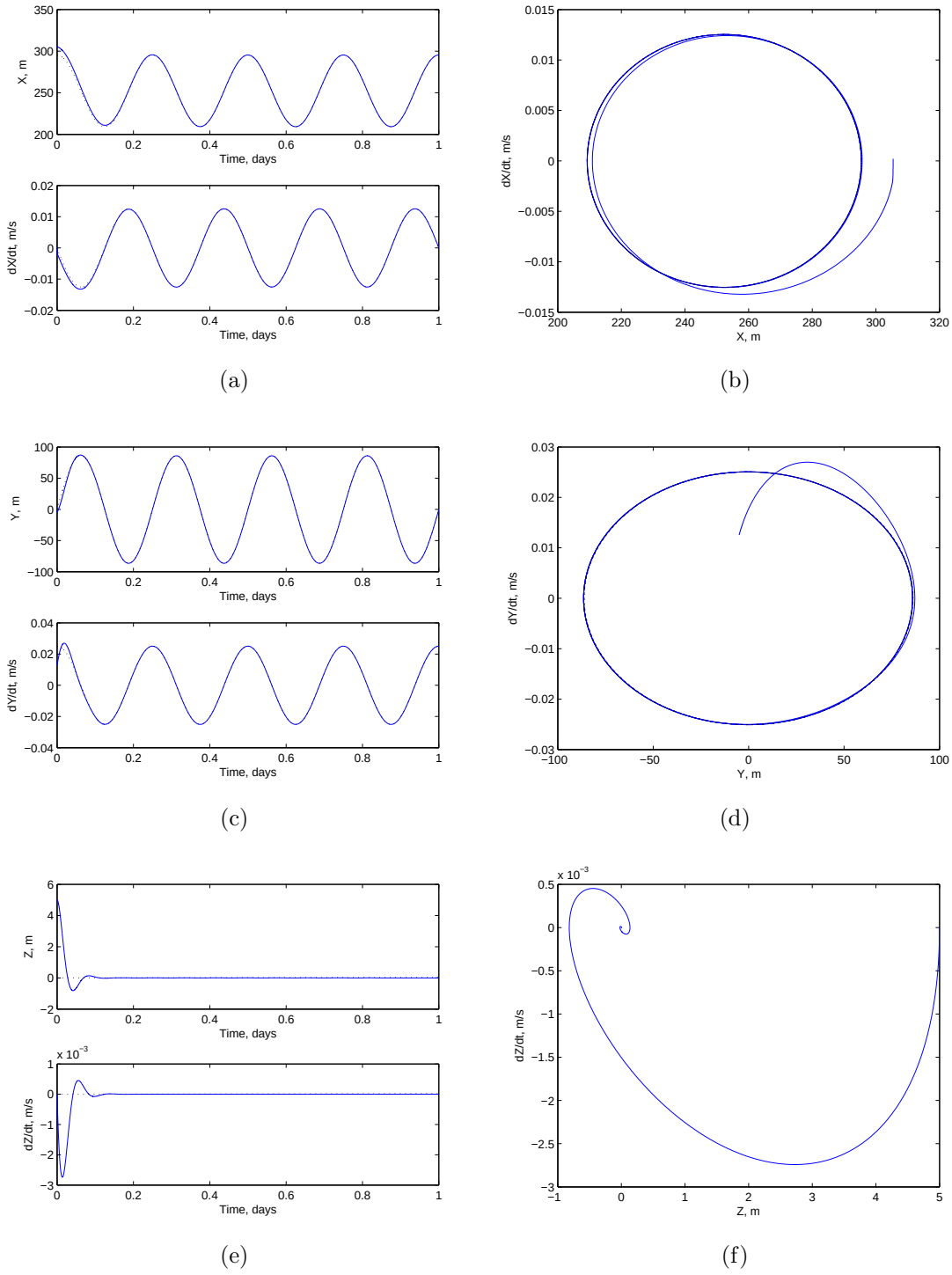

Figure 5.5: Response of the PD controller for the xGT2: (a) and (b) show the state history and phase plane plots for the x axis; (c) and (d) for the y axis; (e) and (f) for the z axis.

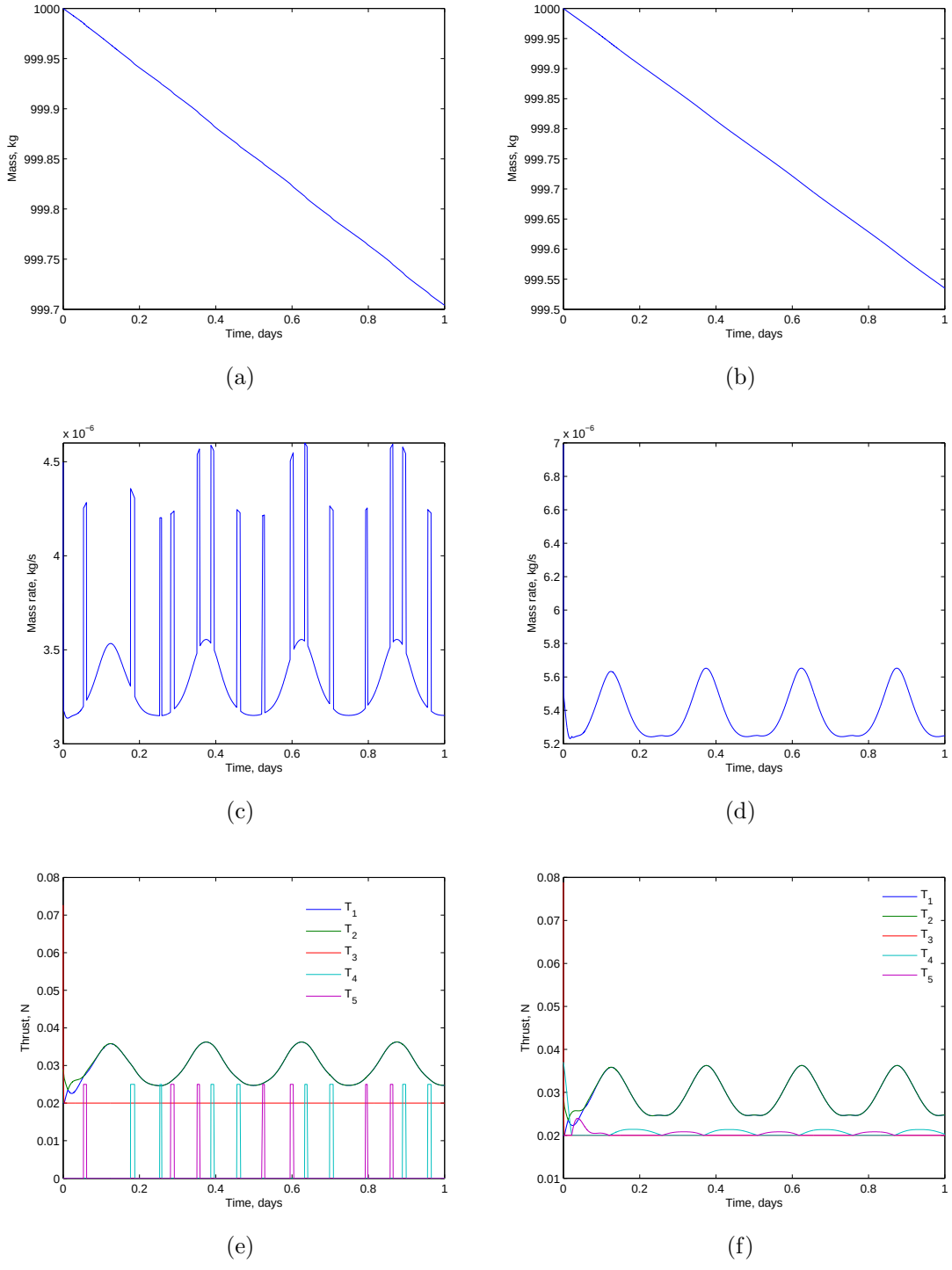

Figure 5.6: Propellant and thrust history plots for the xGT1 and xGT2: (a) and (b) show the propellant mass, (c) and (d) the propellant mass rate and, (e) and (f) show the engine throttle history.

(Fig 5.7(b)), was about 0.40 kg per day, in agreement with the findings shown in Fig. 4.12. These results imply that xGT1 used 38% less propellant than the xGT2. The DB controller showed to be able to improve the propellant efficiency by eliminating the implementation of the differential thrust balance along the y-axis. The firing sequence of the thrusters is illustrated in Figs. 5.8.

The firing sequence of thrusters T_1, T_2 and T_3 is shown in Fig. 5.8(a) for a period of 6 hours. The plot clearly illustrates the mixing logic of the thrusters T_1, T_2 and T_3. At $t = 0$ the GT spacecraft is at its farthest location from the center of the asteroid. At that time T_3 switches-on to accelerate the GT spacecraft towards the asteroid. Due to the low amount of thrust needed, T_1 and T_2 compensate for the excess thrust supplied by T_3. As soon as the demanded thrust changes signs, the action of the thrusters is reversed causing T_3 to compensate for the excessive thrust supplied by T_1 and T_2. Engine T_3 switches-off once the demanded thrust is within the operational boundaries of T_1 and T_2 ($t \approx 1$ hour). The peak of the smooth curve segment of T_1 and T_2 occurs once the spacecraft has reached halfway of its displacement path. The action of T_4 and T_5 is shown in Fig. 5.8(b). The action of the DB controller reduces the firing cycles needed to keep the the GT within the tolerances in the y-axis. Figure 5.8(c) plots the firing sequence of T_1, T_2 and T_3 for the xGT2 with features similar to those found for the xGT1 (Fig 5.8(a)). The firing histories for engines T_4 and T_5 are plotted in Fig 5.8(d). Contrary to the cases shown in Fig 5.8(b), these thrusters fire continuously increasing the propellant rates for the xGT2.

The performance of the controller configurations proposed for the xGT1 and xGT2 is tested over the entire space of body shapes and rotation rates as done in the previous chapter. Again the xGT1 implemented the combination of DB and PD controllers described earlier, and the xGT2 used PD controllers on each translational coordinate. The simulations were ran for 10 days and the results are presented as the daily average.

The parameters for the controllers are listed in Table 5.3. Figure 5.9(a) maps the daily average propellant mass by the xGT1. These results clearly indicate the improvements in propellant efficiency as a consequence of the introduction of the DB controller, over the entire spectrum of asteroid rotation rates and shape eccentricities. The void region in the lower right corner indicates that the required thrust exceeded the maximum available engine thrust $T_{max} = 0.092$ N. The introduction of the PD controller in the did not change the results in significant way for the xGT2. The qualitative differences between the results presented in Fig. 5.9(b) and those exposed in the previous chapter (i.e., Fig. 4.12) are a consequence of the coarser grid size used in the simulation (i.e., 18×18 compared to a 36×36 in the previous chapter). A comparative view of the magnitude of the differences is presented in Fig. 5.10 were the propellant mass cost for the xGT1 and xGT2 are shown in a three-dimensional perspective.

5.3 Summary

A set of controllers were proposed to guide the translational motion of the spacecraft as dictated by the hovering laws. These controllers were based on a DB and PD controller. Selected cases were studied based on the results found in Chapter 4 regarding to the relative propellant penalties between the xGT1 and xGT2 with the detailed NSTAR model. The cases examined here presented strong evidence on the improved performance of the xGT1 using a combination of PD and DB controllers along the the x and y axes, respectively. This configuration showed that the xGT1 can improve propellant efficiency by more than 33% with respect to the xGT2. These improvements are directly associated with reduced thrust supplied by T_4 and T_5 in the xGT1 relative to the xGT2.

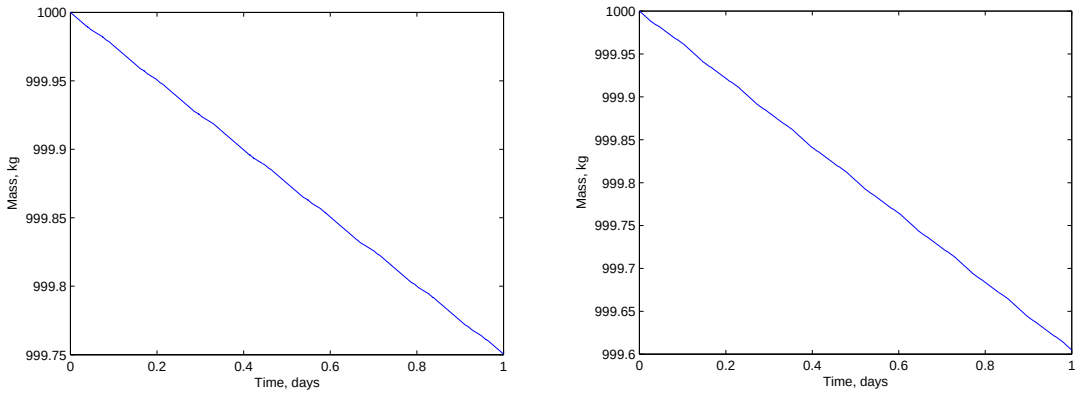

(a) (b)

Figure 5.7: Propellant mass consumed by (a) xGT1 and (b) xGT2.

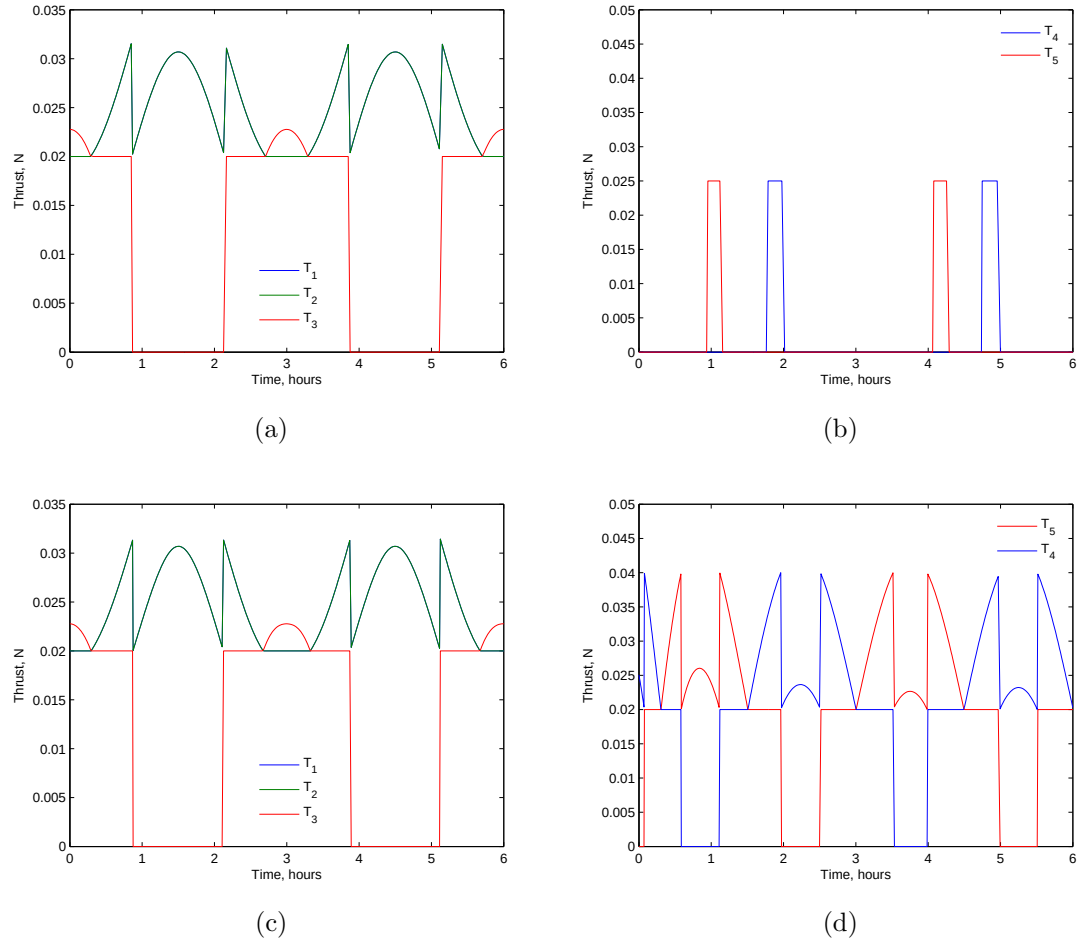

(a) (b)

(c) (d)

Figure 5.8: Operation of the xGT engines: (a) and (b) xGT1, (c) and (d) xGT2.

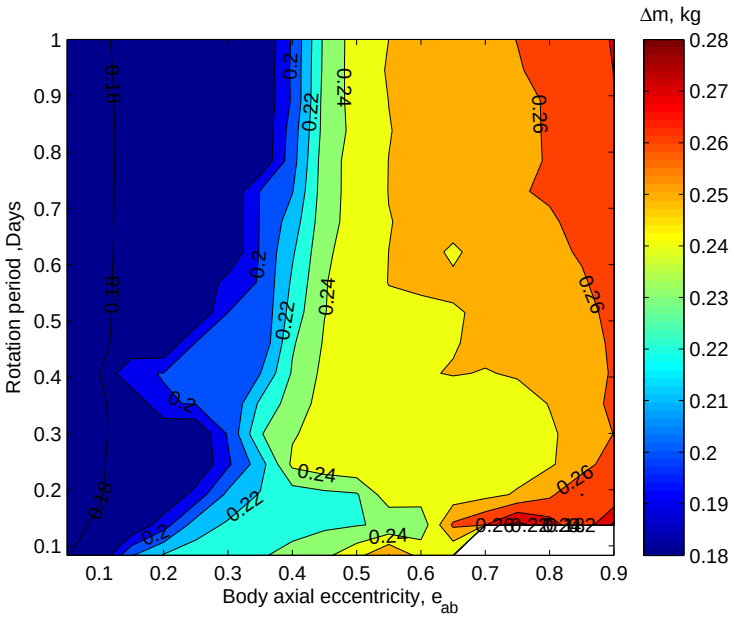

(a)

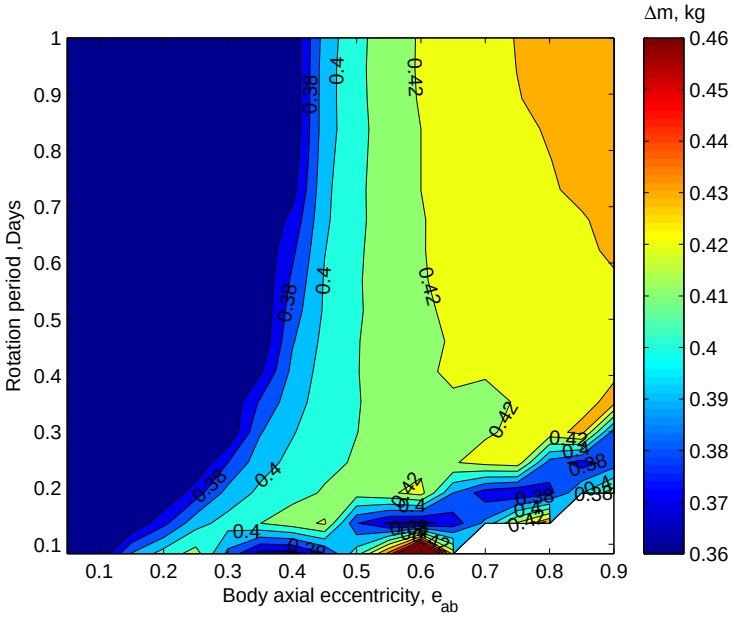

(b)

Figure 5.9: Propellant consumption map: (a) xGT1 and (b) xGT2.

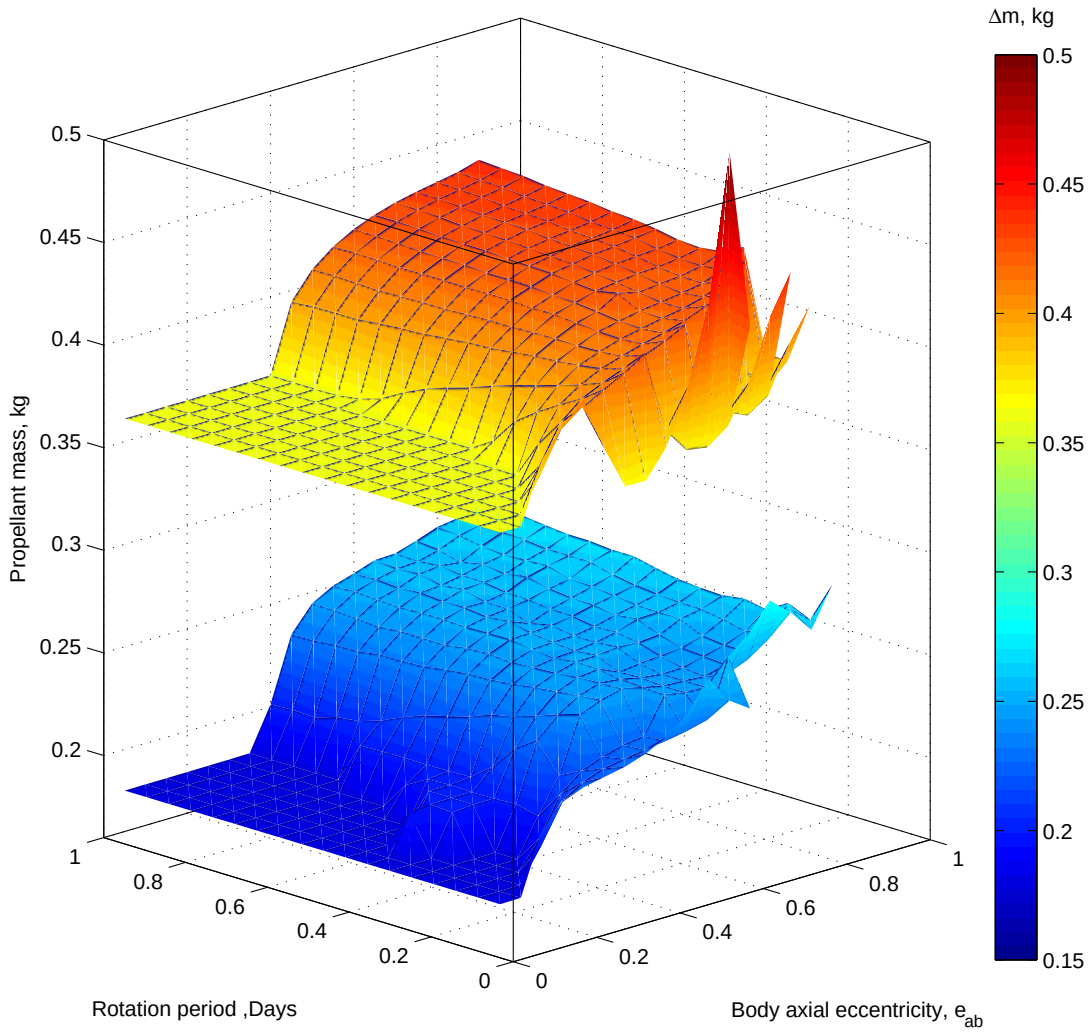

Figure 5.10: Comparative view of the xGT propellant consumption map: The bottom surface corresponds to the Δm due to the xGT1 and the top surface indicates the Δm due to the xGT2.

Chapter 6

Conclusions

The extended gravity tractor, or xGT, has been the purpose of this dissertation work. The xGT consist on a modification to the laws governing the dynamics of the classical GT and were aimed to improve the deflection Δv imparted on an asteroid by the action of a GT. In general, these guidance laws were designed to take into consideration the shape and rotation rate of the asteroid, allowing the GT spacecraft to move towards and away the center of mass of the asteroid in synchronous motion with the asteroid's spin. The first guidance law restricted the spacecraft motion to a single dimension along the desired towing direction. The second guidance law allows the GT spacecraft to move in two-dimensional space. These guidance laws were compared against each other and with respect to the classical inertial hovering.

The physical model assumed the asteroid to be a solid, homogeneous triaxial ellipsoid of constant density rotating about its principal axis of inertia. The GT spacecraft model considered five ion engines capable to control the translational dynamics in the vicinity of the asteroid. Two of these engines needed to be canted to prevent plume impingement over the surface of the asteroid. A realistic ion engine model based on the NSTAR system was included in the model to obtain improved estimates on the propellant costs associated with the implementation of these novel guidance laws.

The experiment addressed the performance and efficiency of these guidance laws over a range of asteroid shapes and rotation rates. The results obtained were compared against the classical GT hovering strategy. These novel guidance laws resulted in an improvement of nearly 60% in Δv imparted to the asteroid. Such Δv improvements directly translate into shorter times required to achieve a deflection, augmenting the chances of success of a GT mission to mitigate the treat of a small asteroid.

The propellant penalties were evaluated as well for each hovering mode. The first analysis consisted on an idealized thruster model as usually done in the literature [35, 39, 33]. Under these assumptions the proposed guidance laws resulted in propellant penalties ranging between 10% to 80% depending on the shape eccentricity of the asteroid. These penalties were also afected by the rotation rate of the asteroid reaching values greater that 200% near the limit of highly eccentric bodies with rotation periods shorter than 6 hours which increased the propellant requirement by a factor of four or more. However, it is wise to mention that these extreme scenarions are unlikely to occur in nature due to physical constraints related to the rotation rate and the axial elongation of a body. That is, the axial radius of rubble-pile asteroids is limited to the extent were the gravitational acceleration over the surface of the equator is balanced by the centrifugal acceleration caused by the rotation rate of the asteroid.

In a second experiment, the NSTAR engine model was included in the simulations to obtain a more realistic system performance. Contrary to our expectations, it was found that the propellant penalties due to the dynamic guidance laws introduced in this work were favored against the classical GT. This turnaround was mainly due to the lower bound in the thrust range of the engine that, once the required acceleration dropped below the engines lower operational threshold, thrusters in the opposite direction fire in order to balance the excess thrust. This effect was observed in asteroids with axial eccentricities greater than 0.6. At this point it is important

to mention that the spacecraft mass plays an important roll in these results. The thrust needed to sustain hovering at any distance is proportional to the spacecraft mass. The prescribed hovering distance needs to be defined based on the propulsion system capabilities, spacecraft mass, asteroid shape, and the rate at which Δv needs to be imparted on the asteroid to obtain a successful deflection. Thus for a given hovering strategy, a given propulsion system and total spacecraft mass, an optimal hovering range could be found to allow the best performance of the GT spacecraft and the propulsion system. A similar argument may be made for the xGT where its translation amplitude could be optimized in order to avoid the engines to operate in the differential thrust balance mode.

In Chapter 5 we tested a DB and a PD controller to control the motion along the three translational axes of the spacecraft. The DB controller was implemented along the y-axis of the xGT1 and the PD controller along the x and z-axis . On the xGT2 the PD controller was implemented independently along the three translational axes. The DB controller was not considered for the xGT2 because it could cause imprecise sluggish motion of the spacecraft. The performance of these controllers was tested on selected scenarios based on the results found in Chapter 4. For the selected cases we found that the DB controller contributed to improve the performance of the xGT by more that 33% with respect to the xGT2, even in cases where in Chapter 4 the xGT2 presented better performance over the xGT1.

The introduction of the xGT allows to approach the GT problem from a new perspective where the hovering strategies can be adjusted to optimize the performance of a GT system for each individual scenario. For example, depending on the characteristics of each target, the displacement amplitude can be defined to maintain a constant altitude from the surface or to hover the spacecraft at a fixed equipotential surface. It is likely that detailed system trade analysis may generate a more accurate picture about the feasibility of these hovering modes. It is possible to imagine the

combined implementation of any of these strategies together with other deflection strategies. For example one could consider to change the albedo of the asteroid by applying a coating on its surface [31]. In such case, it could be necessary to maintain a roughly constant distance from the asteroid, which could be achieved in principle by the implementation of the xGT guidance laws.

Bibliography

[1] R. Grieve and E. Shoemaker, *Hazards Due to Comets and Asteroids*, ch. The record of past impacts on Earth, p. 417. Tucson: The University of Arizona Press, 1994.

[2] E. M. Shoemaker, "Asteroid and comet bombardment of the Earth," *Annual Review of Earth and Planetary Sciences*, vol. Volume 11, pp. 461–494, 1983.

[3] O. B. Toon, K. Zahnle, R. P. Turco, and C. Covey, *Hazards Due to Comets and Asteroids*, ch. Environmental perturbations caused by impacts, p. 791. Tucson: The University of Arizona Press, 1994.

[4] C. Chyba, T. Owen, and W.-H. Ip, *Hazards Due to Comets and Asteroids*, ch. Impact delivery of Volatiles and Organic Molecules to Earth, pp. 9–58. Tucson: The University of Arizona Press, 1994.

[5] L. W. Alvarez, W. Alvarez, F. Asaro, , and H. V. Michel, "Extraterrestrial cause for the cretaceous-tertiary extinction," *Science*, vol. 208, pp. 1095–1108, 1980.

[6] D. Rabinowitz, E. Bowell, E. Shoemaker, and K. Mouinonen, *Hazards Due to Comets and Asteroids*, ch. The Population of Earth-Crossing Asteroids, pp. 285–312. Tucson: The University of Arizona Press, 1994.

[7] W. F. Bottke, A. Morbidelly, and R. Jedicke, *Mitigation of Hazardous Comets and Asteroids*, ch. Recent Progress in Interpreting the Nature of the Near-Earth Object Population, pp. 1–21. Cambridge University Press, 2004.

[8] E. Bowell and K. Muinonen, *Hazards Due to Comets and Asteroids*, ch. Earth-Crossing Asteroids and Comets: Graundbased Search Strategies, pp. 149–197. Tucson: The University of Arizona Press, Tucson, 1994.

[9] C. Bonanno, "An analytical approximation for the MOID and its consequences," *Astronomy and Astrophysics*, vol. 360, pp. 411–416, May 2000.

[10] G. Gronchi, G. Tommei, and A. Milani, *Near Earth Objects, Our Celestial Neighbors: Opportunity and Risk*, ch. Mutual Geometry of Confocal Keplerian Orbits: Uncertainty of the MOID and Search for Virtual PHAs, pp. 3–14. Cambridge University Press, 2006.

[11] B. J. Gladman, F. Migliorini, A. Morbidelli, V. Zappal, P. Michel, A. Cellino, C. Froeschl, H. F. Levison, M. Bailey, and M. Duncan, "Dynamical lifetimes of objects injected into asteroid belt resonances," *Science*, vol. 277, pp. 197–201, July 1997.

[12] A. Morbidelli, W. F. Bottke, C. Froeschlé, and P. Michel, *Asteroids III*, ch. Origin and Evolution of Near-Earth Objects, pp. 409–422. The University of Arizona Press, Tucson, 2002.

[13] E. M. Shoemaker, P. R. Weissman, and C. S. Shoemaker, *The Flux of Periodic Comets Near Earth*, pp. 313–335. The University of Arizona Press, Tucson, 1994.

[14] S. Chesley, "Potential impact detection for near-earth asteroids: the case of 99942 Apophis (2004 MN4)," *Proceedings of the International Astronomical Union*, vol. 1, no. S229, pp. 215–228, 2005.

[15] J. D. Giorgini, L. A. Benner, S. J. Ostro, M. C. Nolan, and M. W. Busch, "Predicting the Earth encounters of (99942) Apophis," *Icarus*, vol. 193, pp. 1 – 19, 2008.

[16] C. R. Chapman, *Mitigation of Hazardous Comets and Asteroids*, ch. What we know and don't know about surfaces of potentially hazardous small bodies, pp. 104–112. Cambridge University Press, Cambridge, 2004.

[17] C. Gritzner and R. Kahle, *Mitigation of Hazardous Comets and Asteroids*, ch. Mitigation Techologies and Their Requirements, pp. 167–200. Cambridge University Press, Cambridge, 2004.

[18] T. J. Ahrens and A. W. Harris, "Deflection and fragmentation of near-earth asteroids," *Nature*, vol. 360, pp. 429 – 433, December 1992.

[19] T. A. Ahrens and A. W. Harris, *Hazards Due to Comets and Asteroids*, ch. Deflection and Fragmentation of Near-Earth Asteroids, pp. 897–927. The University of Arizona Press, Tucson, 1994.

[20] K. A. Holsapple, *Mitigation of Hazardous Comets and Asteroids*, ch. About Deflecting Asteroids and Comets, pp. 113 – 140. Cambridge University Press, 2004.

[21] C. R. McInnes, "Deflection of near-Earth asteroids by kinetic energy impacts from retrograde orbits," *Planetary and Space Science*, vol. 52, no. 7, pp. 587–590, 2004.

[22] D. Izzo, A. Bourdoux, R. Walker, and F. Ongaro, "Optimal trajectories for the impulsive delfection of near earth objects," *Acta Astronautica*, vol. 59, pp. 294–300, 2006.

[23] H. J. Melosh, I. V. Nemchinov, and Y. I. Zetzer, *Hazards Due to Comets and Asteroids*, ch. Non-Nuclear strategies for deflecting comets and asteroids, pp. 1111–1132. The University of Arizona Press, Tucson, 1994.

[24] W. H. Blume, "Deep Impact mission design," *Space Science Reviews*, vol. 117, pp. 23–42, March 2005.

[25] D. K. Yeomans, J. D. Giorgini, and S. R. Chesley, "The history and dynamics of comet 9P/Tempel 1," *Space Science Reviews*, vol. 117, pp. 123–135, March 2005.

[26] J. R. Olds, A. Charania, and M. G. Schaffer, "Multiple mass drivers as an option for asteroid deflection missions," No. AIAA-2007-S3-7, (Washington, D.C.), 2007 Planetary Defense Conference, March 2007.

[27] R. Walker, D. Izzo, C. de Negueruela, L. Summerer, M. Ayre, and M. Vasile, "Concepts for near earth asteroid deflection using spacraft with advanced nuclear and solar electric propulsion systems," *Journal of the British Interplanetary Society*, vol. 58, pp. 268–278, October 2005.

[28] D. Scheeres and R. Schweickart, "The mechanics of moving asteroids," in *Proceedings of the 2004 Planetary Defense Conference*, no. AIAA Paper 2004-1446, (Orange County, California), American Institute of Aeronautics and Astronautics, February 2004.

[29] H. J. Melosh and I. V. Nemchinov, "Solar asteroid diversion," *Nature*, vol. 366, pp. 21–22, November 1993.

[30] B. P. Shafer, M. D. Garcia, R. J. Scammon, C. M. Snellm, and R. F. Stellingwerf, *Hazards Due to Comets and Asteroids*, ch. The Coupling of Energy to Asteroids and Comets, pp. 955 – 1012. The University of Arizona Press, Tucson, 1994.

[31] D. Hyland, H. Altwaijry, S. Ge, R. Margulieux, J. Doyle, J. Sandberg, B. Young, X. Bai, J. Lopez, and N. Satak, "A permanently-acting NEA mitigation technique via the Yarkovsky effect." October 2009.

[32] E. Lu and S. Love, "Gravitational tractor for towing asteroids," *Nature*, vol. 438, pp. 177–178, 2005.

[33] D. Yeomans, S. Bhaskaran, S. Broschart, S. Chesley, P. Chodas, T. Sweetser, and R. Schweickart, "Deflecting a hazardous near-Earth object," (Granada, Spain), 1st IAA Planetary Defense Conference: Protecting Earth From Asteroids, 27-30 April 2009.

[34] C. R. McInnes, "Near earth object orbit modification using gravitational coupling," *Journal of Guidance, Control, and Dynamics*, vol. 30, no. 3, pp. 870–873, 2007.

[35] B. Wie, "Dynamics and control of gravity tractor spacecraft for asteroid deflection," *Journal of Guidance, Control, and Dynamics*, vol. 31, no. 5, pp. 1413 – 1423, 2008.

[36] E. G. Fahnestock and D. J. Scheeres, "Dynamic characterization and stabilization of large Gravity-Tractor designs," *Journal of Guidance, Control, and Dynamics*, vol. 31, no. 3, pp. 501–521, 2008.

[37] M. D. Rayman, P. Varghese, D. H. Lehman, and L. L. Livesay, "Results from the Deep Space 1 technology validation mission," *Acta Astronautica*, vol. 47, no. 2-9, pp. 475 – 487, 2000. Space an Integral Part of the Information Age.

[38] M. D. Rayman, T. C. Fraschetti, R. C. A., and C. T. Russell, "Dawn: A mission in development for exploration of main belt asteroids Vesta and Ceres," *Acta Astronautica*, vol. 58, pp. 605–616, 2006.

[39] D. Yeomans, S. Bhaskaran, S. Broschart, S. Chesey, P. Chodas, M. Jones, and T. Sweetser, "Near-earth object (NEO) analysis of transponder tracking and gravity tractor performance," JPL Task Plan No. 82-120022, Jet Propulsion Laboratory, September 2008.

[40] S. Sawai, D. J. Scheeres, and S. B. Broschart, "Control of hovering spacecraft using altimetry," *Journal of Guidance, Control, and Dynamics*, vol. 25, no. 4, pp. 786–795, 2002.

[41] S. B. Broschart and D. J. Scheeres, "Control of hovering spacecraft near small bodies: Application to asteroid 25143 Itokawa," *Journal of Guidance, Control, and Dynamics*, vol. 28, no. 2, pp. 343–354, 2005.

[42] S. B. Broschart and D. J. Scheeres, "Boundedness of spacecraft hovering under dead-band control in time-invariant systems," *Journal of Guidance, Control, and Dynamics*, vol. 30, no. 2, pp. 601–610, 2007.

[43] T. Kominato, M. Matsuoka, M. Uo, T. Hashimoto, and J. Kawaguchi, "Optical hybrid navigation in hayabusa: Approach, station keeping & hovering," in *16th AAS/AIAA Spaceflight Mechanics Meeting, Tampa, Florida, January 22-26*, AAS Paper 06-210, pp. 1753 – 1772, American Astronautical Society, January 2006.

[44] D. J. Scheeres, "Stability of hovering orbits around small bodies," in *Advances in Astronautical Sciences*, vol. 102, (San Diego, CA.), pp. 855–875, 1999.

[45] J. R. Brophy, R. Y. Kakuda, J. E. Polk, J. R. Anderson, M. G. Marcucci, D. Brinza, M. D. Henry, K. K. Fujii, K. R. Mantha, J. F. Stocky, J. Sovey, M. Patterson, V. Rawlin, J. Hamley, T. Bond, J. Christensen, H. Cardwell, G. Benson, J. Gallagher, M. Matranga, and D. Bushway, "Ion propulsion system

(NSTAR) DS1 technology validation report," Tech. Rep. JPL Publication 00-10, Jet Propulsion Laboratory, October 2000.

[46] R. S. Hudson and S. J. Ostro, "Shape of asteroid 4769 castalia (1989 PB) from inversion of radar images," *Science*, vol. 263., pp. 940 – 943, February 1994.

[47] S. R. Hudson and S. J. Ostro, "Shape and non-principal axis spin state of asteroid 4179 Toutatis," *Science*, vol. 270, pp. 84 – 86, Octobe 1995.

[48] S. J. Ostro, R. S. Hudson, M. C. Nolan, J.-L. Margot, D. J. Scheeres, D. B. Campbell, C. Magri, J. D. Giorgini, and D. K. Yeomans, "Radar observations of asteroid 216 Kleopatra," *Science*, vol. 288, pp. 836 – 839, May 2000.

[49] S. J. Ostro, M. C. Benner, Lance A.M.and Nolan, C. Magri, J. D. Giorgini, D. J. Scheeres, S. B. Broschart, M. Kaasalainen, D. Vokrouhlick, S. R. Chesley, J.-l. Margot, R. F. Jurgens, R. Rose, D. K. Yeomans, S. Suzuki, and E. M. De Jong, "Radar observations of asteroid 25143 Itokawa (1998 SF36)," *Meteoritics & Planetary Science*, vol. 39, pp. 407–424, March 2004.

[50] J. K. Miller, A. S. Konopliv, P. G. Antreasian, J. J. Bordi, S. Chesley, C. E. Helfrich, W. M. Owen, T. C. Wang, B. G. Williams, and D. K. Yeomans, "Determination of shape, gravity, and rotational state of asteroid 433 Eros," *Icarus*, vol. 155, no. 1, pp. 3–17, 2002.

[51] S. Abe, T. Mukai, N. Hirata, O. S. Barnouin-Jha, A. F. Cheng, H. Demura, R. W. Gaskell, T. Hashimoto, K. Hiraoka, T. Honda, T. Kubota, M. Matsuoka, T. Mizuno, R. Nakamura, D. J. Scheeres, and M. Yoshikawa, "Mass and local topography measurements of Itokawa by Hayabusa," *Science*, vol. 312, no. 5778, pp. 1344 – 1347, 2006.

[52] J. Ivory, "On the attractions of homogeneous ellipsoids," *Philosophical Transactions of the Royal Society of London*, vol. 99, pp. 345–372, 1809.

[53] J. M. A. Danby, *Fundamentals of Celestial Mechanics*. Willmann-Bell, 2 ed., 1992.

[54] W. D. MacMillan, *The Theory of Potential*. Dover Publications Inc., 1 ed., 1958.

[55] F. R. Moulton, *An Introduction to Celestial Mechanics*. Dover Publications Inc., 2 ed., 1970, New York.

[56] W. H. Press, W. T. Teukolsky, W. T. Vetterling, and B. P. Flannery, *Numerical Recipes in Fortran*. Cambridge University Press, 2 ed., 1992. The reference is taken from Scheeres 1994.

[57] D. Y. Oh, "Evaluation of solar electric propulsion technologies for discovery-class missions," *Journal of Spacecraft and Rockets*, vol. 44, no. 2, pp. 399–411, 2007.

[58] P. Stella, S. DiStefano, M. Rayman, and A. Ulloa-Severino, "Early mission power assessment of the Dawn solar array," in *Photovoltaic Specialists Conference (PVSC), 2009 34th IEEE*, pp. 1617 –1621, June 2009.

[59] N. Fatemi, S. Sharma, O. Buitrago, J. Crisman, P. Sharps, R. Blok, M. Kroon, C. Jalink, R. Harris, P. Stella, and S. Distefano, "Performance of high-efficiency advanced triple-junction solar panels for the LILT mission Dawn," in *Photovoltaic Specialists Conference, 2005. Conference Record of the Thirty-first IEEE*, pp. 618 – 621, January 2005.

[60] D. M. Goebel and I. Katz, *Fundamentas of Electric Propulsion*. JPL Space Science and Technology Series, John Wiley & Sons, 2008.

[61] D. A. Vallado, *Fundamentals of Astrodynamics and Applications*, ch. 8, p. 575. Microcosm Press, 3rd ed., 2007.

[62] C. D. Brown, *Elements of Spacecraft Design*, ch. 5, p. 267. AIAA, 2002.

[63] P. Pravec, H. A. W., and B. D. Warner, "NEA rotations and binaries," in *Near Earht Objects, our Celestial Neighbors: Opportunity and Risk*, vol. 236, pp. 167 – 176, Procedings of the International Astronomical Union., Cambridge University Press, Cambridge, 2007.

[64] P. Pravec, A. Harris, D. Vokrouhlick, B. Warner, P. Kusnirk, K. Hornoch, D. Pray, D. Higgins, J. Oey, A. Gald, S. Gajdos, L. Kornos, J. Vilgi, M. Husrik, Y. Krugly, V. Shevchenko, V. Chiorny, N. Gaftonyuk, W. C. Jr., J. Gross, D. Terrell, R. Stephens, R. Dyvig, V. Reddy, J. Ries, F. Colas, J. Lecacheux, R. Durkee, G. Masi, R. Koff, and R. Goncalves, "Spin rate distribution of small asteroids," *Icarus*, vol. 197, no. 2, pp. 497 – 504, 2008.

VITA

Dario O. Cersosimo was born October 10^{th}, 1977 in the city of Buenos Aires, Argentina. In 1993 he moved to the island of Puerto Rico where later, in 2002, he earned a Bachelor of Science in Applied Physics from the University of Puerto Rico at Humacao. In May 2005 he obtained a Masters of Science in Space Sciences from Embry-Riddle Aeronautical University at Daytona Beach, Florida. In May 2011 he received the degree of Doctorate of Philosophy in Mechanical and Aerospace Engineering from the University of Missouri.